TOPOLOGY OPTIMIZED REINFORCED CONCRETE WALLS CONSTRUCTED WITH 3D PRINTED FORMWORK

By
Triveni Mudaliar
Rémy D. Lequesne
Matthew Fadden

Structural Engineering and Engineering Materials
SL Report 20-1
January 2020

THE UNIVERSITY OF KANSAS CENTER FOR RESEARCH, INC.
2385 Irving Hill Road, Lawrence, Kansas 66045-7563

TOPOLOGY OPTIMIZED REINFORCED CONCRETE WALLS CONSTRUCTED WITH 3D PRINTED FORMWORK

By

Triveni Mudaliar

Rémy D. Lequesne

Matthew Fadden

Structural Engineering and Engineering Materials
SL Report 20-1
THE UNIVERSITY OF KANSAS CENTER FOR RESEARCH, INC.
LAWRENCE, KANSAS
January 2020

ABSTRACT

The construction industry continually evolves to adapt to gains in knowledge, market pressures and new technologies. However, two promising new technologies, 3D printing and computational topology optimization, have not yet penetrated the civil engineering industry despite being important drivers of change in other fields. The aim of this study was the potential to overcome the major barriers to adoption of both technologies by using them in combination. Both theoretical and practical problems must still be addressed, but the potential impacts are significant: lightweight, architecturally pleasing, reduced volume structures.

Two small-scale specimens were constructed and tested to demonstrate the feasibility of using additively manufactured (3D printed) formwork to construct complex reinforced concrete (RC) structures. The concept was shown to be viable. Areas were identified where further development is necessary before 3D printing can be used for large-scale cost-competitive formwork.

An approach, based on the rule of mixtures, was proposed for applying computational topology optimization to RC structures. This was necessary because the computational topology optimization algorithm employed in this study assumes a structure is homogenous but RC structures are not. The approach was shown to work for optimizing an RC wall for force demands within the linear-elastic range of response.

The sensitivity of optimization outputs to modeling parameters was investigated. The effects and interdependencies of mesh size, element type, number of optimization cycles, and target volume ratio on optimization outcome were demonstrated. The importance of ISO and “percent reduction” parameters on the process of importing the optimized geometry to ABAQUS was also demonstrated.

Finally, a parametric study was conducted to examine the relationships between volume ratio and member strength and stiffness (volume ratio refers to the volume of the optimized structure divided by the volume of the original structure). The study used finite element models of topology optimized slender structural walls subjected to pseudo-static lateral force. It was shown that reductions in volume are not proportional to reductions in stiffness, as expected for slender walls that are flexure-dominated. Reductions in volume of 10 to 20% cause only approximately 3 to 7% reductions in uncracked member stiffness. These reductions in stiffness can be compensated for with use of modestly higher-strength concrete.

Keywords: topology optimization, additive manufacturing, 3D printing, reinforced concrete, structural wall

TABLE OF CONTENTS

LIST OF TABLES

LIST OF FIGURES

CHAPTER 1 - INTRODUCTION

1.1 Motivation

Computational topology optimization is a mathematical approach to optimizing structural geometry. The process iteratively removes material or changes the distribution of material (depending on the algorithm being used) within a design domain. Use of topology optimization in design of structural members would allow designers to produce highly efficient and often aesthetically appealing structures that have less mass and a smaller carbon footprint than traditional civil engineering structures. However, although topology optimization has been well established in the automotive and aerospace industries for many years (Donofrio, 2016), it has yet to make a significant impact in the architectural, engineering, and construction industries. The limited impact is mainly attributed to the (1) difficulty of constructing the complex, irregular, and non-linear designs that result from topology optimization; (2) difficulty of applying topology optimization algorithms, which typically assume homogenous materials, to reinforced concrete (RC) structures; and (3) paucity of test data of topology optimized RC structures, and therefore limited knowledge of the behavior of optimized structures in terms of stiffness, strength, and deformation capacity.

Additive manufacturing may provide a solution to the challenges associated with constructing complex topology optimized structures. For example, it is possible to use additive manufacturing techniques like printing of concrete to construct complex shapes without formwork. However, this approach requires the concrete printer to be larger than the structure, which may not always be economical. Furthermore, there are concerns about the integrity of 3D-printed concrete structures because of potentially weak bond between printed layers and the inability to conveniently place reinforcing bars. Instead of printing the entire complex structure, it is proposed to use additive manufacturing to fabricate formwork. This approach allows use of a smaller 3D printer in an offsite

and controlled environment, and facilitates construction of cast-in-place or precast topology-optimized structures that include reinforcement.

1.2 Objectives and Scope

As a starting point towards future development of topology optimized RC structures, the scope of this investigation is aimed at design, construction, testing, and modeling of optimized RC slender walls under lateral force. The main objectives were to (1) use small-scale specimens to demonstrate the feasibility of using 3D-printed formwork to construct complex RC structures; (2) propose a method for applying topology optimization to RC structures and evaluate the sensitivity of topology optimization outputs to model parameters, (3) use finite element models of topology optimized slender structural walls subjected to pseudo-static lateral force to examine the relationships between volume ratio and member strength and stiffness (volume ratio refers to the volume of the optimized structure divided by the volume of the original structure); and (4) use finite element models to examine the extent to which increased concrete strength offsets the loss of strength and stiffness associated with volume reduction of structures.

CHAPTER 2 - LITERATURE REVIEW

Computational topology optimization is a free-form design tool used by researchers and designers in several industries to produce reduced-weight structures. Recent investigations have developed ways of using varied manufacturing techniques including CNC milling, robotic wire cutting, among others to solve the constructability issues associated with the complex forms obtained from topology optimization. Additive manufacturing (3D printing) has not, to the author's knowledge, been investigated as a technique used to construct topology optimized RC structures and needs investigation. This review will focus on the research related to reinforced concrete members designed using computational topology optimization and constructed using additive manufacturing techniques that could facilitate construction of topology optimized structures. A thorough review of topology optimization algorithms and optimization of varied structural elements under different loading conditions is beyond the scope of this investigation.

2.1 Topology Optimization

2.1.1 Overview of Topology Optimization Algorithms

Topology optimization typically requires the user to define an objective function and constraints. The objective function defines the goal of the optimization, usually either minimizing, maximizing, or minimizing the maximum value of a specified design parameter. Specified design parameters can be volume, displacement, stress, or strain energy, among others. An objective function of minimizing the strain energy is common. A user-defined constraint restricts a design response (e.g. volume, strain energy, or displacement) in the optimization. For example, a constraint could be defined that limits the reduced volume to not less than 70% of the original volume. For this constraint, regardless of the objective function (e.g. minimizing strain energy), the final optimized design/shape will have a volume that is not less than 70% of that of the original

structure. Another common constraint would be to not allow the deflection of a point on the structure to exceed a given value.

For any given objective function and constraints, there are several topology optimization algorithms available in commercially available software. Most are broadly similar to either the evolutionary structural optimization (ESO) method or solid isotropic material with penalization (SIMP) method.

The ESO method, of which extended ESO and bidirectional ESO are variations, begins with a finite element analysis of the structure of interest subjected to the loading condition. The Von-Mises stress distribution obtained from this analysis is used as a basis for identifying and removing lightly stressed elements of the structure. Elements are lightly stressed if the Von-Mises stresses are less than the product of a specified rejection ratio (RR) and the maximum stress in the structure (Xie and Steven, 1993). A common initial rejection ratio is 1%. Once the elimination process is done, a finite element analysis is again carried out to obtain the Von-Mises stress distribution within the modified structure. At this step, an evolution rate (ER) is added to the rejection ratio used previously and a new cumulative rejection ratio is used to identify and then remove lightly stressed elements. An ER of 1 percentage point is commonly used, resulting in the cumulative rejection ratio increasing by increments of 1 percentage point in every step. This iterative procedure is repeated until a predefined optimum condition (or specified constraint) is reached. An example predefined optimum condition is when the entire optimized shape experiences a specified percent of maximum stress (e.g. 25%).

Rather than remove elements, the SIMP method iteratively changes the density of each element within a structure, assigning them densities that are between 0 (void) and 1 (solid) times the original density of the element. This approach was not used in this study because of difficulties

constructing the optimized structure, which contains elements with varied densities, using cast-in-place concrete.

A major advantage of the ESO method is that the material properties (density, stiffness) are not altered and thus remain homogeneous throughout the structure. The resulting optimized shape therefore consists of either solid elements or completely hollow (void) elements. This report is focused on the ESO method.

2.1.2 Examples of Topology Optimized Buildings in Practice

Few topology optimized structures have been constructed, although topology optimization has been occasionally used by structural engineers to develop preliminary theoretical solutions to design problems.

One of the first applications of topology optimization in full-scale structural design was for a multi-space cultural and tourism building in Blanes, Spain in 2002. The columns, which represent the form of a tree and transfer gravity loads to the earth (Figure 2.1(a)), were optimized using a 3D extended (ESO) digital tool (Januszkiewicz and Banachowicz, 2017). Due to budgetary constraints, the construction of the building in Blanes, Spain was suspended.

In 2004, one of the first topology optimized reinforced concrete structures was built in Takatsuki, Japan (Figure 2.1(b)). It was designed using the ESO method (Ohmori, 2008). Although the walls of the four-story office building were optimized for vertical and lateral loads, the forces were primarily resisted by the reinforced concrete moment frame and the walls behaved as a façade.

Topology optimization was used for design of a 1310 by 138 by 66 ft high train station in Florence, Italy. Specifically, the extended ESO method was used to generate optimized columns shaped like tree branches. The designers intended to construct the optimized structure with reinforced

concrete. However, a competing design was selected for construction. The proposed optimized design was instead later constructed in Doha, Qatar, where it serves as the Qatar National Convention Center that officially opened in 2011. Steel was ultimately used instead of reinforced concrete because it was simpler to construct. The 66-ft high tree-shaped column consists of two main components: the visible non-structural cladding exterior and a structural core comprised of octagonal tubes constructed from steel plates (Donofrio, 2016). Thus, the originally optimized RC design was simplified to a steel structure with cladding designed to appear as though it had been optimized (Figure 2.1(c)).

The same extended ESO method was used to design the Rolex Learning Center in Switzerland (Figure 2.1(d)) (Januszkiewicz and Banachowicz, 2017).

2.1.3 Experimental Research on Topology Optimized Structures

Few researchers have constructed topology optimized reinforced concrete members. One was the optimized slab with four supports shown in Figure 2.2(a) (Jipa et al., 2016). The computational topology optimization in that study was done using the density-based SIMP algorithm in ABAQUS. Ultra-high-performance fiber reinforced concrete (UHPFRC) was used in design and construction of the specimens instead of reinforcing bars, facilitating construction of the complex geometries produced by the optimization process. However, data from tests of the structure were not reported, so little can be learned regarding behavior or modeling of the structure.

(a)

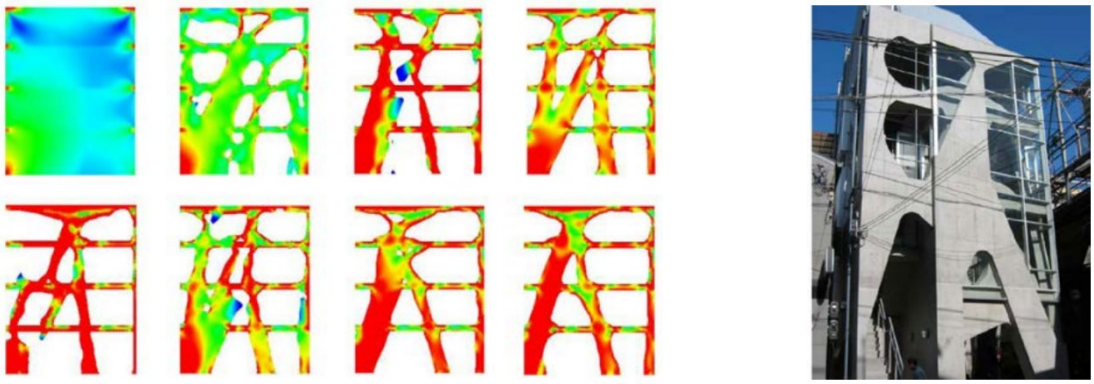

(b)

(c)

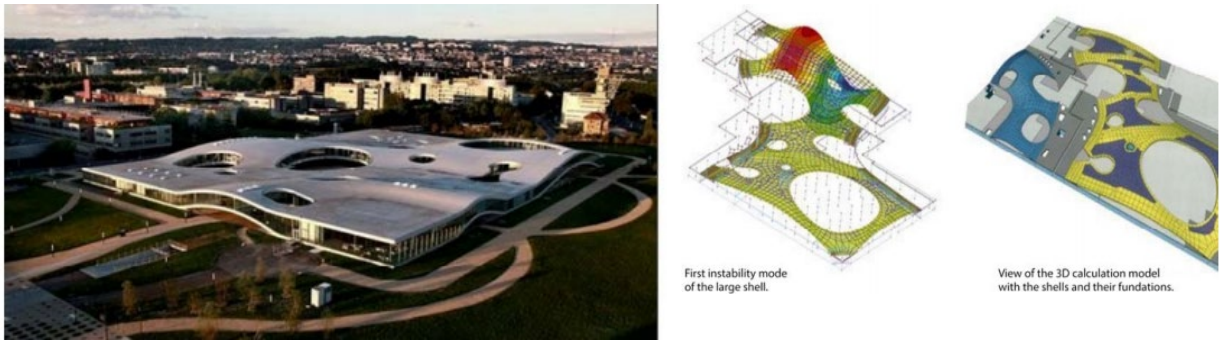

(d)

Figure 2.1: Examples of topology optimized structures constructed in (a) Blanes, Spain, 2002 (not constructed) (Januszkiewicz and Banachowicz, 2017); (b) Takatsuki, Japan, 2004 (Donofrio, 2016); (c) Doha, Qatar, 2008 (Jewett, 2018); and (d) Lausanne, Switzerland, 2008 (Januszkiewicz and Banachowicz, 2017)

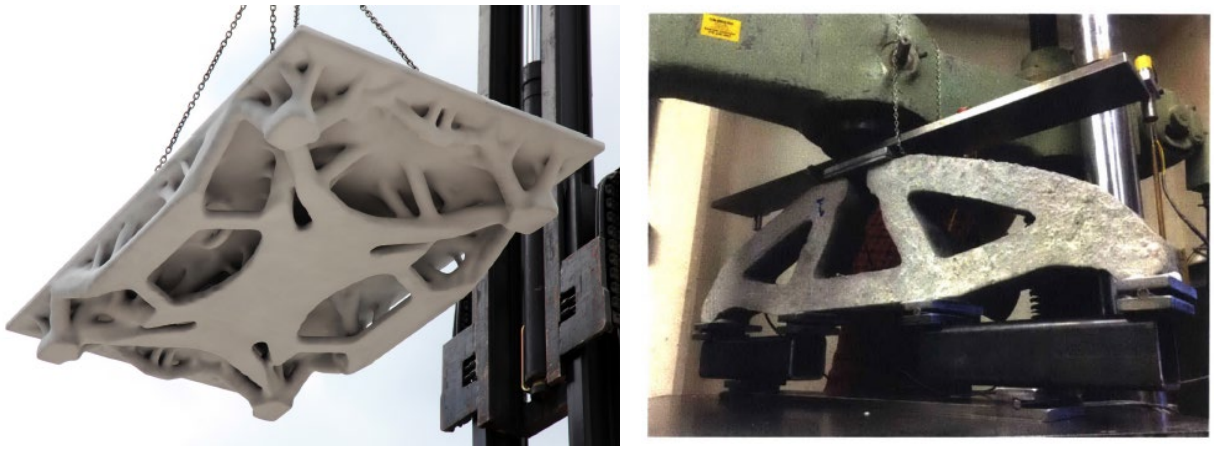

(a) (b)

Figure 2.2: Topology optimized (a) UHPFRC slab with four supports (Jipa et al., 2016) and (b) PC beam testing under compression (Jewett and Carstensen, 2019)

Jewett and Carstensen (2019) reported data from tests of topology optimized RC beams designed to represent hammerhead piers of a bridge subjected to a point load at midspan and supported at four locations. (Figure 2.2(b)). Five different designs were tested: a rectangular plain concrete prism, three topology optimized plain concrete beams, and one topology optimized reinforced concrete beam constructed using formwork made using a computer numerical control (CNC) milling machine. For each design, three specimens were fabricated and tested (15 specimens in total). The non-optimized original beam had dimensions of 36 by 9 by 3 in. and a target concrete compressive strength of 5000 psi. The three types of topology optimized plain concrete specimens were designed to have a volume that was 50% of the original volume, but using different methods:

1) Compliance-based topology optimization. The objective function was to minimize the compliance (maximize stiffness) using a pre-defined volume. The constraints were (1) maintaining static equilibrium, (2) restricting relative densities of individual elements to values between 0 and 1, and (3) not exceeding the defined maximum volume (50%). It assumed isotropic behavior of concrete. The final volume after optimization process was equal to 50% of that of the rectangular prism.

2) Stress-based optimization with the tensile strength of concrete assumed to be $8\sqrt{f'_c}$. The objective function of this method was to minimize volume until specified limits of maximum and minimum stress were reached (e.g. the tensile strength of concrete was limited to $8\sqrt{f'_c}$). It assumed anisotropic behavior of concrete and checked every element in the system against stress limits at each step. This was an extremely time-consuming approach. The final volume after optimization process was equal to 49% of the original rectangular beam.
3) Stress-based optimization with the tensile strength of concrete assumed to be $6\sqrt{f'_c}$. The optimization process was similar to the previous method. Concrete was assumed to fail in tension within the upper and lower bounds in these two stress-based methods. The final volume after optimization process was equal to 56% of rectangular prism.

The shape and volume of the topology optimized specimens obtained from the three different methods were different. The fourth type of topology optimized reinforced concrete beam had the same materials and geometry as the specimens designed with the first method (compliance-based), but it also had one No. 3 reinforcing bar in the tension cord with the optimized design obtained from the first method. The steel cross-sectional area was not designed for the expected tension force using the topology optimization algorithm; the bar was selected based on judgement.

In this study, the specimen designed with an assumed concrete tensile strength of $6\sqrt{f'_c}$ had a volume that was 7% greater than the volume of the specimen with an assumed concrete tensile strength of $8\sqrt{f'_c}$. This occurred because the strength of unreinforced ties (tension members) limited the strength of the optimized structure. The results from three tests per design were averaged for the five specimens and are listed in Table 2.1. Although all the specimens surpassed

the design load of 2000 lb and had a target volume of 49 to 56% of that of the original beam, the different final volumes of members and optimized shapes resulted in different measured strengths (Table 2.1). Interestingly, the specimens designed using a compliance-based algorithm and a stress-based algorithm with a concrete tensile strength of $6\sqrt{f'_c}$ had similar strengths. As would be expected, the specimen designed with a less conservative estimate of concrete tensile strength exhibited the lowest strength. Also as expected, the strength of the compliance-based optimized specimen was improved substantially by introducing reinforcement, even though it was not topology optimized with the expectation of being reinforced.

Table 2.1: Results from tests of concrete beams supported at four points with point load at midspan

Design	Volume (%) [1]	Maximum (avg.) Strength (lbs) [1]
Rectangular PC prism (control)	100	23260
Compliance-based optimized beam	50	5100
Compliance-based optimized RC beam	50	17770
Stress-based optimized beam [2]	49	3360
Stress-based optimized beam [3]	56	4820

[1] Values reported from Jewett (2018). [2] Concrete tensile strength assumed to be $8\sqrt{f'_c}$. [3] Concrete tensile strength assumed to be $6\sqrt{f'_c}$.

Although this was an interesting study, a major limitation of this investigation was the use of plain concrete. Plain concrete structures in practice are largely obsolete and an investigation of topology optimized reinforced concrete structures is needed. Another limitation was the stress-based algorithm, which efficiently accounted for the anisotropic behavior of concrete but failed to produce a solid-void (binary) optimized design. Significant post-processing was therefore needed to remove volumes with intermediate densities, which affected the behavior of the specimens. One limitation of the stress-based method was the use of a "P-norm" function introduced in the stress expression to reduce the time required to evaluate the stresses of every element in the member at each step. The "P-norm" function is a case-specific variable, selected by the designer based on

judgement, and has no practical meaning. On the other hand, the algorithm used to design the compliance-based optimized specimen did not consider the anisotropic behavior of concrete, produced a solid-void design, and yet failed at 50% higher load than the stress-based optimized specimens. There is a need to explore topology optimization of members with isotropic material properties and study the behavior of optimized structures with actual material properties to quantify strength, stiffness, and deformation capacity.

2.2 Additive Manufacturing Techniques

Several researchers have investigated different additive manufacturing techniques to efficiently build complex structures. These new emerging technologies may also speed up the process of construction. Currently, complex topology optimized structures could be directly built using either a D-shape process, contour crafting, or concrete printing (Lim et al., 2012). The D-shape process uses a nozzle mounted on a gantry frame to deposit binder on a powder bed (artificial sandstone). The maximum height that can be built using D-shape process is about 40 ft (Donofrio, 2016). Contour crafting uses a crane to extrude cement paste with a large deposition head that can build the full width of a structural wall at once. Concrete printing extrudes mortar using a smaller resolution nozzle mounted on gantry frame. It produces a more intricate finished structure. The large equipment size, difficulty placing reinforcing bars, questionable bond strength between printed layers, and the difficulty in using use coarse aggregates and large fibers in printed concrete pose significant limitations to using these manufacturing techniques in practice. Even if fiber reinforced concrete (FRC) is used to completely replace steel reinforcement, it does not cross layers to improve the inter-layer bond strength. Moreover, to use FRC with > 1% fiber volume fractions, a more developed extrusion system is required to effectively incorporate FRC in concrete printing (Hambach and Volkmer, 2017).

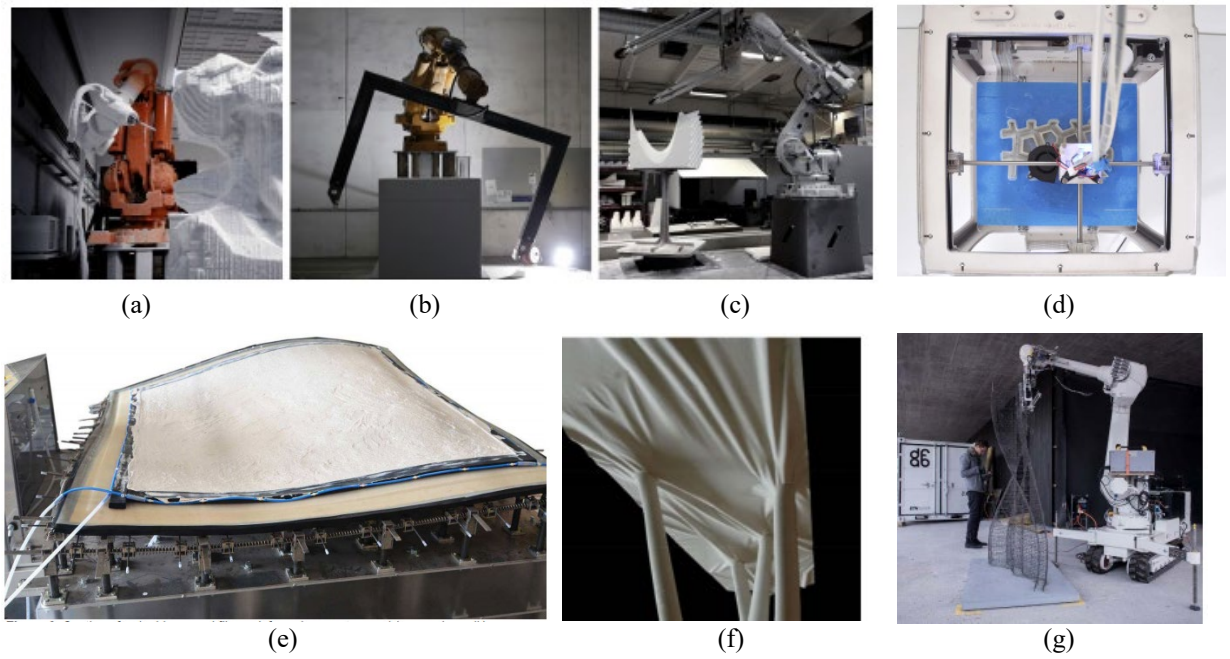

Figure 2.3: Equipment for fabrication of formwork (a) Robotic CNC Milling, (b) Robotic Hot-Wire Cutting, (c) Robotic Abrasive Wire Cutting, (Sondergaard et al., 2018), (d) 3D Printer (Peters, 2014), (e) 25-Actuator Based Flexible Molds (Raun and Kirkegaard, 2014), (f) Flexible Fabric Formwork (Hawkins et al., 2016) and (g) Mesh Mold which uses uniform reinforcement of RC members as formwork and the concrete is placed inside the mesh (Hack et al., 2017)

An alternative to printing concrete could be fabrication of non-prismatic formwork for complex shapes. This is more viable as the on-site construction process and skill requirements remain similar to current practice. This approach also eliminates some of the limitations of concrete printing listed above, particularly the limitation on placement of reinforcement. The most commonly used methods include CNC milling, hot-wire cutting, abrasive wire cutting, 3D printing, and use of actuator based flexible molds, flexible fabric formwork, or robotically fabricated stay-in-place reinforcing bar mesh formwork (mesh mold) (Figure 2.3). Of these, CNC milling and 3D printing are most convenient.

Jewett (2018) used an ONSRUD 3-axis mill with a 0.5-in. diameter bit to cut Styrofoam (Figure 2.4(a)). The formwork was used to cast a 36 by 9 by 3 in. optimized beam. Although it took only 4 minutes to cut a single mold, the volume of material wasted was equal to the volume of the structure. Another disadvantage of the method is that concrete placement can only be done

horizontally. Thus, formwork for complex topologies involving non-planar and non-parallel opposite sides would be difficult to fabricate. This limitation was also observed in the construction of a 13 by 16 by 7 ft, 3 in. thick shell (Figure 2.4(b)). The fabrication of formwork took 10 days using a CNC router to cut the expanded polystyrene (EPS) foam.

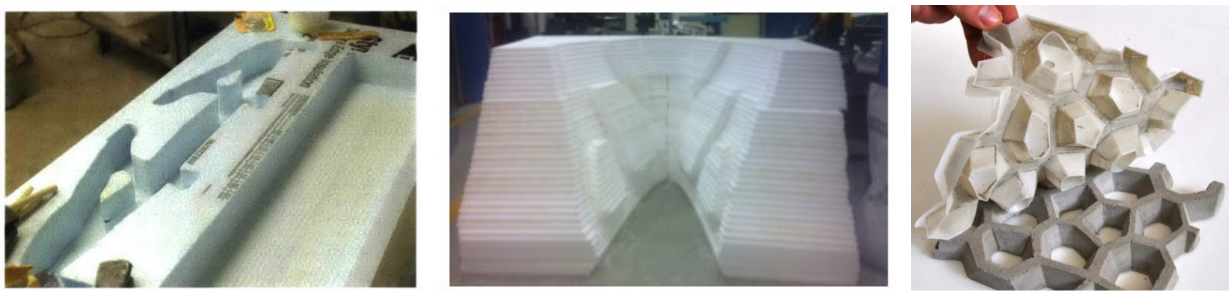

(a) (b) (c)

Figure 2.4: Formwork fabrication using (a) ONSRUD Mill (Jewett, 2018), (b) CNC Router (Vazquez et al., 2014), and (c) 3D Printer (Peters, 2014)

Peters (2014) experimented with malleable polymers made from flexible plastic filaments as a mold (Figure 2.4(c)). These were fabricated using a desktop 3D printer. Although promising, the method needs development in terms of (1) fabricating large formwork, (2) casting concrete with coarse aggregates, (3) reinforcement placement, and (4) incorporating either additional bracing or increased thickness of formwork to withstand hydrostatic forces in case of walls or columns. This investigation is aimed at addressing the issues of reinforcement placement, and fabrication of formwork for walls including effects of hydrostatic pressure.

CHAPTER 3 - EXPERIMENTAL WORK

Two RC walls, called Control Wall (CW) and Optimized Wall (OW), were tested under a monotonic lateral load until failure. These tests were conducted to demonstrate the feasibility of using additive manufacturing to produce functional formwork and to provide a basis for calibrating models described in Chapter 5. Both specimens were constructed with base and top blocks. The base block simulated the foundation of a structural wall and was used to secure the wall to the strong floor of the structural laboratory. A 55-kip hydraulic actuator was connected to the top block to apply lateral loads. The lateral force was applied at an elevation of 60 in. above the base block, resulting in an aspect ratio of 4 for both walls.

3.1 Specimen Design

3.1.1 Control Wall

The reinforcement used for the control specimen is shown in Figure 3.1. The control specimen was designed so its lateral strength would be limited by flexure using concrete with a target compressive strength of 6,000 psi and Grade 36 reinforcement (see Section 3.2). Flexural reinforcement consisted of ten No. 2 bars in each of the boundary elements near the edges of the wall. Vertical web reinforcement consisting of two 12-gauge wires (diameter of 0.106 in.) at a 3 in. spacing also contributed slightly to the wall flexural strength. The nominal flexural strength of the wall, calculated using the rectangular stress block described in ACI 318-14 and specified material properties, and considering the section to be doubly reinforced, was 418 kip-in. The nominal flexural strength of the wall resulted in a shear force demand close to 7 kips, or $3\sqrt{f'_c}hl_w$, where f'_c is specified concrete compressive strength in psi, h is the wall thickness, and l_w is the wall length.

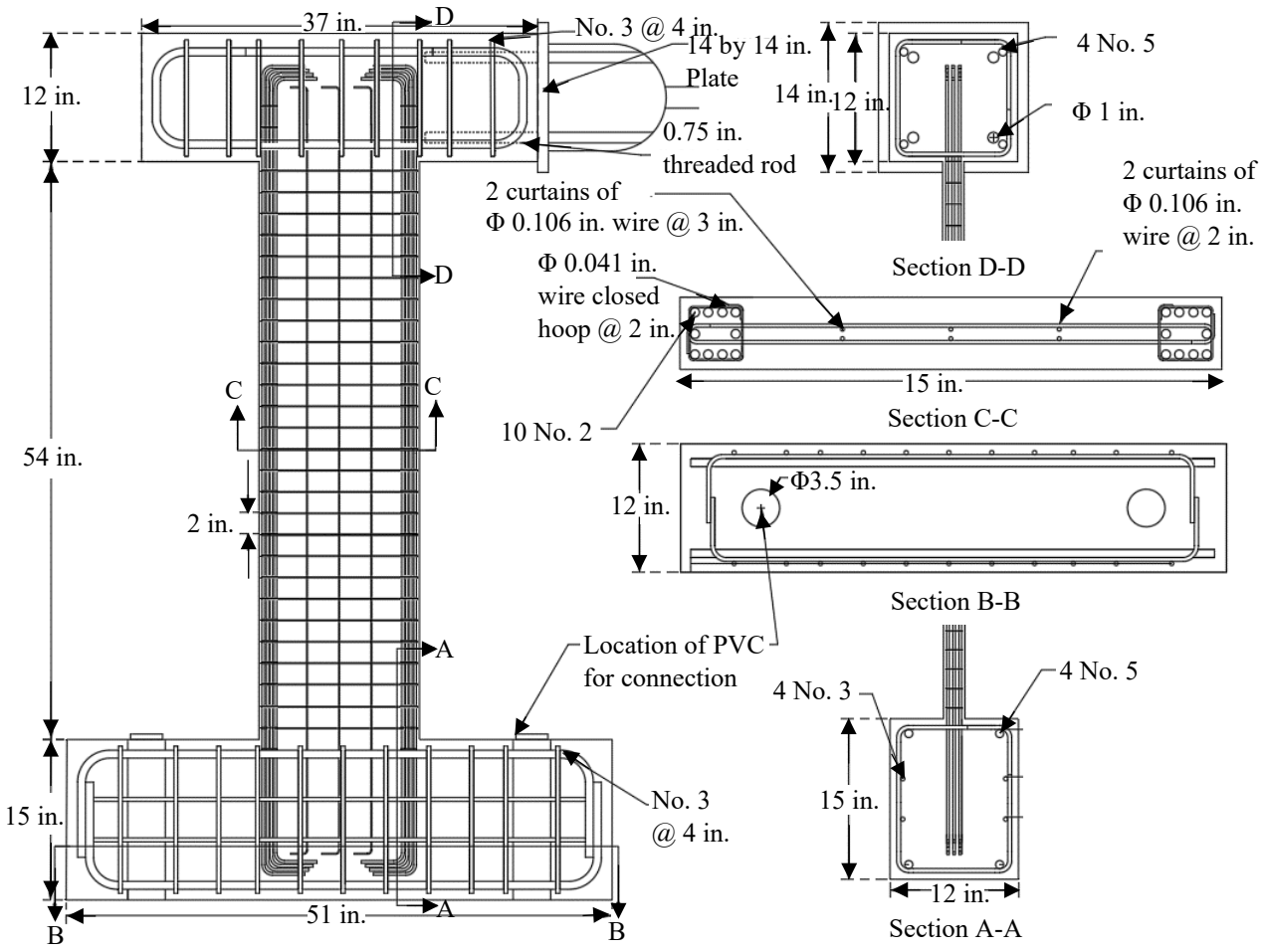

Figure 3.1: Reinforcement details of control wall specimen

The horizontal shear reinforcement was designed so the sum of the nominal shear strengths attributed to the concrete (Eq. 3.1) and steel (Eq. 3.2) exceeded the shear demand associated with a base moment of 418 kip-in. Two 12-gauge wires (diameter of 0.106 in.) were provided at 2 in. spacing (l_w/7.5) throughout the height of the wall. This resulted in a nominal shear strength of 7.1 kips and a horizontal reinforcement ratio of 0.0044, which exceeds 0.0025, the minimum horizontal reinforcement ratio required in Section 11.6.2 of ACI 318-14. Vertical web reinforcement consisted of two 12-gauge wires (diameter of 0.106 in.) at a 3 in. spacing. This resulted in a vertical web reinforcement ratio of 0.0029, which exceeds 0.0025, the minimum vertical web reinforcement ratio required in Section 11.6.2 of ACI 318-14. Longitudinal

reinforcement near the edges of the wall was enclosed by 19-gauge wires (diameter of 0.041 in.) at a 2 in. spacing. This spacing satisfied the requirements of ACI 318-14 Section 25.7.2.1 for maximum tie spacing.

$$V_c = \left[0.6\lambda\sqrt{f'_c} + \frac{l_w\left(1.25\lambda\sqrt{f'_c}+\frac{0.2N_u}{hl_w}\right)}{\frac{M}{V_u}-\frac{l_w}{2}}\right] hd_1 \quad \text{Eq. 3.1}$$

$$V_s = \frac{A_v f_{yt} d_1}{s} \quad \text{Eq. 3.2}$$

Where: V_c is the nominal shear strength attributed to concrete, V_s is the nominal shear strength attributed to steel (which must not be less than V_u/ϕ - V_c, where the strength reduction factor ϕ was taken as 1.0 in this study), f'_c is the specified concrete compressive strength, λ is modification factor for lightweight concrete (equals one for normal weight concrete), h is wall thickness, d_1 is the distance from the extreme compression fiber to the centroid of longitudinal tension reinforcement (taken as 14 in.), N_u is the factored axial force normal to the cross-section (assumed to be zero), l_w is the length of the wall, V_u is the shear demand on the wall (taken as 7 kips), M is the base moment demand (taken as 420 kip-in.), A_v is the required area of shear reinforcement, f_{yt} is the specified yield stress of transverse reinforcement, and s is the longitudinal spacing of shear reinforcement.

3.1.2 Optimized Wall

Since the experimental investigation was carried out early in this study, and because its main purposes were to provide a (1) proof of concept that demonstrated the feasibility of using 3D-printed formwork and (2) benchmark for validating computational models, a relatively simple "optimized" geometry was used that was based on a strut-and-tie model. The resulting structure satisfied equilibrium assuming each member resisted either tension or compression only. Strut-

and-tie models represent complex stress distributions within structures as a system of struts, ties, and nodes that comprise a truss. These are not normally used for structural topology optimization, and the authors do not intend to imply strut-and-tie models should be used for this purpose.

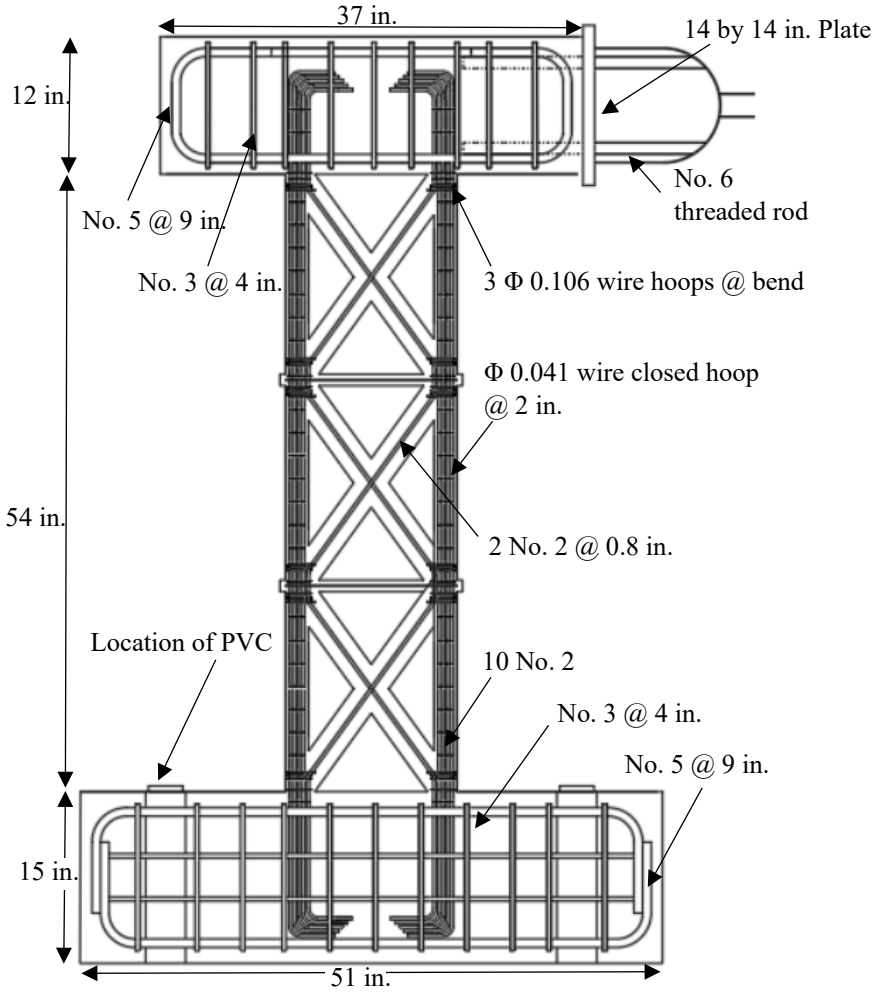

Figure 3.2: Reinforcement details of optimized wall specimen (top and base block reinforcement are the same as shown in Figure 3.1)

A simple truss model was used to solve for internal member forces that result from a 7 kip lateral force applied at the top of the wall. A 7 kip force was used because it is close to the expected lateral strength of the control specimen based on its nominal flexural strength. All the members had a concrete compressive strength of 12,000 psi and modulus of elasticity as $57000\sqrt{f'_c}$. Members stiffness was not modified to account for cracking. The base was fixed in translation and rotation.

For simplicity, member joints were modeled as pin connections, including joints between inclined members near mid-depth of the cross-section.

Truss members were designed using concrete with a specified compressive strength of 12,000 psi and Grade 36 reinforcing bars. Figure 3.2 shows the reinforcement layout used for the optimized wall specimen. The boundary elements/columns in the truss had two-inch-square cross-sections reinforced with ten No. 2 bars, the same as for the control wall. Inclined members had an oval cross-section with minor and major diameters of 2 and 2.5 in., resulting in an area of 3.9 in.^{2}. Since several inclined members were ties, two No. 2 bars were provided in each to provide the necessary strength. Each truss member had a calculated axial strength (based on concrete and reinforcement in compression and only reinforcement in tension) that was larger than the calculated internal force demand, and sometimes considerably so. For example, the calculated strength in compression of the inclined members was 50.3 kips, which was sufficient to carry the entire shear demand. The inclined tension members were therefore not needed for strength. This was done because the inclined members under compression were expected to carry most of the shear force after cracking of the inclined members in tension, a process that was not accounted for in the rudimentary model used to find the internal forces. The calculated strength of these ties in tension, based on bar area and the specified yield stress, was 4.9 kip, approximately equal to the estimated demand based on the model. For ease of construction and symmetry, the two No. 2 bars were also provided in the inclined struts.

Confinement of longitudinal reinforcement in the vertical elements consisted of continuously wound 19-gauge wires (diameter of 0.041 in.) at a 2 in. spacing. The joints between inclined and vertical members required additional transverse reinforcement to tie the inclined No. 2 bars into the group of vertical bars: three 12-gauge wire hoops were provided at the bend. Reinforcement in

the horizontal members (slabs) consisted of a closed 12-gauge wire hoop (diameter of 0.106 in.) with two legs.

Not counting the top and base blocks, this "optimized" wall had a volume that was 57% of that of the control specimen, but the weight of reinforcement in this specimen was 7.4% greater than in the control specimen.

Because the aim of these tests was to (1) demonstrate the feasibility of constructing cast-in-place structures with 3D-printed formwork and (2) provide a basis for calibrating the stiffness of linear models, the failure mode of the optimized wall was not a major concern in design. Clearly, if such a structure were to be constructed in practice, superior detailing would be necessary to ensure adequate deformation capacity and control of undesirable failure modes.

3.1.3 Top and Base Blocks

The base blocks had dimensions of 12 by 15 by 51 in. and the top blocks had dimensions of 12 by 12 by 37 in. They were reinforced as shown in Figures 3.1 and 3.2. These were constructed with concrete having a compressive strength of 6000 psi and Grade 60 reinforcement. Wall reinforcement, which had 90 degree hooks at both ends, was extended 9, 8.3, and 7.6 in. into the top block and 12.7, 12, and 11.3 in. into the base block. Three dimensions are provided for each end because the hooks were nested, as shown in Figure 3.2. These embedment lengths (l_d) were longer than the straight bar development length calculated using Eq. 3.3, which was proposed by Feldman, Poudyal, and Cairns (2018) for smooth reinforcing bars. In Eq. 3.3, c_b is the distance between the centroid of the lapped/anchored bar and the nearest concrete surface; d_b is the nominal bar diameter; ψ_t is the top-cast factor (2.5 for bars in top-cast position and 1.0 for bottom-cast bars). Hooks were provided in addition to satisfying this calculated length because this equation

was not intended for use on small diameter wires and the possible effect of scale was outside the scope of this study.

$$\ell_d = \frac{0.877 \times \psi_t \times d_b}{\sqrt{c_b/d_b}} \times \frac{f_y}{\sqrt{f'_c}} \quad \text{Eq. 3.3}$$

3.2 Materials

3.2.1 Concrete

The base and top blocks of both specimens and the entire control wall were cast using normal strength concrete with a target compressive strength of 6000 psi. The concrete was mixed in the structural laboratory using a 9 cu. ft. barrel mixer. The optimized wall was cast using high strength concrete with a target compressive strength of 12000 psi that was mixed in a bucket because the batch quantities were very small. The optimized wall was cast using high strength concrete to improve its strength and stiffness and to partially compensate for the section loss caused by openings. The walls were cast in three lifts on separate days.

The mixture proportions used for the two specimens are listed in Table 3.1 assuming SSD conditions for all aggregates. The batch quantities were adjusted to account for the surface moisture content of the sand obtained using the ASTM C566 procedure. The normal strength mortar was designed for a compressive strength of 6000 psi and a slump of 6 to 7 in. It had a water/cement ratio of 0.57. The mixture design for the high strength mortar was based on one reported by Wille and Boisvert-Cotulio (2013), with quantities of admixtures modified based on trial batch results. For all batches, a viscosity modifying admixture (VMA 358) was used to reduce segregation and two high-range water reducers (ADVA 190 and ADVA 405) were included to obtain flow-able concrete with a spread between 20 and 25 in. for ease of constructability. Trial batches were used to optimize the mixture proportions.

Table 3.1: Concrete mixture proportions

	Control Wall		Optimized Wall	
	(lb/yd^3)	**Proportions by Weight**	**(lb/yd^3)**	**Proportions by Weight**
Cement [1]	719	1.0	1430	1.0
Sand [2]	2698	3.75	1187	0.83
Water	410	0.57	402	0.28
Fly Ash [3]	-	-	343	0.24
Silica Fume [4]	-	-	357	0.25
VMA 358 [5]	0.9	0.001	-	-
ADVA 190 [6]	3.0	0.004	58	0.041
ADVA 405 [6]	-	-	57	0.04

[1] Type I/II Portland cement compliant with ASTM C150. [2] Kansas River Sand (with gradation shown in Table 3.2). [3] Class C Fly Ash compliant with ASTM C618. [4] Compliant with ASTM C1240. [5] Admixture is compliant with ASTM C494/C494M for type S admixtures. [6] Admixture is compliant with ASTM C494/C494M for type A and F, and ASTM C1017 type I.

Mortar was used instead of concrete to accommodate the small scale of the specimens. The maximum aggregate size was restricted to 0.2 in. Locally available raw materials were used for both of the mortar mixtures.

Table 3.2: Sieve analysis report for fill sand

Sieve #No.	**Sieve Size (in.)**	**Empty mass of sieve (lb)**	**Total mass of sieve (lb)**	**Mass Retained (lb)**	**% Retained**	**% Retained Cumulative**	**% Passing**
4	0.19	1.10	1.10	0	0.02	0.02	100
8	0.09	1.01	1.02	0.01	0.5	0.5	99.5
16	0.05	0.97	1.58	0.61	27.6	28.2	71.9
30	0.02	0.89	2.07	1.18	53.2	81.4	18.7
50	0.015	1.00	1.39	0.39	17.8	99.1	0.9
130	0.01	0.92	0.94	0.02	0.8	99.9	0.05
200	0.003	0.72	0.72	0	0.04	100.0	0.01
	Pan	0.81	0.81	0	0.01	100.0	0.0
	Total			2.2	100.0		

The mixing procedure for the normal-strength mortar consisted of: (1) adding batch quantities of water and ADVA 190 to the mixer and running it at a constant speed, (2) adding batch quantities

of sand and cement to the mixer and mixing until the desired fluidity and consistency was reached (based on visual inspection), and lastly (3) adding VMA 358.

The mixing procedure for the high-strength mortar consisted of: (1) mixing the ADVA 190 and water and setting the blend aside, (2) adding batch quantities of silica fume and sand and mixing with a constant speed until blended, (3) adding batch quantities of cement and fly ash and mixing until blended, (4) adding the mixture of water and ADVA 190 and mixing for 1 minute, and lastly (5) adding ADVA 405 and mixing with increased speed until the desired fluidity and consistency was reached.

Plastic mortar properties are reported in Table 3.3. The measured concrete compressive strengths obtained from standard concrete cylinders tested in accordance with ASTM procedures are listed in Table 3.4. The average concrete compressive strengths of the control and optimized walls on the day of testing were 6400 and 11100 psi.

Table 3.3: Plastic mortar properties

		Control Wall			**Optimized Wall**		
		Temp. [1] **(°F)**	**Spread** [2] **(in.)**	**Concrete Density** [3] **(lb/ft^3)**	**Temp.** [1] **(°F)**	**Spread** [2] **(in.)**	**Concrete Density** [3] **(lb/ft^3)**
Base	Lift 1	60	20	145.0	58	25	141.6
Block	Lift 2	64	18	148.4	61	28	144.3
	Lift 3	63	15	143.6	60	27	145.4
Wall	Lift 1	60	25	144.6	-	-	-
	Lift 2	66	24	143.6	-	-	-
	Lift 3	65	22	146.0	-	-	-
Top	Lift 1	52	20	144.3	59	24	146.7
Block	Lift 2	50	21	144.4	58	22	145.0

[1] Temperature of freshly mixed concrete following ASTM C1064. [2] Slump flow (spread) of self-consolidating concrete following ASTM C1611. [3] Density of freshly mixed concrete determined following ASTM C138.

Table 3.4: Measured concrete compressive strengths

		Control Wall				Optimized Wall			
		Cast Date	**Test Date**	**Age (Days)**	**f'_c [1,2] (ksi)**	**Cast Date**	**Test Date**	**Age (Days)**	**f'_c [1] (ksi)**
Base Block	Lift 1	11/15/17	12/13/17	28	5.6	11/21/17	12/19/17	28	6.9 [2]
			05/15/18	181	4.8		08/07/18	259	6.4 [2]
	Lift 2	11/15/17	12/13/17	28	5.5	11/21/17	12/19/17	28	6.3 [2]
			05/15/18	181	5.1		08/07/18	259	6.6 [2]
	Lift 3	11/15/17	12/13/17	28	5.5	11/21/17	12/19/17	28	6.2 [2]
			05/15/18	181	4.8		08/07/18	259	6.0 [2]
Wall	Lift 1	12/05/17	01/02/18	28	6.6	02/13/18	03/13/18	28	10.7 [3]
			05/15/18	161	6.4		08/07/18	175	11.3 [3]
	Lift 2	12/08/17	01/05/18	28	6.4	02/19/18	03/26/18	35	10.6 [3]
			05/15/18	158	6.4		08/07/18	169	11.1 [3]
	Lift 3	12/12/17	01/09/18	28	6.7	02/25/18	03/26/18	29	9.6 [3]
			05/15/18	154	6.5		08/07/18	163	10.8 [3]
Top Block	Lift 1	03/13/18	05/15/18	63	5.9	03/13/18	08/07/18	147	5.9 [2]
	Lift 2	03/13/18	05/15/18	63	5.8	03/13/18	08/07/18	147	6.0 [2]

[1] Concrete compressive strength following ASTM C39. [2] Reported values based on average of three 4 by 8 in. cylinders. [3] Reported values based on average of three 3 by 6 in. cylinders.

3.2.2 Steel

The specimens had No. 2 hot-rolled smooth steel bars as longitudinal reinforcement and low-carbon steel wire as vertical and horizontal web reinforcement. The No. 2 bars were compliant with ASTM A36. Their mechanical and chemical properties were obtained from certified mill test reports and are listed in table 3.5. The low-carbon steel wires were compliant with ASTM A853 and had a tensile strength (ultimate) of 70,000 psi.

Table 3.5: Material properties of wall longitudinal reinforcing bars based on mill certifications

Mechanical Properties		Chemical Composition	
Density	0.284 lb/in^3	**Carbon (C)**	0.29 %
Tensile Strength (ultimate)	79,800 psi	**Copper (Cu)**	>=0.2 %
Tensile Strength (yield)	36,300 psi	**Iron (Fe)**	98 %
Elongation at Break	20% - 23%	**Manganese (Mn)**	0.8 – 1.2 %
Modulus of Elasticity	29000 ksi	**Phosphorous (P)**	0.04 %
Poisson Ratio	0.3	**Silicon (Si)**	0.15 – 0.4 %
Shear Modulus	11,500 ksi	**Sulfur (S)**	0.05 %
Bulk Modulus	23,200 ksi		

Since the bars and wires were smooth, an effort was made to corrode their surfaces to increase their roughness and improve their bond with the concrete. The No. 2 hot-rolled steel bars and low-carbon steel wires were sprayed with a 10% hydrochloric acid (HCl) solution and placed in fog room (with a relative humidity near 100%) for 7 days. This was similar to a process used by Moehle and Sozen (1978). The loose scale was later removed using a wire brush before assembly and concrete placement. Figure 3.3 shows the effect of this treatment on a No. 2 bar.

Figure 3.3: Reinforcing bars before (left) and after (right) the HCL treatment

3.2.3 3D Printed Formwork Material

PLA (polylactic acid) 3D printing filament was used to fabricate the optimized wall formwork. A spool weighing 2.2 lb with a filament diameter of 0.069 in. (tolerance +/- 0.001 in.) was used. To characterize the mechanical properties of the printed material, twelve 3.5-in.-long specimens were tested under three-point and four-point bending. Six of the twelve specimens had dimensions of 0.8 by 0.25 in. and were tested under three-point bending. These were printed in either the longitudinal or transverse directions: in other words, the joint between layers was either in the plane with dimensions of 0.8 by 3.5 in. or 0.8 by 0.25 in., respectively (shown in Fig. 3.4(a) and 3.4(b)). The remaining six specimens with dimensions of 0.8 by 0.125 in. were printed in the longitudinal direction and tested under either three- or four-point bending.

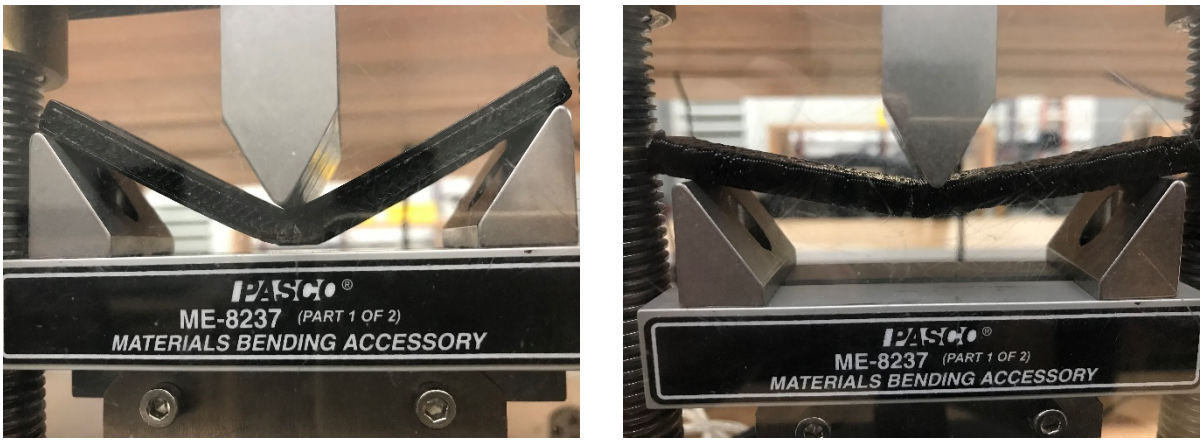

(a) (b)

Figure 3.4: 3D printed test specimens under three-point bending test. Specimen printed so the joint between layers was (a) in the vertical plane parallel to the longitudinal axis and (b) in the vertical plane perpendicular to the longitudinal axis

Equation 3.4 was used to calculate the strain in the extreme fiber at every data point. Similarly, Eq. 3.5 was used to compute tensile stresses in the extreme fiber at every data point. The tensile stresses corresponding to maximum moment, σ_{t_max}, are reported in Table 3.6. The measured loads and displacements were not proportional, even early in the test. The effective modulus of elasticity was computed as the slope of line joining points corresponding to 0.1 σ_{t_max} and 0.5 σ_{t_max} on the

stress-strain curves. The maximum tensile stress in specimens printed such that the joint between layers was perpendicular to the longitudinal axis (in the transverse direction) was only about one-quarter that of specimens printed in the longitudinal direction.

Three-point bending: $\varepsilon = {}^{48I\delta\sigma_t}/_{PL^3}$ Eq. 3.4a

Four-point bending: $\varepsilon = {}^{48I\delta\sigma_t}/_{Pa(3L^2 - 4a^2)}$ Eq. 3.4b

$\sigma_t = {}^{My}/_{I}$ Eq. 3.5

Where: P is the applied point load, L is the span between support centerlines (3.5 in.), a is the distance between the centerline of a point load and the nearest support in the four-point bending test ($a = L/3$), I is the moment of inertia based on nominal dimensions, δ is the deflection at mid-span, y is the distance between the extreme tension or compression fiber and the neutral axis based on nominal dimensions, and M is the moment at mid-span.

Table 3.6: Mechanical properties of 3D printed specimen

	3-Point Bending			4-Point Bending
	0.125 in. L [1,2]	0.25 in. L [1,2]	0.25 in. T [2,3]	0.125 in. L [1,2]
Maximum Stress in Extreme Tension Fiber (σ_{t_max})	9.8 ksi	8.8 ksi	2.5 ksi	9.1 ksi
Effective Elastic Modulus (E)	370 ksi	300 ksi	140 ksi	450 ksi

[1] Specimens printed longitudinally. [2] Reported values based on an average of three tests.
[3] Specimens printed transversely.

3.3 Construction

3.3.1 Formwork Design

The control wall specimen and the top and base blocks were constructed using traditional plywood formwork.

The formwork for the optimized wall was fabricated using a 3D printer. The size of the available printer was a restriction for formwork design. The printer had a 16 by 16 in. base plate and a total height available for printing of 21 in. Therefore, the height of the wall was split in three parts, with each part not exceeding a height of 18 in (shown in Fig. 3.5). Each part was also split in half along a vertical plane parallel to the wall to allow for placement of reinforcement.

A uniform formwork wall thickness of 0.125 in. was used throughout. The dimension was selected based on initial trials. The thickness was also selected such that the volume required to print one subpart of formwork was less than the volume of a spool of Polylactic Acid (PLA), the material used to print the formwork.

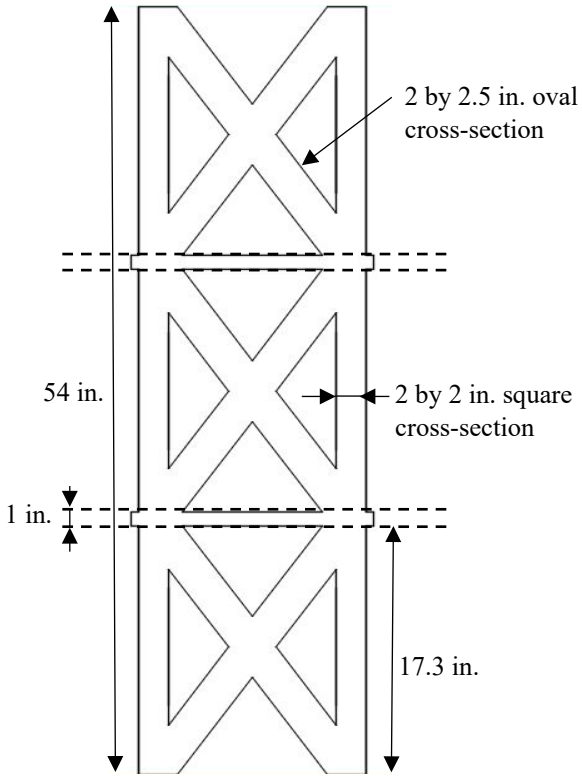

Figure 3.5: Parts of optimized wall divided to accommodate printer limitations on height of printed parts

The formwork was initially printed with sharp corners similar to conventional wood formwork. It became apparent during initial trials that stress concentrations at the sharp corners of the formwork produced weak spots prone to fracture during concrete placement. Hence, all edges and joints between members (e.g. the inclined member-to-boundary element joint) were smoothed by increasing the radius of the corners. The minimum radius necessary for 3D printed formwork will depend on the materials, demands, and additive manufacturing procedures employed.

To join the sides of the formwork, each edge was extended (Figure 3.6(a)) to allow for application of epoxy at the joint. Some of the extensions also had holes to accommodate zip-ties to reinforce the connection. If 3D printed formwork is to be reused in practice, a different connection type (perhaps bolting) would be required.

The formwork (Figure 3.6(a)) was printed up-side down for convenience. The large flat printed area in contact with the printer surface in Figure 3.6(b) provided a firm connection with the printing table during printing and provided a convenient surface for supporting the slabs (Figure 3.7) located near the 1/3 points of the vertical span. Formwork for the sides of the slabs was printed separately (Figure 3.7) and epoxied to the supporting wall formwork.

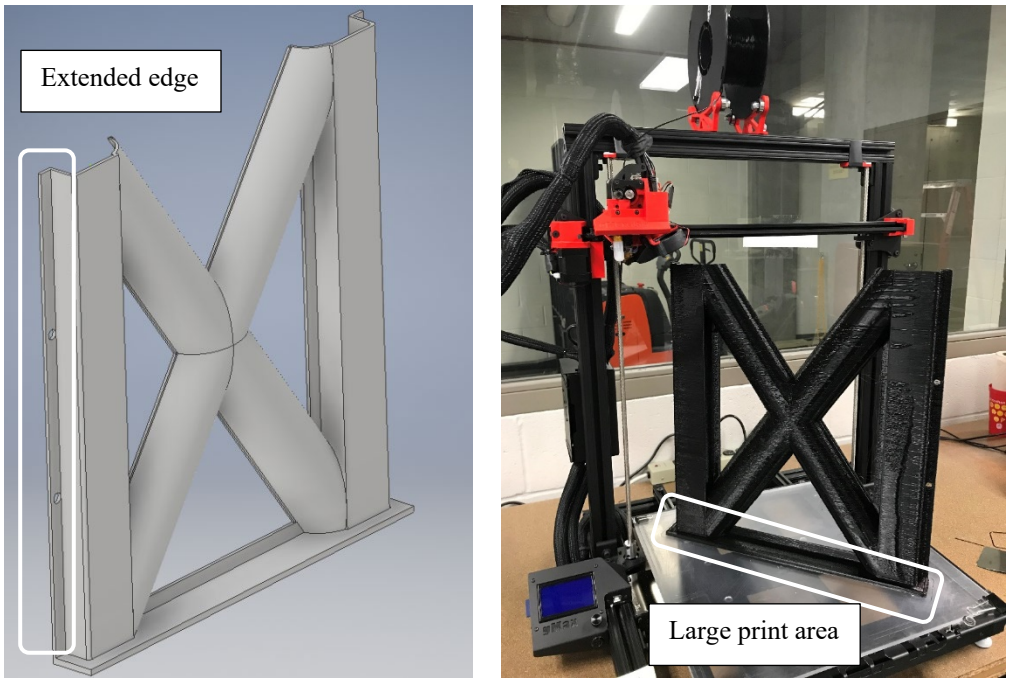

(a) (b)

Figure 3.6: (a) Lift 1 Formwork designed in AutoCAD Inventor and (b) Lift 1 subpart being printed

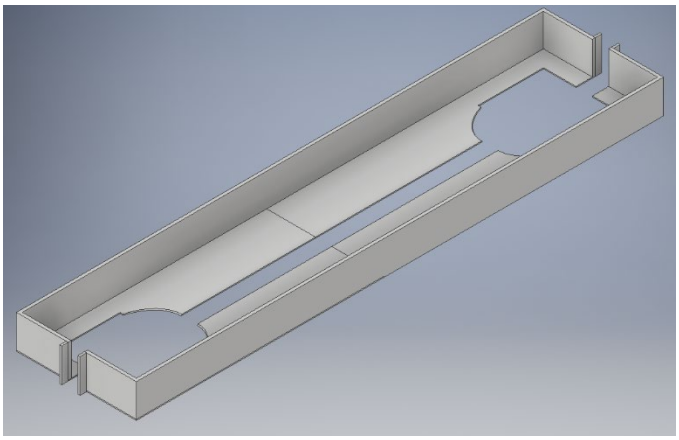

Figure 3.7: Slab formwork

The formwork was drawn in AutoCAD Inventor and exported as a stereo lithography (STL) format to Slic3r, which was used to convert the file to 3D printer readable format (gcode). After printing, the 3D printed formwork was coated with a single layer of a liquid rubber spray to seal small gaps between printed layers, if any existed. Such gaps occasionally occurred where interlayer bonding was incomplete. Caulk was applied at every joint after the pieces were epoxied together. Plywood pieces and clamps were used to hold the formwork together until the epoxy set (as described in Section 3.3.2). The oval shaped inclined members were held together using zip ties. Clay was used to seal minor leaks observed during concrete placement.

3.3.2 Construction Sequence and Reinforcement Placement

Construction began with erection of the reinforcement for the base block and wall specimen, followed by preparation and assembly of the base-block formwork and then concrete placement (Figure 3.8). The walls were then cast in three lifts, each consisting of formwork assembly followed by concrete placement (Figure 3.9). The wall formwork was then removed, and the top block was then constructed using normal sequencing (assembly of reinforcement, formwork, and false work to support it (Figure 3.10), and placement of concrete). The fresh concrete was covered with wet burlap and plastic sheets for 1 to 5 days after each placement.

(a)

(b)

(c)

(d)

Figure 3.8: Construction process for the base block of the control wall specimen (a) reinforcement cage braced by cables, (b) assembled formwork, (c) concrete after placement, covered with burlap and plastic sheets, and (d) after formwork removal. The diagonal reinforcement was used as temporary bracing during construction that was removed before placement of concrete.

Figure 3.9: Construction process for Lift 2 of the optimized wall specimen (a) formwork subpart and reinforcement, (b) assembled formwork, (c) plywood support during epoxy set, and (d) after concrete placement.

Figure 3.10: Support structure/falsework and formwork for top block in control (left) and optimized walls (right)

The reinforcement cage for each specimen was constructed such that the wall was cast in the upright position. The reinforcement was held in position with steel cables anchored to the floor and tightened with turnbuckles. The No. 2 inclined bars were also braced to minimize out-of-plane translation of longitudinal reinforcement during concrete placement. To hold the longitudinal reinforcement in position at such small scales, a spacer was designed and fabricated using a 3D printer (Figure 3.11). The spacers were 2 by 2 by 0.25 in. for the control wall and 2 by 2.5 by 0.25 in. for the optimized wall. The spacers were placed above the top of each lift and removed before the next lift was placed such that no spacers were cast into the concrete.

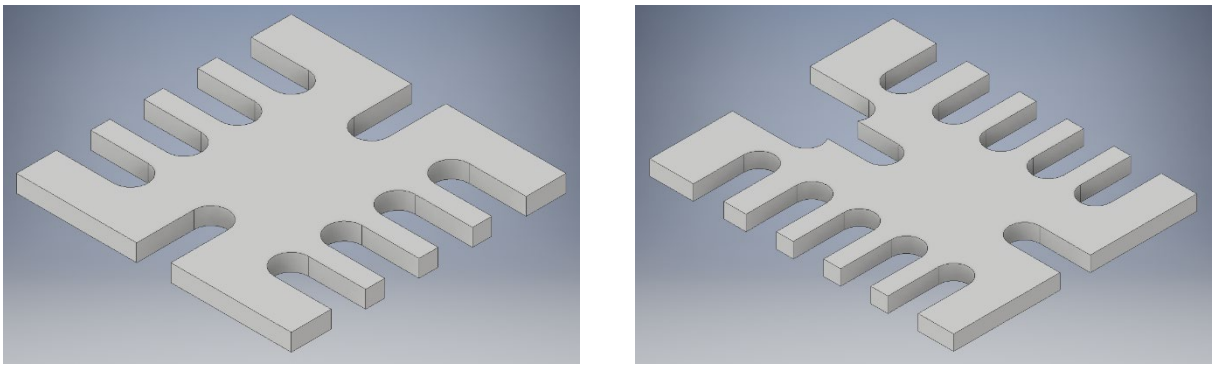

Figure 3.11: Reinforcement spacers for control wall (left) and optimized wall (right)

3.4 Test Setup

Figure 3.12 is a photo of a specimen during testing. The specimens were bolted to the laboratory strong floor using two 2.5 in. diameter threaded rods and hex-nuts. To avoid concrete crushing at the junction of the hex-nut and base block, 1 in. thick square plates were used as washers below the hex-nut. The 55-kip hydraulic actuator, which applied only bearing (compressive) force, was supported and aligned with the top block with threaded rods partially cast into the top block. The actuator had a stroke length of +/- 20 in.

A steel frame, comprised of 2.5 by 2.5 by 0.25 in. tubular columns and 2.5 by 2.5 by 0.25 in. angle sections, was used to brace the slender walls against out-of-plane displacements and twisting. The columns were connected in the plane of the wall to the ends of the base block using zinc plated 0.625-in. diameter 7-in. long steel wedge concrete anchors. The angle sections, oriented horizontally and bolted to the vertical tubes, were located 25 and 50.5 in. from the top of the base block (measured to the centerline of the angle). To minimize friction between the angle sections and the concrete walls, 0.0625-in. thick mirror-finished steel plates were welded to the face of the angle sections and 0.25-in. thick nylon pads were glued to the walls. Spacers were used where the angles were bolted to the vertical tube, as needed, to accommodate the thickness of these friction-

reducing elements. The system of mirror-finished plate and nylon pads provided minimal frictional resistance to the in-plane movement of the specimens but provided out-of-plane restraint.

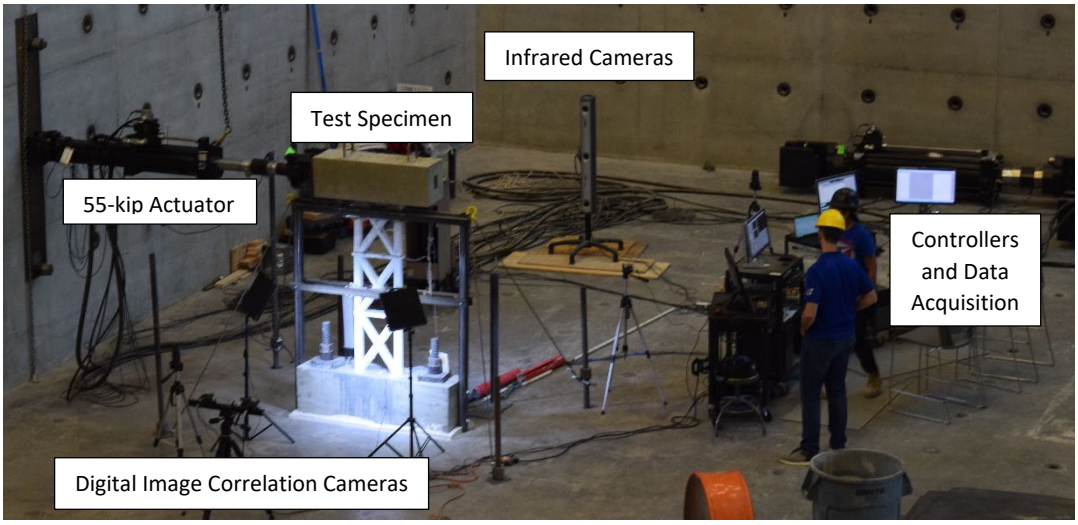

Figure 3.12: Photo of test setup

3.5 Instrumentation

Before mounting the external instrumentation, the surface of the specimens was painted white to improve the visibility of cracks (Figure 3.13).

The load cell within the actuator was used to measure force.

Several 120-ohm foil-type strain gauges were applied to the reinforcement at the locations shown in Figure 3.14 to measure axial reinforcement strains. The control wall had 8 strain gauges on the longitudinal bars near the wall edges, while the optimized wall had 6 gauges on the inclined bars in addition to 8 gauges on the longitudinal bars.

The lateral deflection, flexural rotations, and shear deformations of the specimens were calculated using data collected with a non-contact infrared-based system that tracks the positions in space of individual markers glued to the specimen surface (Figure 3.15). The control wall specimen had 53 markers on the wall, 7 on the base block, and 5 on the top block. Three markers were placed on

fixed surfaces as a reference. Among the markers on the wall, three were inactive during testing due to supporting frame interference. The optimized wall specimen had 59 markers on the wall, 9 on the base block, and 5 on the top block. Similar to the control wall specimen, during testing four markers were inactive.

Deformations were also recorded using digital image correlation (DIC). The system used required that the specimens be painted white and then speckled with black paint (Figure 3.16). The control wall was speckled over its entire height, although the largest deformations occurred near the base of the wall, as expected. Expecting a similar response in the optimized wall, only lift 1 (level 1) of the optimized wall was speckled with black spray paint. This allowed higher resolution data collection within that area.

Additionally, two cameras were used to record time-lapse videos of the tests.

(a) (b)

Figure 3.13: Surface prepared for crack detection and instrumentation

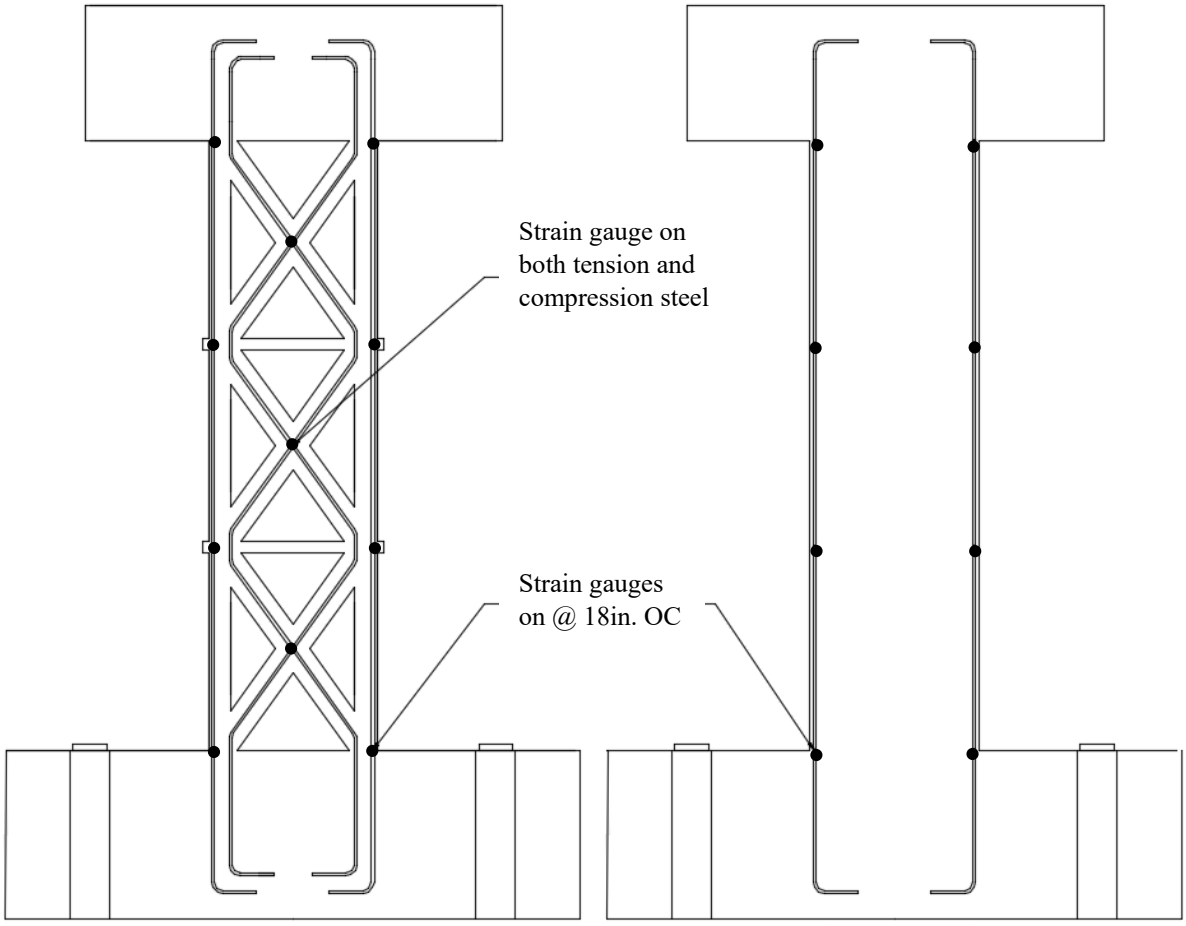

Figure 3.14: Strain gauge locations in (a) optimized and (b) control wall specimens (only the instrumented reinforcement is shown for clarity)

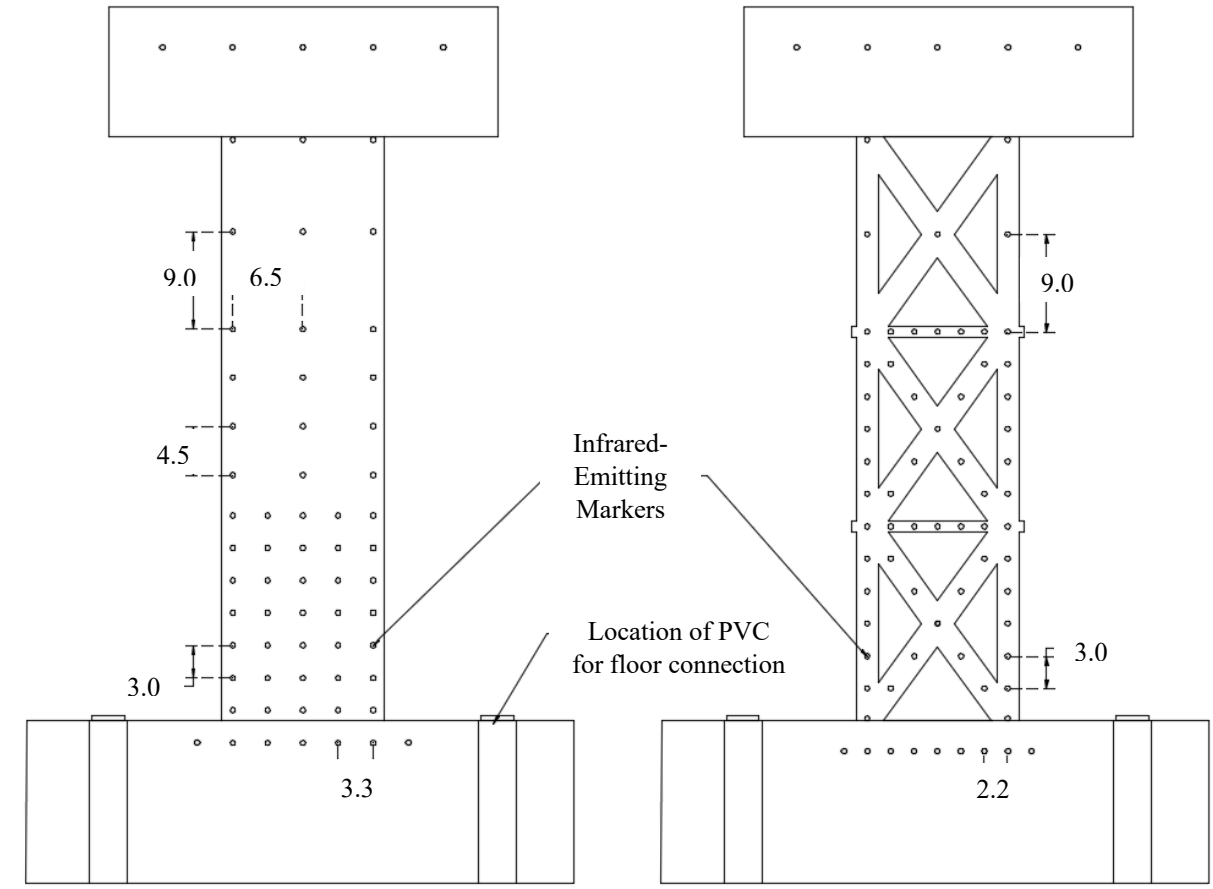

Figure 3.15: Infrared-emitting markers on the control wall specimen (a) nominal (b) actual, and optimized wall Specimen (c) plan and (d) actual

(a)

(b)

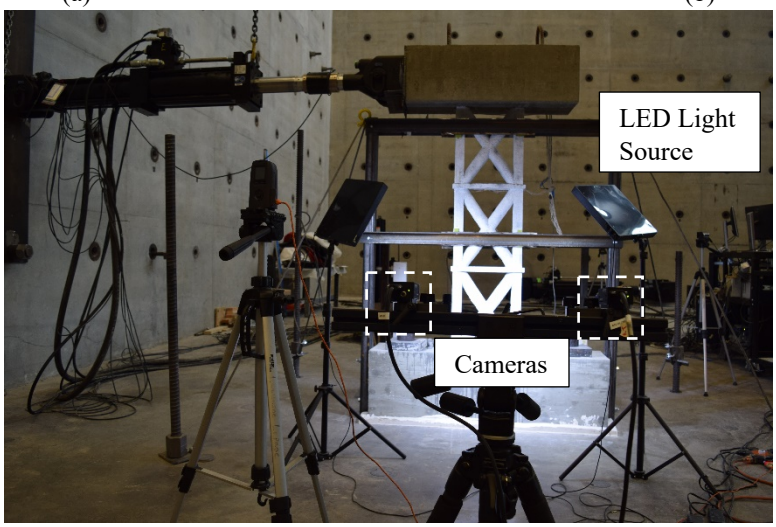

(c)

Figure 3.16: Digital image correlation (DIC) (a) speckle pattern for control wall, (b) speckle pattern for optimized wall, and (c) setup for DIC using two cameras

CHAPTER 4 - EXPERIMENTAL RESULTS

4.1 Measured Shear Force versus Top Displacement

Figure 4.1 shows measured shear versus lateral displacement for the two specimens tested. The reported lateral displacement was obtained from the measured lateral displacement of the top block by subtracting the effects of base block translation and rotation. The expression used to calculate the lateral displacement, δ, is given by Eq. 4.1.

$$\delta = \delta_{top} - \delta_{base} - \left(\theta_{top} l_t\right) - \left(\theta_{base} l_b\right) - \left(\theta_{base} h_w\right) \quad \text{Eq. 4.1}$$

Where δ_{top} is the translation of the top block estimated based on the translation of markers located approximately 3 in. above the line of action of the actuator, δ_{base} is the translation of the base block estimated based on the translation of markers located approximately 3 in. below the top of base block, θ_{top} is the rotation of the top block about an axis normal to the plane of the wall, calculated using the two markers on the top block located furthest from the specimen centerline, l_t is the vertical distance between the line of action of the actuator and line of markers on top block (3 in.), θ_{base} is the rotation of the base block about an axis normal to the plane of the wall, calculated using the two markers on the base block located furthest from the specimen centerline, l_b is the vertical distance between the top of base block and the line of markers on base block (3 in.), and h_w is the vertical distance between the top of the bottom block and the line of action of the actuators.

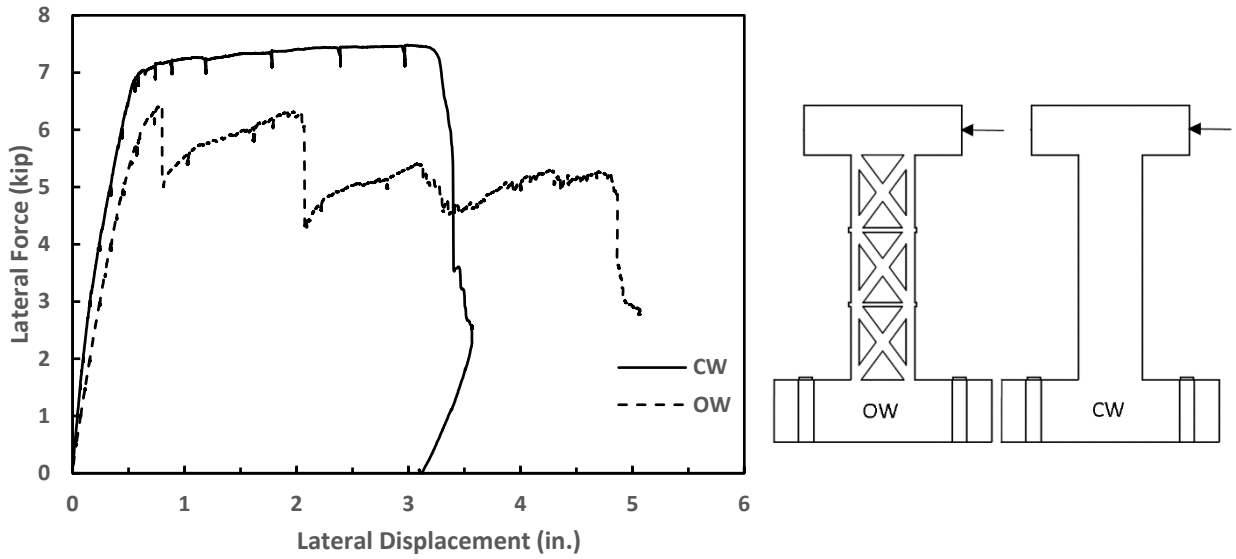

Figure 4.1: Measured lateral force (shear) versus lateral displacement

Figure 4.1 shows that the optimized wall was less stiff and less strong than the control wall, but that both specimens experienced large deformations before losing their lateral strength. After cracking, the control wall exhibited an approximately linear response up to a lateral force near 7 kips, after which the lateral strength of the specimen remained approximately constant under deflections up to 3.3 in., when concrete crushing and buckling of compression reinforcing bars occurred near the wall base and caused a near total loss of strength. Note that the boundary element had minimal confining reinforcement (Section 3.1).

The optimized wall had a smaller initial stiffness, but also responded approximately linearly until the longitudinal reinforcement yielded, which occurred at forces slightly greater than 6 kips. At approximately 0.8 in. of deflection, the optimized wall exhibited a sudden 21% reduction of strength due to failure of an inclined strut within the top third of the specimen (Figure 4.2(a)). As displacement was further increased, the forces redistributed and the optimized wall progressively regained strength, reaching approximately 98% of its maximum strength near 2.1 in. of deflection. At this point, a strut located within the middle third of the specimen failed (Figure 4.2(b)), causing

a 31% reduction in strength. This was again followed by redistribution of internal forces and a gradual increase in strength up to approximately 80% of the maximum strength. Testing was terminated after the specimen lost more than 50% of its maximum strength at 4.9 in. of deflection due to crushing and buckling of the vertical strut (boundary element).

One of the reasons for failure of struts in the optimized wall was the lack of detailing for deformation capacity; the strength was much larger than needed (Section 3.1) but the detailing could have been improved. Because the aim of these tests was to (1) demonstrate the feasibility of constructing cast-in-place structures with 3D-printed formwork and (2) provide a basis for calibrating the stiffness of linear models, the failure mode of the optimized wall was not a primary concern. Clearly, if such a structure were to be constructed in practice, superior detailing would be necessary to ensure adequate deformation capacity and control of undesirable failure modes.

(a) (b)

Figure 4.2: Failure of struts in the (a) top third of the specimen and (b) middle third of the specimen

4.2 Measured Shear Force versus Drift Ratio

Shear force is plotted versus drift ratio in Figure 4.3. Drift ratio was defined as the lateral top displacement from the previous section, corrected for base block translation and rotation, divided

by the height of the wall measured from the top of base block to the line of action of the actuator. It is clear from Figure 4.3 that both specimens exhibited drifts that were considerably larger than 2%, a common drift limit in practice, before losing their ability to resist lateral loads.

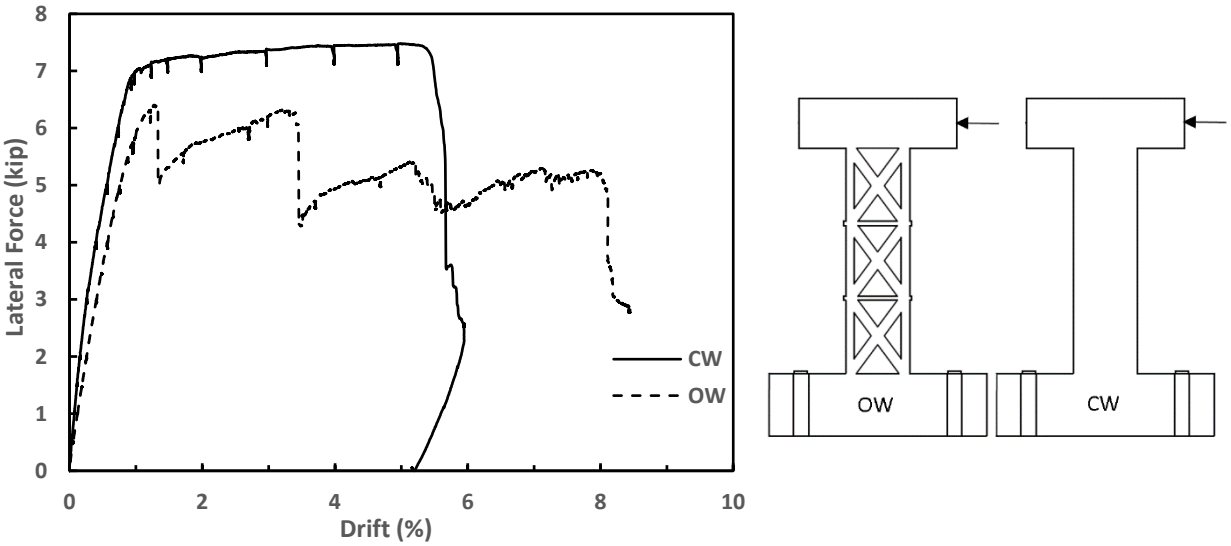

Figure 4.3: Lateral force versus drift ratio

The control wall exhibited its maximum strength of 7.5 kips at 5.0% drift whereas the optimized wall exhibited its maximum strength of 6.4 kips at 1.3% drift. The failures of the struts in the optimized wall described in Section 4.1 occurred at 1.3% and 3.4% drift. The control and optimized walls resisted lateral forces exceeding 80% of their lateral strength up to drifts of 5.6% and 8.1%, respectively.

4.3 Stiffness

The initial stiffness of the specimens was measured in two ways: (1) based on acceleration measurements made before applying lateral loads to the specimens and (2) as the initial slope of the load-displacement curves.

Accelerations were measured using an accelerometer mounted to the top block at the vertical height where horizontal force would be applied. These measurements were made without the

actuator or external bracing (shown in Figure 3.12) attached, but with the specimens bolted to the strong floor. The specimens were excited by tapping the top block with a mallet in the plane of the wall (i.e. in the same direction the actuator would bear on the specimen). The acceleration versus time data collected from both specimens showed clear evidence of a periodic response dominated by a single mode of vibration.

The frequency of vibration was identified for each specimen based on the distance between time-axis intercepts. Eq. 4.2 was used to estimate the cracked stiffness, *k*.

$$k = (2\pi f)^2 \times (M + 0.23m) \quad \text{Eq. 4.2}$$

Where: *f* is the vibration frequency for the first vibration mode in the plane of the wall obtained from accelerometer data, *M* is the mass of the top block (assumed to be equivalent to a lumped mass) and *m* is the mass of the wall (assumed to be evenly distributed throughout the wall height).

The initial stiffness of the specimens was estimated from the force-displacement data as the slope of a line passing through points corresponding to 0.2 and 1.2 kips of force (Figure 4.4). The data for calculation was restricted to 1.2 kips based on the calculated value of cracking force obtained using Eq. 4.3.

$$P_{cr} = \frac{f_r \times I_g / y_b}{h_w} \quad \text{Eq. 4.3}$$

$$I_g = \left(\frac{h l_w^3}{12}\right) + \left((n-1)A_{rf}(d_1 - y_b)^2\right) + \left((n-1)A_{rf}(d' - y_b)^2\right) \quad \text{Eq. 4.4}$$

Where: P_{cr} is the calculated cracking force, f_r is the modulus of rupture (taken as $7.5\sqrt{f'_c}$), I_g is the gross moment of inertia of the cross-section considering tension and compression reinforcement (Eq. 4.4), y_b is the location of neutral axis (equal to $l_w/2$), h_w is the total height of

wall (60 in.), n is the ratio of modulus of elasticity of steel to concrete, h is the thickness of wall (2 in.), A_{rf} is the area of longitudinal reinforcement (10 no. 2 bars), d_1 is the distance from the extreme compression fiber to the centroid of the tensile longitudinal reinforcement (14 in.), d' is the distance from the extreme compression fiber to the centroid of the compression reinforcement (1 in.), and y_b is the distance from the centroid to the compression face (7.5 in.).

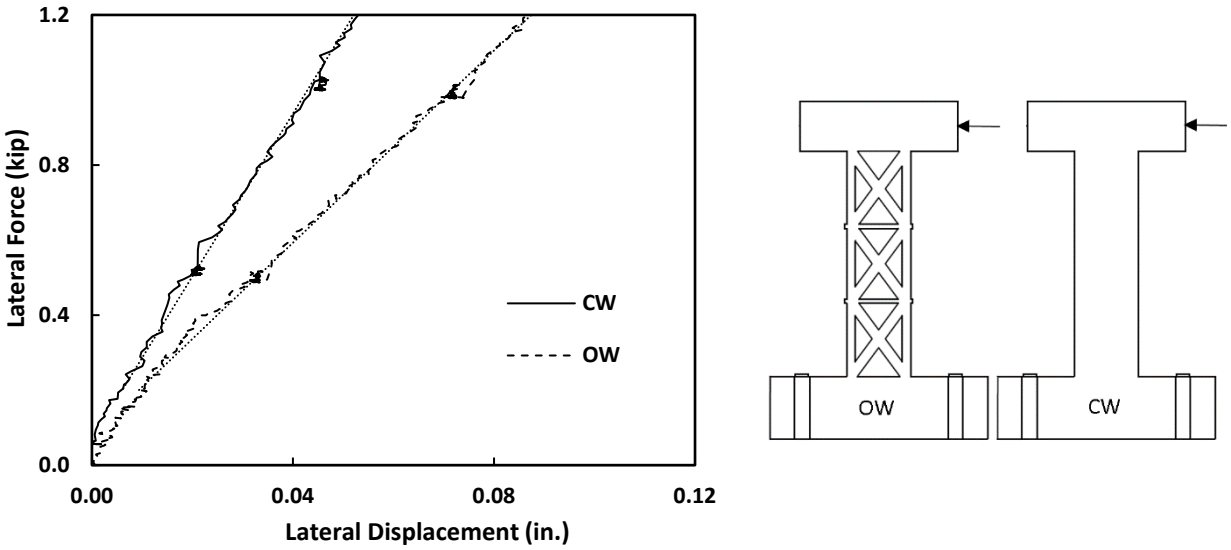

Figure 4.4: Estimated uncracked stiffness from pushover test results

The initial stiffnesses of the specimens estimated from the slope of load-displacement curves and the accelerometer data are shown in Table 4.1. The two methods of estimating stiffness differed by -6.9 and +7.0% for the control and optimized walls, respectively. The optimized wall, which had 43% less volume than the control wall, had an uncracked stiffness that was between 32 and 41% less than that of the control wall (depending on approach used to calculate stiffness).

Table 4.1: Comparison of initial stiffness from accelerometer and pushover test results

Specimen	Natural Frequency (Hz)	Stiffness [1] (kip/in.)	Stiffness [2] (kip/in.)	% Difference [3]
Control Wall (CW)	20	20.2	21.7	-6.9
Optimized Wall (OW)	16.7	13.7	12.8	+7.0

[1] Stiffness calculated using Eq. 4.2. [2] Stiffness obtained from pushover test data (Figure 4.4).
[3] Pushover test data used as the reference.

4.4 Components of Deformation

The contributions of shear and flexural deformations to overall deformation were calculated using the concept described in Huq et al. (2018) and used by several others. The deformation components were calculated based on the changes in the positions of markers glued to the surface of each specimen. The calculations are derived assuming they are applied to a set of four markers arranged in a rectangular pattern. Deformation of the rectangular shape circumscribed by markers *A*, *B*, *C*, and *D* was assumed to be comprised of deformations due to flexure (θ), shear (γ), and transverse expansion (ψ) (Figure 4.5).

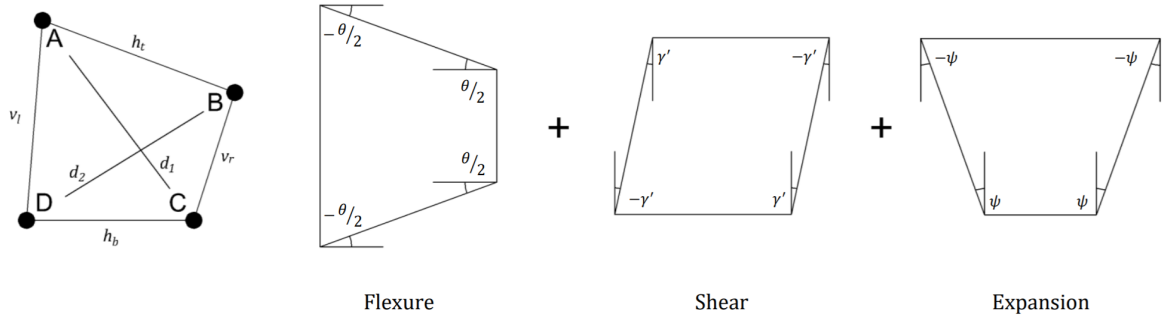

Figure 4.5: Components of deformation (Huq et al., 2018)

These deformation components were calculated with Eqs. 4.3 through 4.5 based on the change in angles at *A*, *B*, *C*, and *D*, where subscript *i* indicates the time *i* and subscript *o* indicates a time before the specimen was loaded. For any given time *i*, angles *A*, *B*, *C*, and *D* were calculated using Eqs. 4.6 through 4.9, respectively. The change in angles *A*, *B*, *C*, and *D* were taken to be equal to the sum of components θ, γ, and ψ obtained as shown in Eqs. 4.10 through 4.13.

$$\theta_i = -\frac{1}{2}[-(A_i - A_o) + (B_i - B_o) + (C_i - C_o) - (D_i - D_o)] \quad \text{Eq. 4.3}$$

$$\gamma_i = -\frac{1}{4}[(A_i - A_o) - (B_i - B_o) + (C_i - C_o) - (D_i - D_o)] \quad \text{Eq. 4.4}$$

$$\psi_i = \frac{1}{4}[-(A_i - A_o) - (B_i - B_o) + (C_i - C_o) + (D_i - D_o)] \quad \text{Eq. 4.5}$$

$$A_i = cos^{-1}\left(\frac{{h_t}^2+{v_l}^2-{d_2}^2}{2h_t v_l}\right)$$ Eq. 4.6

$$B_i = cos^{-1}\left(\frac{{h_t}^2+{v_r}^2-{d_1}^2}{2h_t v_r}\right)$$ Eq. 4.7

$$C_i = cos^{-1}\left(\frac{{h_b}^2+{v_r}^2-{d_2}^2}{2h_b v_r}\right)$$ Eq. 4.8

$$D_i = cos^{-1}\left(\frac{{h_b}^2+{v_l}^2-{d_1}^2}{2h_b v_l}\right)$$ Eq. 4.9

$$A_i - A_o = -{\theta}/{2} + \gamma - \varphi$$ Eq. 4.10

$$B_i - B_o = {\theta}/{2} - \gamma - \varphi$$ Eq. 4.11

$$C_i - C_o = {\theta}/{2} + \gamma + \varphi$$ Eq. 4.12

$$D_i - D_o = -{\theta}/{2} - \gamma + \varphi$$ Eq. 4.13

Since the method assumes uniform curvature within the rectangular cell circumscribed by *A*, *B*, *C*, and *D*, the values of deformation reported in subsequent sections are approximate. This is especially true when the rectangular cell circumscribed by *A*, *B*, *C*, and *D* was selected to cover large portions of the structure, which was sometimes necessary because the optimized wall had few rectangular cells available. The main purpose of the following discussion is to compare the global behavior of the two specimens. More detailed results for the control specimen based on a smaller grid (l_w/5), where uniform curvature within a cell is a more reasonable assumption, are reported in Appendix A. Calculations were also made for different cell sizes based on the control-wall data, and comparisons are reported in Appendix A that help demonstrate the sensitivity of

this approach to cell size. These results may inform interpretations of the results presented for the optimized wall.

4.4.1 Flexural Rotation

Flexural rotations were calculated for both specimens using Eq. 4.3 and cells of markers that approximately covered the bottom, middle, and upper thirds of the specimens. Flexural rotation at each level was multiplied by the vertical distance between the mid-height of level and the point of application of lateral force. The sum of this product at the bottom, middle, and upper third levels of the specimens was divided by the total height of the wall (60 in.) to obtain the drift resulting from flexural rotation. The lateral force was plotted against this final drift from flexural rotation in Figure 4.6. Figure 4.6 does not include concentrated rotations at the base of the wall due to strain penetration and slip of the wall reinforcement in the foundation.

The control wall results in Figure 4.6 are similar to the lateral force versus drift plot, suggesting that flexure governed its global behavior. Up to approximately 6 kips of lateral force, the same can be said for the optimized wall. However, after failure of inclined struts, drifts due to flexural rotation of the optimized wall specimen were much smaller than the overall drift, especially after the second strut failed. At an overall drift of 0.04 rad, flexural rotations accounted for 0.011 and 0.003 rad (28 and 8%) in the control wall and optimized wall, respectively.

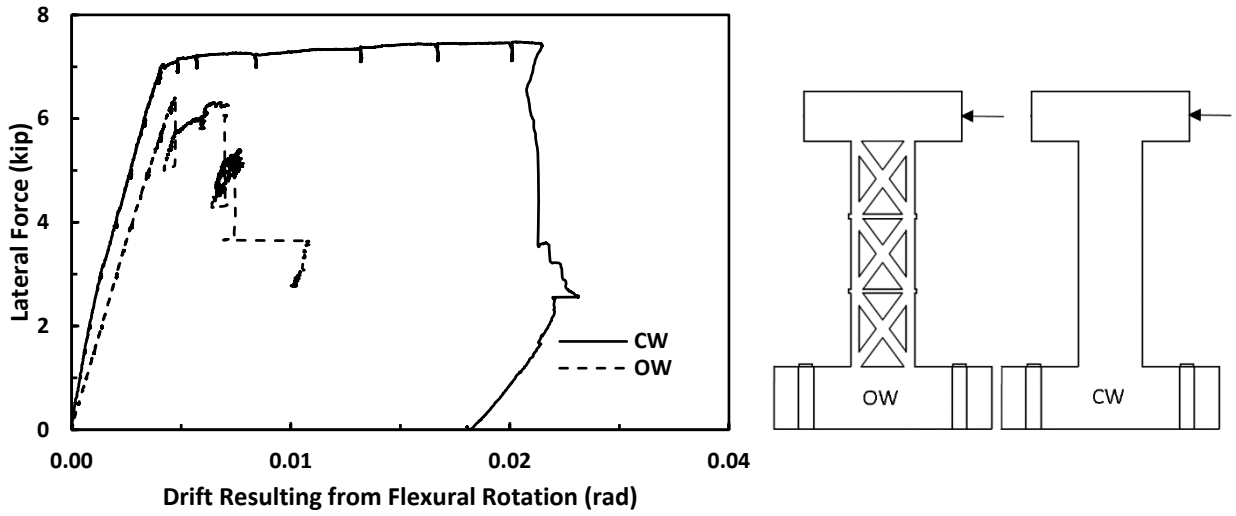

Figure 4.6: Lateral force versus flexural rotation

The flexural rotation within each level distribution is plotted for several imposed drift ratios in Figure 4.7. Flexural rotations in both walls were largest in the lowest level (bottom one-third of the height), although they were much larger near the base of the control wall than elsewhere.

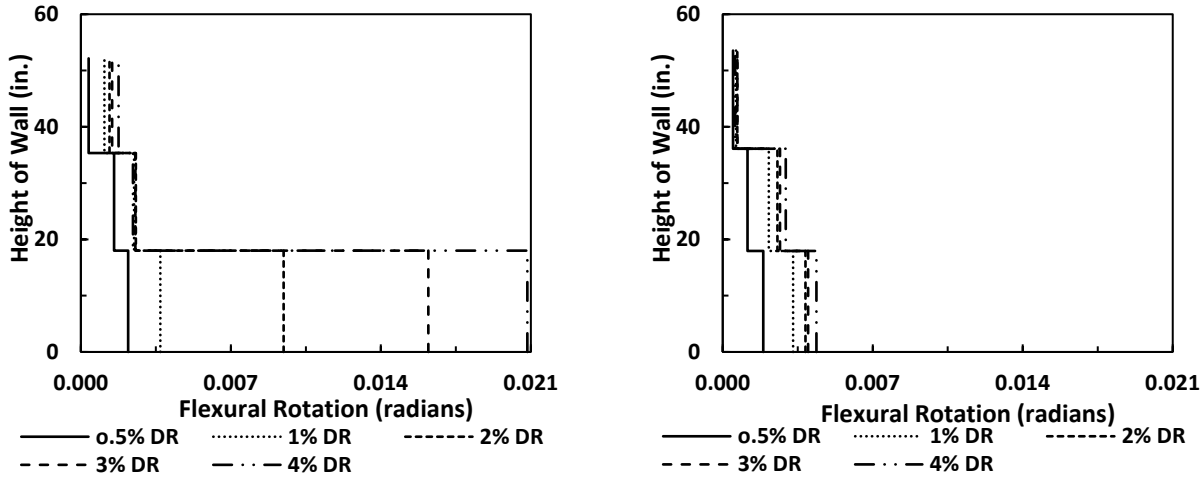

Figure 4.7: Flexural rotations along the height of (a) control and (b) optimized walls

The large flexural rotations within the lowest level of the control wall are consistent with the observed damage, which ultimately concentrated at the base of the wall. Concrete crushing and buckling of longitudinal bars in compression zone at failure was observed during the test. Damage

of this type was not observed near the base of the optimized wall, which underwent markedly less flexural rotation.

Figure 4.8: Control wall damage at failure

4.4.2 Shear Deformation

Shear deformations of the specimens were calculated using Eq. 4.4 at three levels that approximately corresponded to the bottom, middle, and upper thirds of the specimens. The computed shear deformation at each level was then multiplied by the height of the level and summed to obtain a total deformation resulting from shear. This was divided by the total height of the specimen to obtain the drift resulting from shear deformations.

The total drift from shear deformations is plotted for both specimens in Figure 4.9. For the control wall, drift from shear deformations was much smaller than the total imposed drift. The opposite was true for the optimized wall, for which drift from shear deformations was very similar to the total imposed drift. It is clear that shear dominated the global behavior of the optimized wall, especially after failure of the struts. At an imposed drift of 0.04 rad, the drifts resulting from shear deformations in the control and optimized walls were 0.007 and 0.032 (18 and 80%), respectively.

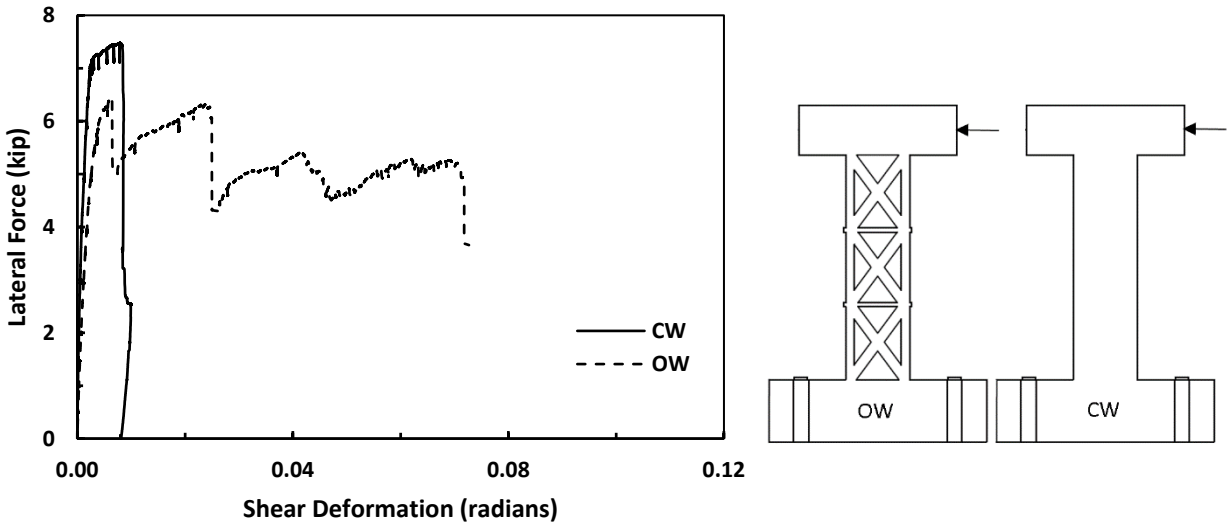

Figure 4.9: Wall drift attributed to shear deformations in the control and optimized walls

This is consistent with the damage observed during the test of the optimized wall (Figure 4.10). Most of the damage was concentrated in the upper two levels, where inclined struts failed due to buckling of reinforcement and crushing/splitting of concrete. Failure of the inclined struts led to large shear distortions, resulting in failures of the vertical struts that were forced to deform in a manner compatible with the inclined members. These observations were made at large deformations – deformations that are larger than would be expected in most structures, especially those designed for non-seismic demands.

Figure 4.10: Damage observed in optimized wall at failure

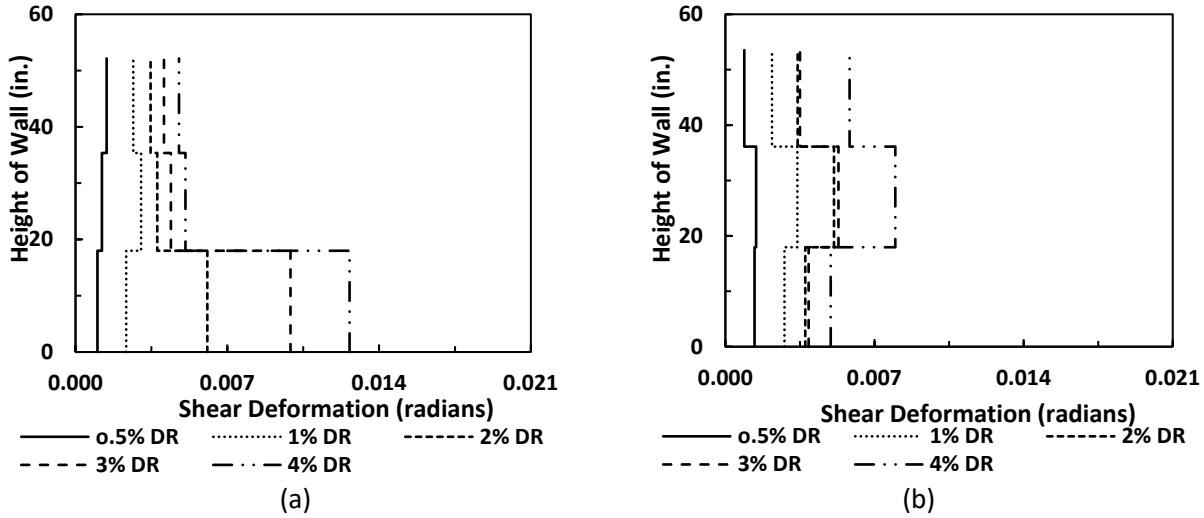

Figure 4.11: Shear deformation along the height of the (a) control wall and (b) optimized wall

Figure 4.11 shows the shear deformations calculated for each of the three levels considered in each specimen. The control wall exhibited nearly uniform shear distortion along its height up to approximately a 1% drift ratio, after which shear deformations were largest in the bottom third of the wall. This was expected, as wall shear stiffness is known to decrease in areas subjected to flexural rotation demands that cause flexural reinforcement to yield. In the optimized wall, the shear deformation in the middle third level was larger than at other levels. At 1% drift, the middle

level experienced a shear deformation of 0.0034 rad while the bottom and top levels experienced shear deformations of 0.0028 and 0.0022 rad. The differences between shear deformations within each level became more pronounced as drift demands increased.

4.4.3 Axial Deformation

Figure 4.12 shows the distribution of axial strains along the height of the walls for each column of markers. Axial strain refers to the change in distance between successive markers divided by their initial distance. Since the control wall had five columns of markers near its base, Figure 4.12(a) has five sets of data, whereas only two are shown for the optimized wall (Figure 4.12(b)). The dimensions used as figure labels refer to the distance between the extreme compression fiber and the column of markers used for the calculation. Axial deformations are shown for a drift ratio of 1% in Figure 4.12. Appendix A has similar plots for drift ratios of 0.25%, 0.5%, 1%, 2%, 3%, and 4%.

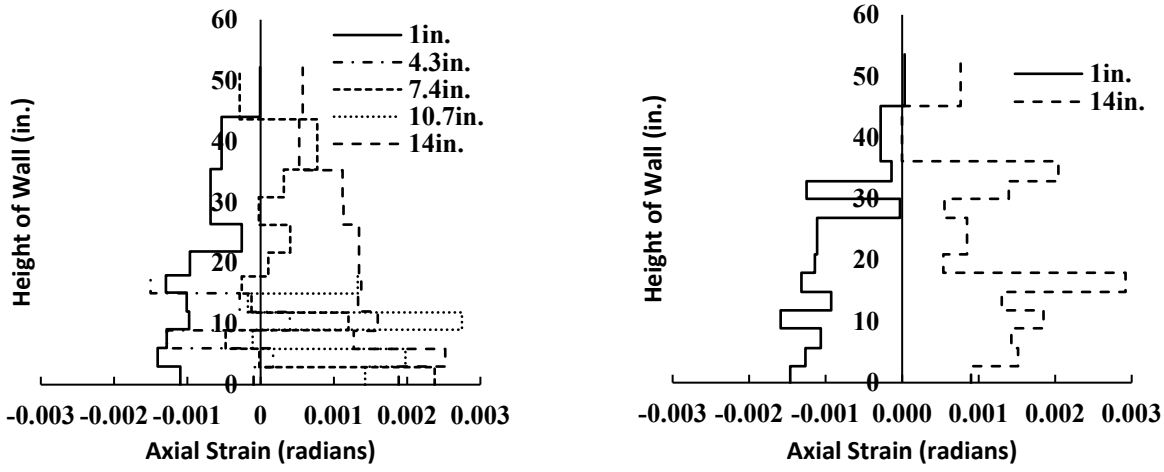

Figure 4.12: Axial strains along height of the wall at 1% drift ratio in (a) control and (b) optimized walls

4.4.4 Damage

Principal strain contours were obtained from the digital image correlation (DIC) system output. Figure 4.13 shows the strain contours at 1.5% drift. Similar figures are provided in Appendix A for several different deformation demands. Cracks were observed to have developed starting at the tension face of the control wall and propagated through the web at an inclination, as expected. Cracks were observed in the vertical and inclined ties in the optimized wall, also as expected. Figure 4.13(b) also shows that deformations were largest near the joint between the inclined tie and the vertical strut (upper right of figure), where local member rotation demands appear to have been large. This damage and the mode of failure suggest that truss members and nodes require detailing to ensure adequate deformation capacity of individual members.

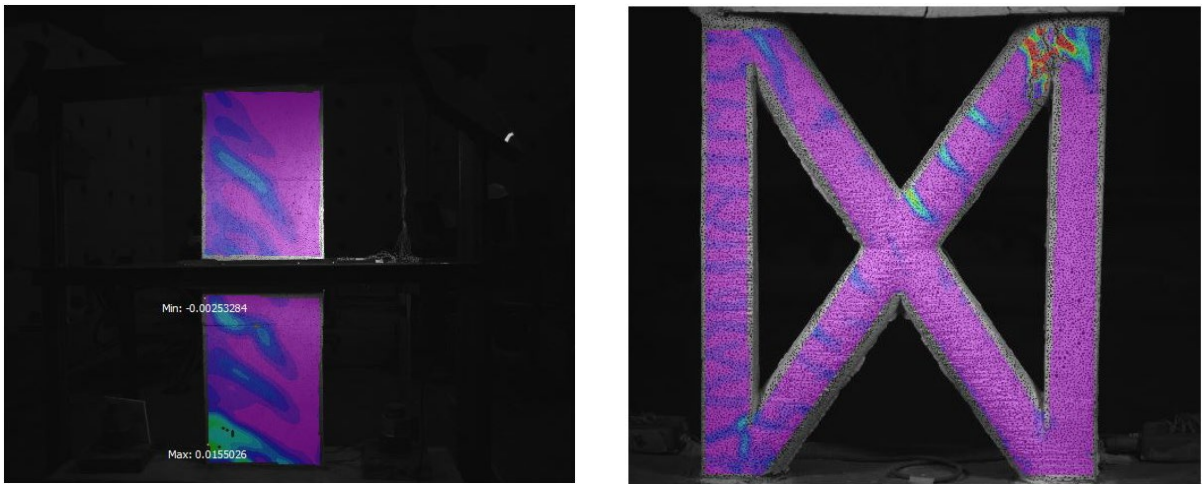

(a) (b)

Figure 4.13: Damage at 1.5% drift in the (a) control wall and (b) optimized wall (lateral load is being applied towards the right in both figures)

CHAPTER 5 - TOPOLOGY OPTIMIZATION USING ABAQUS (TOSCA)

The aim of this chapter is to describe an approach for using topology optimization in design of RC structures, including modeling optimized member behavior and designing for stiffness. ABAQUS was used because it is a commonly used commercially available finite element analysis software. The control wall described in Chapters 3 and 4 was modeled and FE analysis outputs were compared to the experimental results to validate material properties. Topology optimization was then done, resulting in a variety of different profiles at different volume ratios. Each profile was then re-analyzed to quantify stiffness and study overall behavior of the optimized structures.

5.1 Rectangular Wall Analysis

Two different models were created to simulate the rectangular control wall described in Chapters 3 and 4. One model had discretely modeled longitudinal reinforcement while the other was modeled using a material with a stiffness selected to represent the stiffness of an uncracked reinforced concrete element. The first model with discrete reinforcement was created to simulate experimental conditions and validate modeling assumptions. The approach used for this model, once validated, formed the basis for the analysis of optimized models discussed in Section 5.4. The second model was created to accommodate the limitations of the topology optimization algorithm, which could not accommodate discretely-modelled reinforcement and only supported linear elastic, plastic, and hyperplastic material models (ABAQUS Analysis User's Manual, 2007). Neither model considered geometric nonlinearity (buckling).

5.1.1 Material Properties

Concrete and steel materials used in the first model were assigned the properties listed in Table 5.1. Concrete was modeled using the concrete damaged plasticity model in ABAQUS. This

material model assumes that concrete failure occurs due to crushing or tensile cracking (Hillerborg, Modéer, and Petersson, 1976; Lubliner, et al., 1989; Lee, and Fenves, 1998). The material model was explained in Wahalathantri et al. (2011). The values of dilation angle (φ), flow potential eccentricity (e), ratio of initial equi-biaxial compressive yield stress to initial uniaxial compressive yield stress (σ_{b0} / σ_{c0}), ratio of second stress invariant on tensile meridian (K_c), and the viscosity parameter (μ) were taken from (Tao et al., 2013). A concrete compressive strength of 6000 psi was assumed, resulting in an elastic modulus of 4,400 ksi based on ACI 318-14 equations and a tensile strength of 300 psi. The tensile strength was calculated from the $3.75\sqrt{f'_c}$ recommended by Orakcal et al. (2004). Steel reinforcement was modeled as an elastic-perfectly plastic material. Perfect bond was imposed between the steel reinforcement and concrete.

Table 5.1: Material properties for model with discrete reinforcement

	Concrete	**Steel**
Density (lb/ft^3)	145	490
Poisson's Ratio	0.2	0.3
Modulus of Elasticity (ksi)	4,400	29,000
Compressive strength (psi)	6000	
Yield Stress (psi)		36,000
Tensile strength (psi)	300	
Dilation Angle (deg)	31	
Flow Potential	0.1	
σ_{b0} / σ_{c0}	1.16	
K_c	0.75	
Viscosity Parameter, μ	0	

The material properties used in the second model are listed in Table 5.2. To create this model, which did not have discrete reinforcement, the wall was divided into three parts: two 2 by 2 by 60 in. boundary elements at each wall edge and an 11 by 2 by 60 in. web. The boundary elements were modeled with an elastic-perfectly plastic material while the web was modeled as linear-elastic; both regions were assigned a homogeneous material defined in a manner intended to represent reinforced concrete. The modulus of elasticity was calculated with Eq. 5.1, which is based on the rule of mixtures and neglects effects of cracking. Density was defined in a similar manner. The tensile strength in the boundary element was limited to the value shown in Eq. 5.2. The strength in compression was assumed to be equal to concrete compressive strength (f'_c). For the boundary elements, the reinforcement ratio, ρ, was 0.125 (based on 10 No. 2 bars placed in a 2 by 2 in. rectangular cross-section). The web reinforcement ratio was taken as zero because it was so small it had a negligible effect on outcomes.

$$E_{effective} = [(1-\rho)E_c] + [\rho E_s] \quad \text{Eq. 5.1}$$

$$f_{limit} = \rho f_y \quad \text{Eq. 5.2}$$

Table 5.2: Material properties for model with non-discrete reinforcement

	Boundary Element	**Web Region**
Density (lb/ft^3)	190	145
Poisson's Ratio	0.2	0.2
Modulus of Elasticity (psi)	7500000	4400000
Compressive Strength (psi)	6000	
Tensile Strength (psi)	6000	

5.1.2 Boundary Conditions

For the two models described in the previous section, fixed-end supports were defined using displacement/rotation boundary conditions prior to loading (during the static step). All six degrees of freedom for each node at the base were set to zero. A feature of the algorithm, called Nlgeom, was enabled to allow for geometric nonlinearity during loading steps.

5.1.3 Loading Protocol

A lateral force was applied to the wall models as a 200 psi surface traction on the 2 by 15 in. cross-section at the top of the wall, resulting in a 6 kip lateral force. Since the applied surface traction resulted in a force-controlled analysis, it was important to limit the lateral force to a point before yielding, which was expected to occur between 6 and 7 kips.

5.1.4 Model Validation

The load-displacement results from the model with discrete reinforcement are shown in Figure 5.1 along with the experimental result up to 5.7 kips. A change in slope of the load-displacement curve was observed after this load, perhaps due to yielding, so only the data up to 5.7 kip of lateral force was used for this study. The cracking load in the FE model obtained from the change in slope of the load-displacement curve was approximately 1.4 kip. This was estimated as the force corresponding to the intersection point of two linear trend-lines fit to the curve before and after the change in slope (cracking). This cracking force was close to the cracking force estimated in Section 4.3 (1.2 kip).

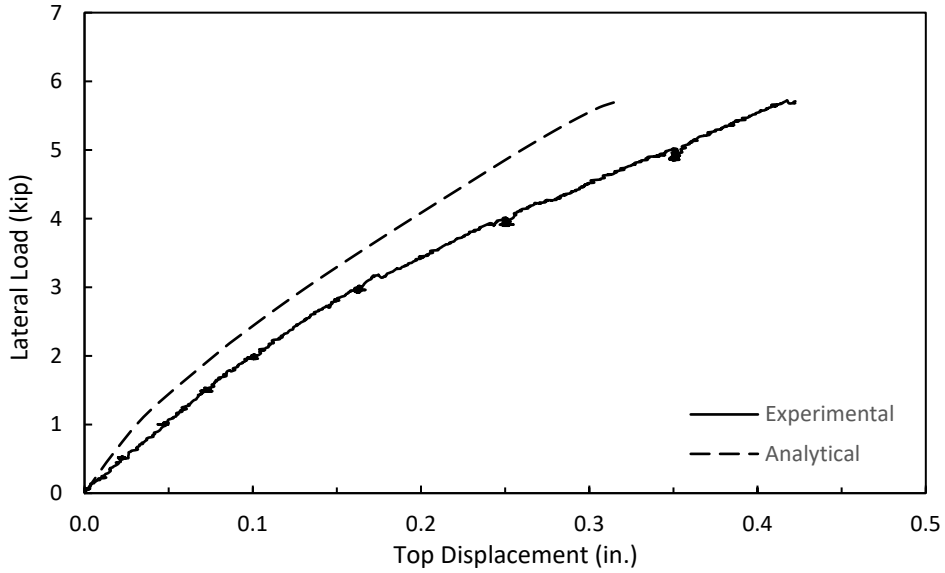

Figure 5.1: Load versus Displacement: Experimental Result and FE Output for Model with Discrete Reinforcement

Figure 5.1 shows that the analytical model was stiffer than the test specimen. A reason for this difference was the fact that the analytical model was rigidly fixed at the base while the test specimen exhibited a concentrated rotation at its base due to straining and slip of the longitudinal wall reinforcement within the base. To estimate the extent to which this accounts for the difference between the results, the displacement attributable to strain penetration was estimated using Eq. 5.5, where the base rotation, θ_{base}, was calculated as the total elongation of the wall reinforcement within the base block calculated using Eq. 5.6 divided by *jd,* the assumed distance between tension and compression force resultants (13 in.). Equation 5.6 assumes a triangular distribution of reinforcement strain over the calculated development length, l_d, calculated using Eq. 3.3. The maximum strain, ε, is an estimate of the axial tensile strain in the reinforcement at a lateral force of 6 kips calculated using Eq. 5.7, where *P* is the lateral force (6 kips), and *jd* is the assumed distance between tension and compression regions (13 in.).

$$\Delta_{correction} = \theta_{base} \times h_w \quad \text{Eq. 5.5}$$

$$\Delta_{base} = 1/2 \times \varepsilon \times l_d \quad \text{Eq. 5.6}$$

$$\varepsilon = \frac{P \times h_w}{jd \times A_{rf} \times E}$$ Eq. 5.7

Table 5.3 shows the deflection at 5.7 kips measured in the test, determined from the FE model, and the deflection from the FE model corrected for base rotation in the manner described previously. It is evident that most of the difference between the FE model and the test specimen is attributable to the different boundary condition at the base. The remaining difference is likely due to other approximations made when developing the model, particularly the assumption of perfect bond between the steel reinforcement and concrete. Nevertheless, the corrected result was believed to provide a sufficiently satisfactory approximation of the experimental result for the modeling approach described above to be used again for simulating the behavior of optimized models (in Section 5.4).

Table 5.3: Deflection at 5.7 kips lateral force

	Experimental Results	**FE Model without Correction**	**FE Model with Correction**
Top Displacement (in.)	0.42	0.32	0.40
% Difference	-	24	5

The second FE model (without discrete reinforcement) had linear elastic material properties and ignored concrete cracking, resulting in a dramatically stiffer response. The deflection of this model at 6 kips was only 0.13 in. This model is clearly inadequate for estimating load-deflection behavior of conventional or optimized RC members. It will only be used herein as the basis for topology optimization.

5.2 Topology Optimization Approach

The aims of the topology optimization part of this study were to (1) document the sensitivity of optimized geometries to modeling parameters and (2) examine the relationship between volume ratio (defined as the ratio of optimized to original volumes in percent) and wall stiffness, an important parameter in design.

Tosca, a topology optimization software, was used in combination with ABAQUS. The user has two options for algorithms: (1) general topology optimization, which employs the SIMP approach described in Chapter 2, and (2) condition-based topology optimization, which employs the ESO approach described in Chapter 2. For this study, the condition-based topology optimization approach was selected to avoid construction or post-processing difficulties associated with elements having varied densities that result from using SIMP algorithms.

5.2.1 Optimization Scope, Objective Function, and Constraints

The scope of the optimization task was limited to the 11 by 2 by 60 in. web region, excluding the top edge/surface on which the lateral force of 6 kip was applied as a surface traction (which was excluded because changes in that surface area would result in changes in force demand because of the manner in which the load was applied). The 2 by 2 by 60 in. boundary elements at each edge of the wall were also excluded from the optimization task because these needed to be reinforced and optimization of these volumes would have made reinforcement detailing difficult.

The objective function was to minimize the total strain energy for all the structure (i.e. minimize the sum of strain energy of all elements). The constraint applied to the task was the ratio of final volume to original volume (volume ratio), which was a variable in this study. Thus, each model "run" would aim to find the geometry that exhibits the smallest total strain energy while also

satisfying the volume ratio constraint. This is done by iteratively removing elements subjected to small stress demands until the specified volume ratio is obtained.

An additional geometric restriction was imposed in some models described later in the chapter: symmetry about the centroid of the wall cross-section. This was done so the wall could resist the same lateral force in both loading directions, a common case in design.

In addition to the constraint (volume ratio), several parameters were found to affect optimization results, including element type, mesh size, and number of cycles (or iterations). The following describes the effects of these variables on topology optimization outputs.

5.2.2 Number of Optimization Cycles

Figure 5.2(a) shows the results from several optimization analyses done using different numbers of optimization cycles on models with different mesh sizes subjected to a lateral force of 6 kips; the figure shows total internal strain energy in the optimized member versus number of optimization cycles. A volume ratio constraint of 70% was used for all analyses shown in this figure. Because the applied force was constant in this parametric study, and because internal strain energy equals external work, strain energy in Figure 5.2(a) is proportional to displacement at the top of the wall and inversely proportional to stiffness. The lower bound limit on the number of cycles for condition-based topology optimization in Tosca is 10. So, optimizations were done on models with varied mesh sizes using 10 to 75 cycles. The mesh sizes selected for this study were 1 in. (half the wall thickness), 0.5 in., 0.4 in., and 0.25 in.

Figure 5.2(a) shows that, for a given mesh size, the strain energy decreased quickly as the number of optimization cycles increased from 10 to approximately 25, after which increased number of cycles resulted in little or no change in strain energy regardless of mesh size. This small parametric

study therefore appears to show that once the number of cycles required to reach convergence is identified for a given structure, objective function, and constraint, that same number of cycles can be used for other mesh sizes without additional sensitivity studies.

Figure 5.2(a) also shows that the strain energy in the optimized wall decreased as mesh size decreased from 1 in. to 0.25 in. (0.5h to 0.125h). Furthermore, the output did not appear to converge as mesh size decreased. Perhaps further reductions are needed to reach convergence.

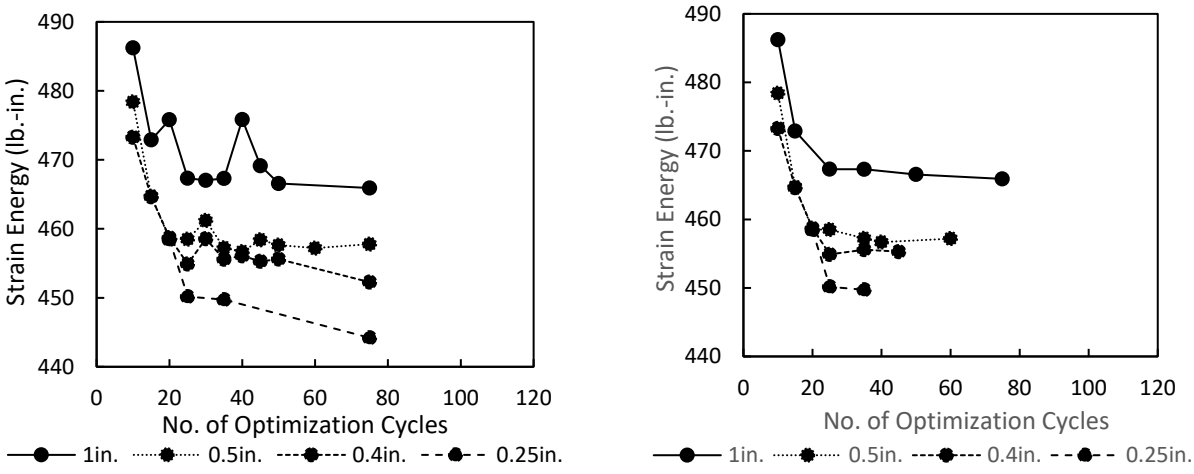

Figure 5.2: Strain energy versus number of optimization cycles for a volume ratio of 70% (a) without smoothing (b) with smoothing (element type C3D8H)

Although the curves in Figure 5.2(a) show the general trend described previously, each also exhibits spikes, or sharp increases in strain energy, at some intermediate cycles that appear inconsistent with the trends. This was observed in all mesh sizes. These sudden jumps were clearly visible in plots of strain energy versus number of cycles (Figure 5.3). In Figure 5.3, each curve represents a topology optimization analysis for a given mesh size and number of optimization cycles. These iteration cycles resulted in different final optimized shapes. One possible cause of the spikes is the ESO-style condition-based topology algorithm used for the analyses: abrupt changes in the topology between steps arise due to the fixed 0-1 integer values used to signal

whether an element is a void or a solid. This is a known issue that was addressed in Huang and Xie (2007), Huang and Xie (2010), and Mahmoud et al. (2018), where a stabilization index was defined to correct it.

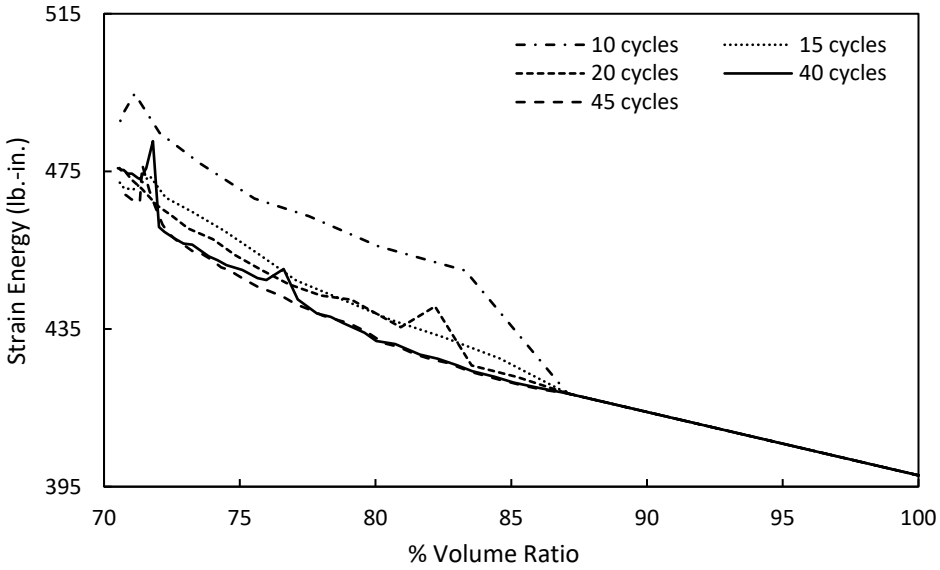

Figure 5.3: Strain energy versus volume ratio, where each point represents the strain energy at a given iteration step in the analysis process (element type C3D8H, 1 in. mesh size)

Since the topology optimization algorithm used in this study was commercially available and therefore not able to be modified by the researchers, the stability index could not be applied. Instead, cycles with spikes for each mesh size were removed, resulting in a smoothed curve relating strain energy and number of optimization cycles (Figure 5.2(b)). If an ESO-style algorithm is used for topology optimization and this stability index is not integrated into the algorithm, it will be necessary for users to conduct multiple optimizations using different numbers of cycles to identify cases where these spikes occur.

Even when the number of cycles exceeds that required for convergence (25 in this case), different optimized profiles can be obtained for different numbers of optimization cycles that exhibited similar strain energy. Two different profiles corresponding to the same strain energy (470 lb-in.)

are shown in Figure 5.4, one of which is symmetric about its centroid and one that is not. The models had a 1 in. mesh size but different numbers of iteration cycles (25 and 35 cycles). Although the profiles are different, when modeled using smeared (non-discrete) reinforcement as described in Section 5.1.1, the distributions of strain are similar under a lateral force of 1.5 kips (Figure 5.4) and the maximum tensile and compressive stresses differed by less than 3%. The difference in geometric configuration therefore appears to have no significant effect on the behavior of the optimized walls under small lateral forces in this case.

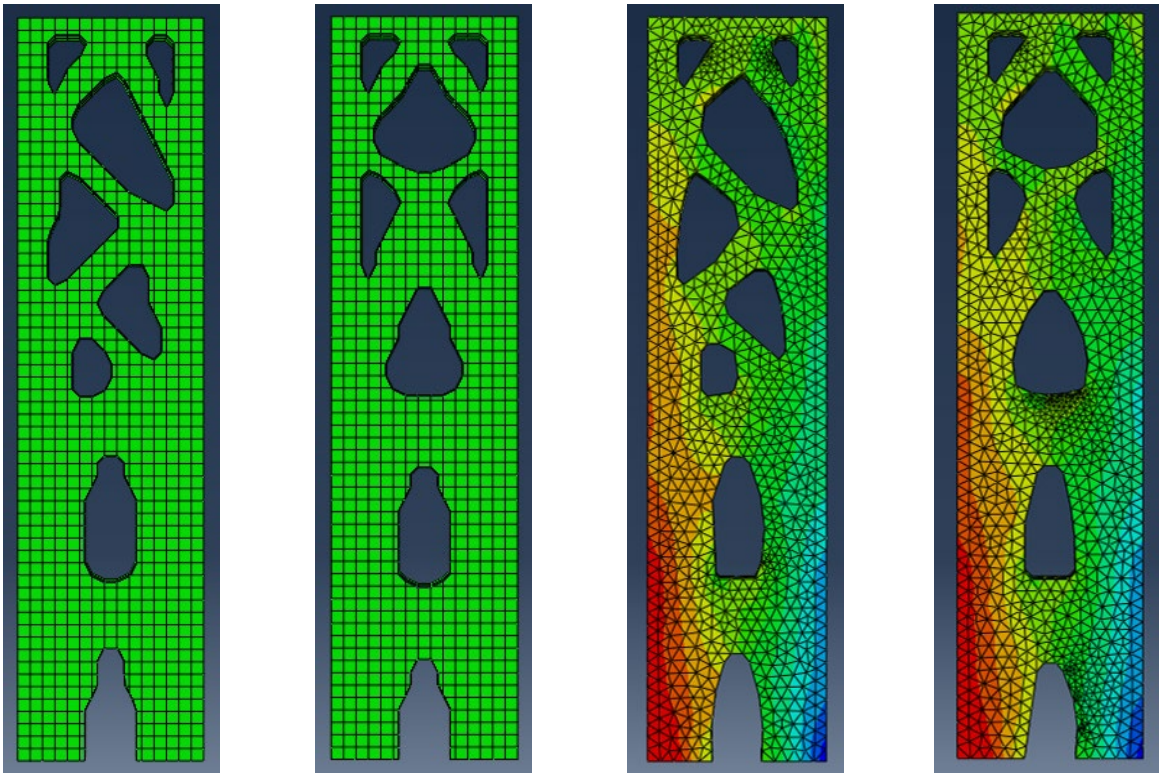

Figure 5.4: Optimized shape obtained (element type C3D8H, 1 in. mesh size) with (a) 25 optimization cycles and (b) 35 optimization cycles; axial stresses (S22) under 1.5 kips of force in the optimized designs obtained with (c) 25 optimization cycles and (d) 35 optimization cycles

It was shown previously that, regardless of mesh size, the number of optimization cycles required to reach convergence was about constant as mesh size varied for a target volume ratio of 70%. However, the number of cycles required to reach convergence changes as the target volume ratio changes, as shown in Figure 5.5, a plot of strain energy versus number of optimization cycles for

target volume ratios of 0.5, 0.6, 0.7, 0.8, and 0.9. The values reported in Figure 5.5 correspond to actual volume ratios and optimization cycle numbers, which sometimes slightly differ from the target values.

In general, Figure 5.5 shows that strain energy was larger for smaller volume ratios and the number of optimizations cycles required to reach convergence increased for smaller volume ratios. The solution for smaller volume ratios was also more likely to exhibit the spikes shown previously in Figure 5.2(a), which makes sense: a structure with a smaller volume should be more sensitive to the incremental removal of elements.

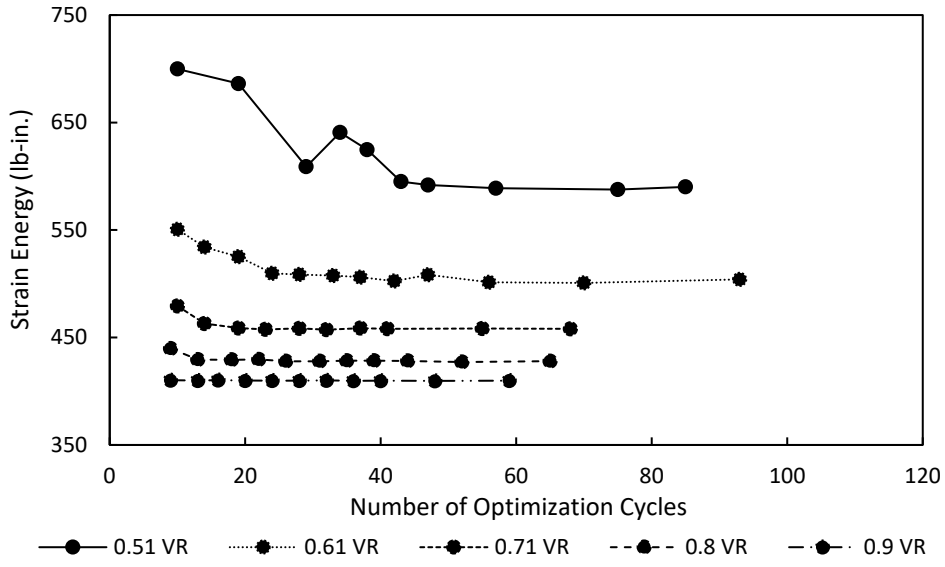

Figure 5.5: Strain energy versus number of optimization cycles (element type C3D8H, 0.5 in. mesh size)

Table 5.4 shows the lowest strain energy, optimization cycle number corresponding to that lowest strain energy, top displacement, and stiffness for different target volume ratios. Top displacement and stiffness were estimated using the finite element analysis approach with non-discrete reinforcement described in Section 5.1.

Table 5.4 shows that at each volume ratio, the lowest strain energy was obtained at different optimization cycles, with no clear trend between volume ratio and number of optimization cycles. As expected, strain energy was inversely proportional to volume ratio, causing stiffness to be correlated with volume ratio.

Table 5.4: Optimization cycles, normalized strain energy, and normalized stiffness associated with minimum strain energy for different volume ratios (element type C3D8H, 0.5 mesh size, 6 kips applied force)

Target Volume Ratio	Strain Energy (lb.-in.)	Optimization Cycle	Normalized Strain Energy	Top Disp. [1] (in.)	Stiff. [2] (kip/in.)	Normalized Stiffness
0.5	588	75	1.47	0.20	30.4	0.67
0.6	501	70	1.25	0.17	35.7	0.79
0.7	457	32	1.14	0.15	39.1	0.87
0.8	427	52	1.07	0.14	42.0	0.93
0.9	410	48	1.03	0.14	43.9	0.97
1.0	400	-	1.00	0.13	45.0	1.00

[1] The top displacement value corresponding to lateral force of 6 kip reported. [2] Stiffness calculated as lateral force (6 kip) divided by top displacement.

5.2.3 Mesh Size and Element Type

To evaluate the effects of mesh type on optimization results, four models that were similar except for element type were created and subjected to topology optimization using 35 and 75 optimization cycles. The models each had a 1 in. mesh and a target volume ratio of 0.7. The four element types were C3D4, C3D6, C3D8H and C3D10. The relatively coarse 1 in. mesh size was selected to reduce the processing time.

Table 5.5 lists the strain energy obtained after optimization was completed for each of the models. When 35 optimization cycles were used, the total strain energy differed based on the element type; models with 8- and 10-node elements had already converged at 467 lb-in of energy after 35 cycles

whereas the models with 4- and 6-node elements had not (although they were close). After 75 optimization cycles, all four models had converged to approximately 467 lb-in of strain energy.

Table 5.5: Total strain energy for different mesh types (1 in. mesh size)

Mesh Types	**Strain Energy (lb-in.)**	
	35 Cycles	**75 Cycles**
C3D4	474	466
C3D6	474	466
C3D8H	467	467
C3D10	467	467

Figure 5.6 shows that the optimized geometries differed based on element type despite all models exhibiting similar strain energy levels. As identified earlier (in the discussion of Figure 5.2), mesh size has an important effect on the obtained strain energy for the optimized system. This is also true for the final optimized geometry. Figure 5.7 shows that coarser (1 in.) meshes result in bulkier individual members while finer meshes result in progressively smaller, more streamlined members and more numerous voids (Huang and Xie, 2007; Johnsen, 2013). These figures are based on a model with element type C3D8H and a target volume ratio of 70%. It is not clear whether further decreases in mesh size would eventually reach convergence – neither Figure 5.2 nor 5.5 imply that an asymptote is being reached.

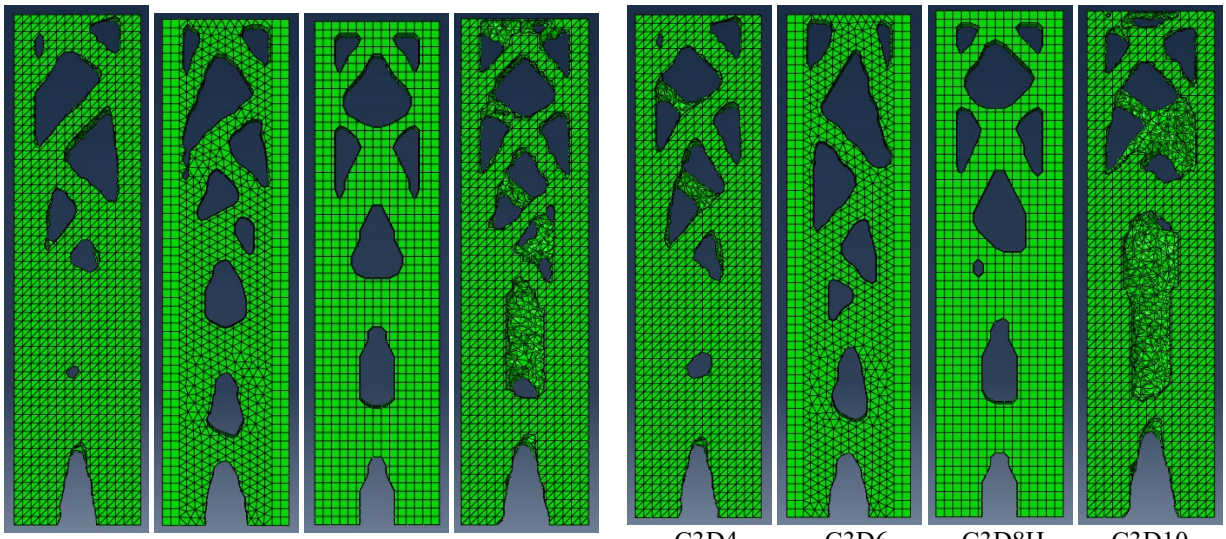

Figure 5.6: Final optimized design at (a) 35 cycles and (b) 75 cycles

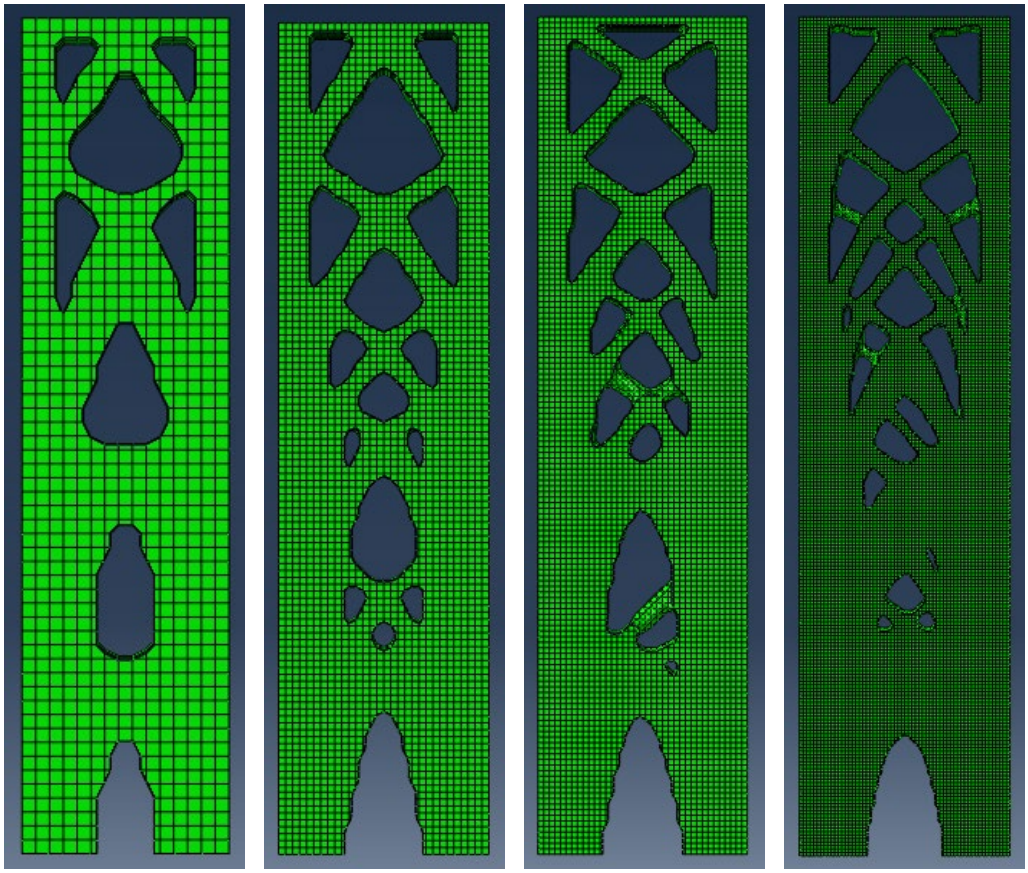

Figure 5.7: Optimized geometries for different mesh sizes (element type C3D8H and volume ratio of 70%)

Reduction in mesh size also increases computational time (Figure 5.8). These results are for models with element type C3D8H, a volume ratio of 70%, and a mesh size of either 1, 0.5, 0.4, 0.25, or 0.125 in. The number of optimization cycles was varied from 10 to 75 cycles at an interval of 5 cycles. The models with a 0.25 in. mesh took substantially longer than others.

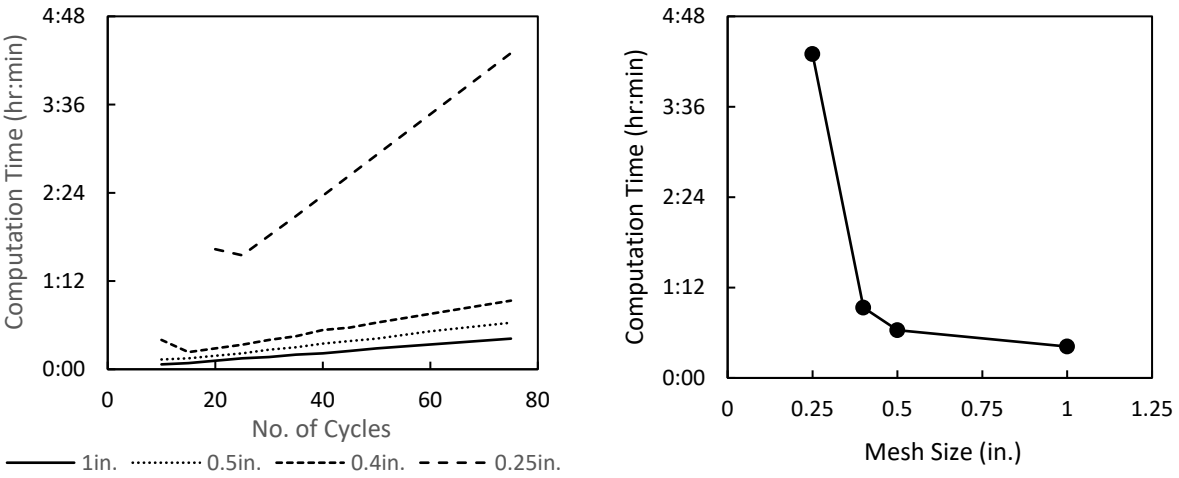

Figure 5.8: Computation time for different mesh sizes (element type C3D8H and volume ratio of 70%) at (a) different number of cycles and (b) 75 cycles

When the mesh size was reduced from 1 to 0.5 in., 0.5 to 0.25 in., and 0.25 to 0.125 in.; the reduction in strain energy (as a percent of the strain energy for the model with a 1 in. mesh) was 2%, 1.6%, and 1.4% respectively (Table 5.6).

Table 5.6: Total strain energy for different mesh sizes (element type C3D8H and volume ratio of 70%)

Mesh Size (in.)	**Strain Energy (lb-in.)**	**% Change in Mesh Size Relative to 1 in.**	**% Change in Strain Energy Relative to 1 in.**
1	466.6	-	-
0.5	457.2	50	2
0.4	455.3	60	2.4
0.25	449.7	75	3.6
0.125	443.4	87.5	5

The trend suggests gradual convergence of strain energy at finer mesh sizes, although the 0.125 in. mesh may not have reached convergence. Nevertheless, the changes in strain energy are small: a change from a 1 in. mesh to a 0.125 in. mesh resulted in only a 5% reduction in strain energy but required 17 times longer to run. It therefore appears the largest difference in result obtained from differences in mesh size are related to computation time and the aesthetics of the geometry of the optimized shape.

5.3 Analysis of Topology Optimized Structures

5.3.1 Topology Optimized Geometry and Wall Stiffness

Based on the above parametric study, further analyses were done using element type C3D8H with a mesh size of 0.5 in. and target number of optimization cycles of 60 (with an exception of using 45 optimization cycles for volume ratio 0.7 because of an anomaly that occurs at this volume ratio for 60 optimization cycles). The optimization outputs of this analysis for volume ratios of 1, 0.9, 0.8, 0.7, 0.6, and 0.5 are shown in Figure 5.9.

Figure 5.10 shows strain energy and stiffness normalized by the values for the model with a volume ratio of 1, plotted versus volume ratio. It shows that the model with a volume ratio of 0.9 had a stiffness that was only about 3% less than the rectangular wall, whereas the model with a volume ratio of 0.5 had a stiffness that was 2/3 of that of the rectangular wall. It therefore appears that 10 to 20% reductions in volume are possible without causing substantial reductions in member stiffness, but larger reductions in volume will have a large effect on stiffness.

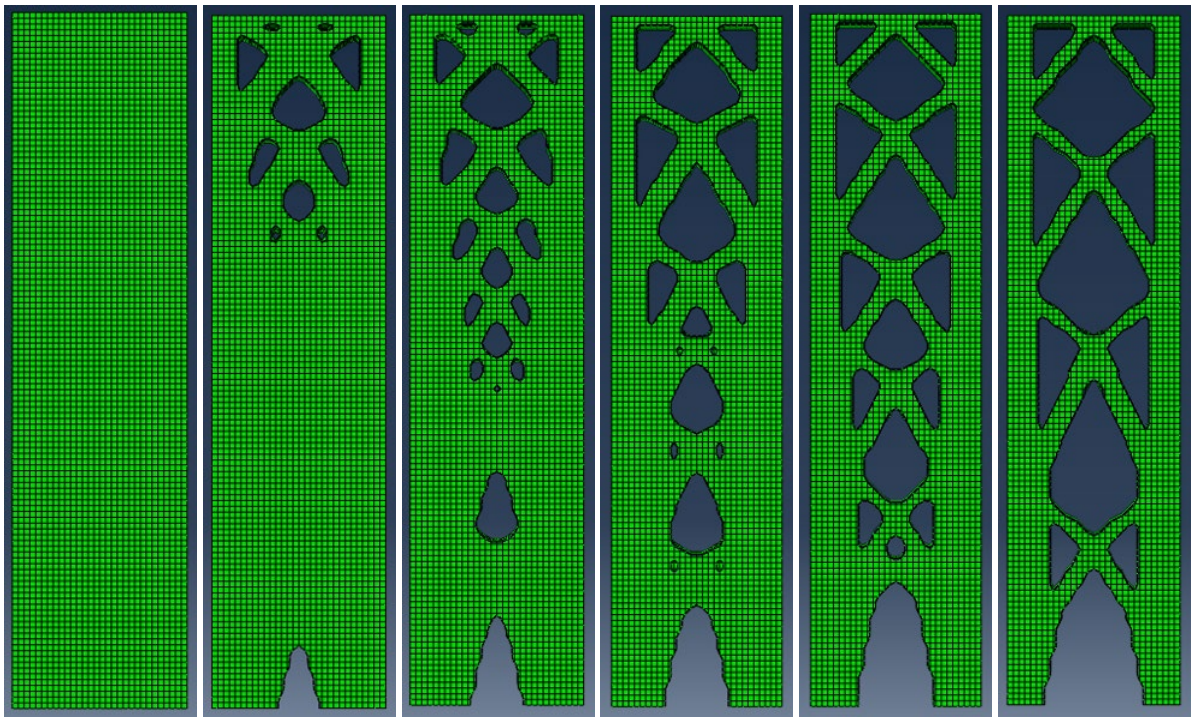

Figure 5.9: Optimized profiles for different volume ratios (element type C3D8H and mesh size of 0.5 in.)

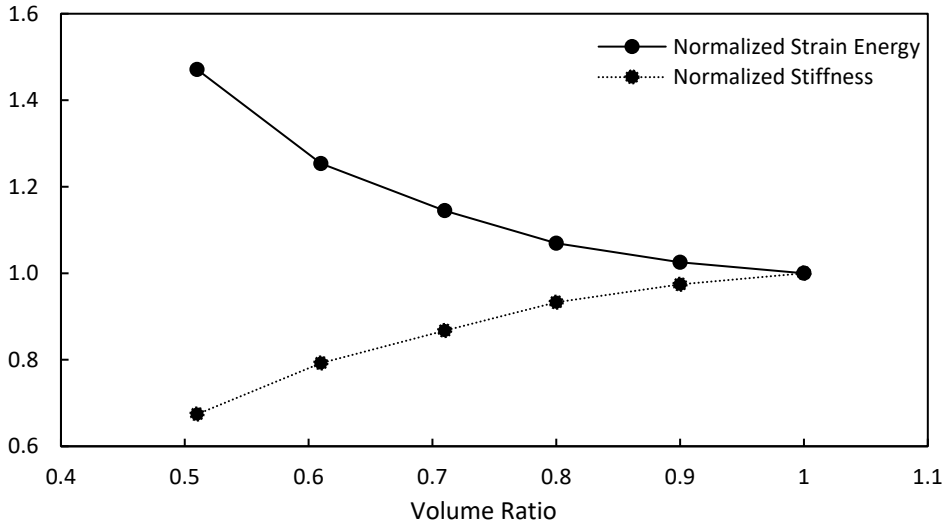

Figure 5.10: Normalized strain energy and stiffness versus volume ratio (element type C3D8H and mesh size of 0.5 in.)

5.3.2 Post-Processing for Further Analysis

Since the topology optimization algorithm only supports linear elastic, perfectly plastic, and hyperplastic material models that were shown to produce unrealistic representations of member response in Section 5.1, the model outputs shown in Section 5.3.1 were modeled using discrete reinforcement and concrete damage plasticity, as described in Section 5.1. To do this, the topology optimized geometries were extracted from Tosca and imported back to ABAQUS. This process is inherently imperfect and results in element nodes located outside the optimized geometry that cause problems in subsequent analyses. The topology optimization results were therefore smoothed using ABAQUS procedures controlled by an ISO value and a percent reduction.

The smoothing process removes or adds material to the surface: if the ISO is 0, the section obtained after smoothing is the non-optimized or original cross-section before topology optimization, if ISO is 1, the surface of the geometry is placed within the optimized geometry, thereby reducing the volume of the smoothed shape beyond the defined constraint value. This is shown in Table 5.7 and Figure 5.11, which report the final volume ratio, computation time for the smoothing process, top displacement and stiffness of the smoothed model, and the smoothed optimized geometries for ISO values of 0, 0.3, 0.5, and 0.7. All other parameters were constant. The models had discrete reinforcement and were thus assigned the material properties listed in Table 5.1 and were subjected to a lateral force of 1.5 kip at the top.

Table 5.7 shows that ISO values of 0.5 and 0.7 produced reasonable results with a final volume ratio close to the target volume ratio of 70%. Use of an ISO of 0.5 may be the most preferable option because Figure 5.11 shows that some parts of the optimized structure with an ISO of 0.7 appeared somewhat overly slender. Moreover, the final volume obtained for ISO of 0.7 was less

than the target volume, which may be undesirable. Note that selection of an appropriate ISO value should be done with consideration. This is a purely geometric process of element and node removal that does not consider the extent to which element removal effects the distribution of stresses. Use of the ISO value to change the volume ratio to a value substantially different from the target volume ratio could lead to inefficient or unconservative geometries.

Table 5.7: Effect of ISO value on optimized results (element type C3D10 and mesh size of 0.5 in.)

ISO Value	Volume Ratio	Computation Time (min)	Top Displacement (in.)	Normalized Stiffness
0	1.00	171	0.046	1.00
0.3	0.76	58	0.051	0.91
0.5	0.74	55	0.052	0.90
0.7	0.68	53	0.055	0.85

(a) ISO = 0 (b) ISO = 0.3 (c) ISO = 0.5 (d) ISO = 0.7

Figure 5.11: Obtained optimized profile after smoothing (element type C3D10 and mesh size of 0.5 in.)

Another factor affecting the smoothing process is percentage reduction. It defines the percent of faces (0-100) to be removed during the data reduction process to minimize the complexity of the model. This is illustrated in Figure 5.12, which shows the meshed models for percent reduction values of 0, 50, and 100. Table 5.8 and Figure 5.13 show the effects of the percent reduction variable on calculated stresses, wall stiffness, and computation time. The percentage reduction did not affect the calculated stresses (Figure 5.13) or stiffness of the optimized section, but it did reduce the computation time considerably (Table 5.8).

Table 5.8: Effect of percent reduction on optimized results (element type C3D10 and mesh size of 0.5 in.)

Percent Reduction	**Volume Ratio**	**Computation Time (min)**	**Top Displacement (in.)**	**Normalized Stiffness**
0	0.74	55	0.052	0.9
50	0.74	11	0.052	0.9
100	0.74	5	0.052	0.9

(a) (b) (c)

Figure 5.12: Optimized profile after smoothing with percent reduction (a) 0, (b) 50, and (c) 100, (element type C3D10, mesh size of 0.5 in., ISO = 0.5

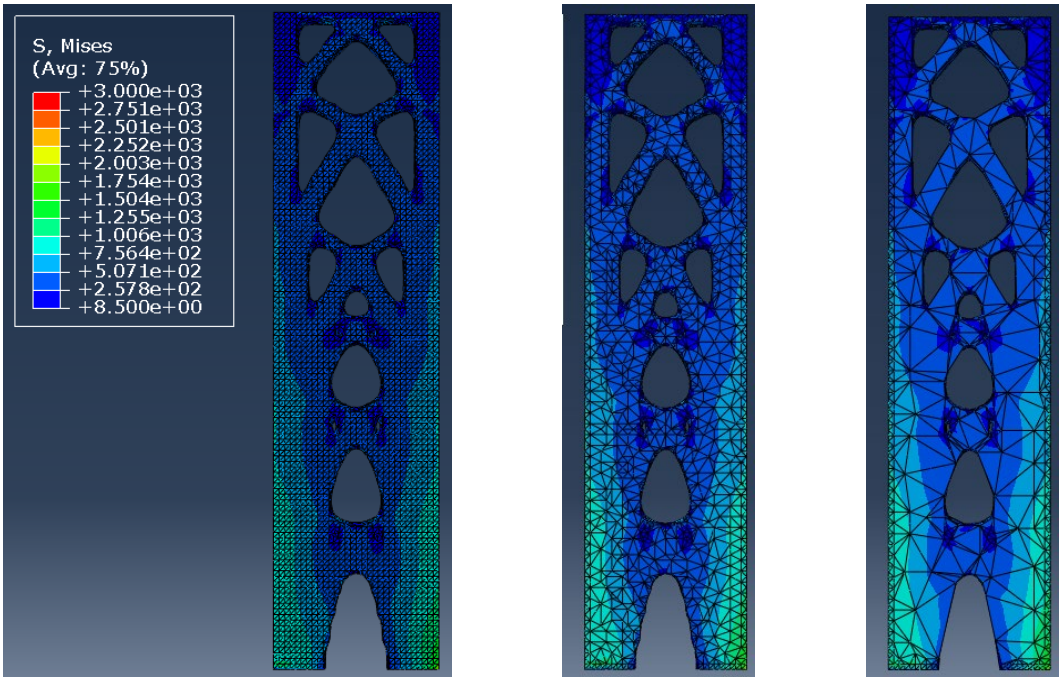

Figure 5.13: Von-Mises stress in optimized profile after smoothing with percent reduction (a) 0, (b) 50, and (c) 100, (element type C3D10, mesh size of 0.5 in., ISO = 0.5

Based on these preliminary analyses, and using an element type of C3D10, a mesh size of 0.5 in., an ISO of 0.5, and a 100 percent reduction, optimized and smoothed geometries were obtained for target volume ratios of 0.5, 0.6, 0.7, 0.8, and 0.9. Table 5.9 shows the target and final volume ratios. The final optimized and smoothed shapes used for further analysis are shown in Figure 5.14. In the subsequent sections, the actual volume ratio is reported, not the target value.

Table 5.9: Target versus actual volume ratios after extraction using smoothing process

Target Volume Ratio	0.5	0.6	0.7	0.8	0.9
Actual Volume Ratio	0.51	0.65	0.74	0.84	0.92

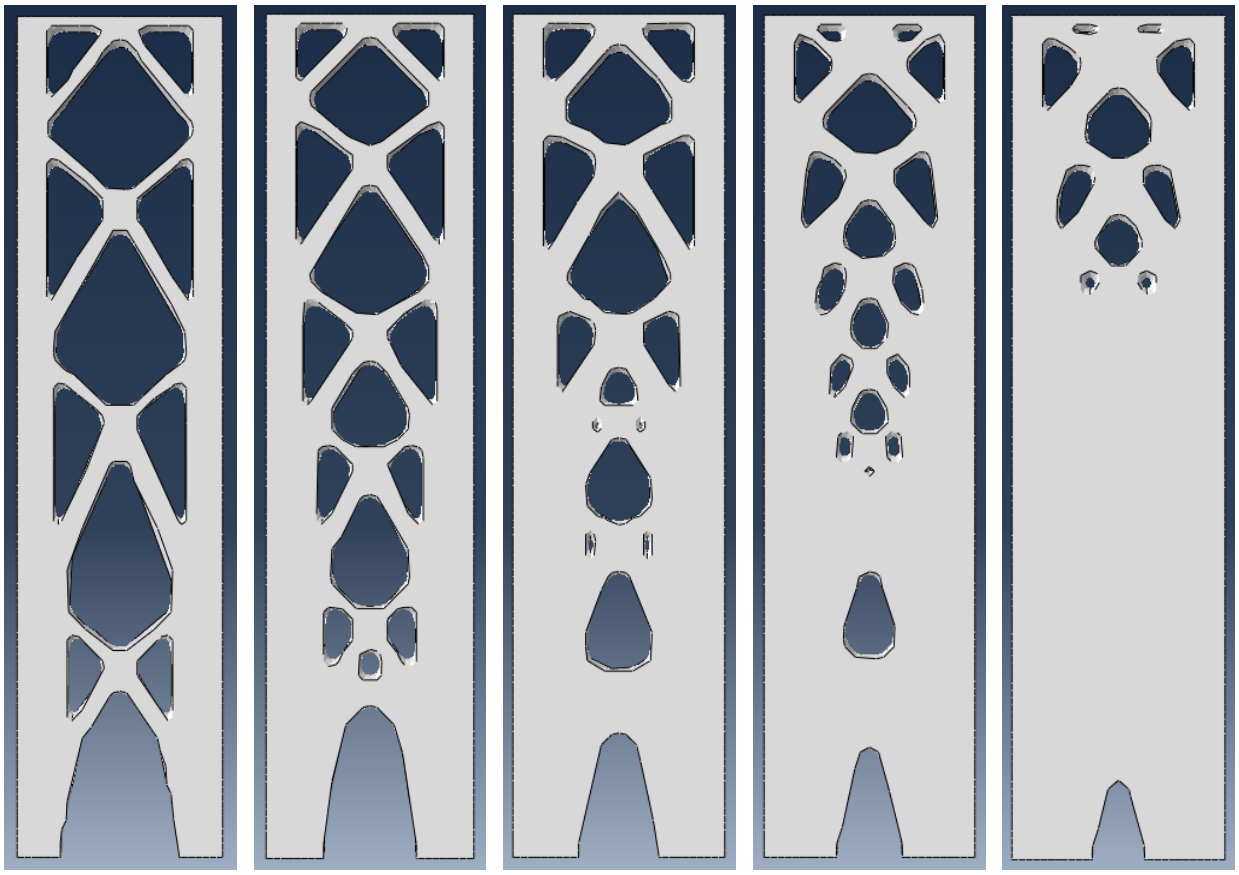

Figure 5.14: Final optimized profiles after smoothing and importing to ABAQUS for volume ratios of (a) 0.51, (b) 0.65, (c) 0.74, (d) 0.84, and (e) 0.92

5.4 FE Analysis of Optimized RC Walls

Although a complete analysis of all the optimized sections up to failure is beyond the scope of this study, the optimized wall models in Figure 5.14 were subjected to a lateral force of 6 kip, which is less than the force required to cause reinforcement yielding, to simulate the stiffness and strength of the walls after cracking. With reduction in volume, it is expected the stiffness and strength of the walls will be reduced. Although the flexural strength of the wall can easily be increased with added reinforcement, it may be difficult to place reinforcement within the optimized web. It is therefore assumed that fiber reinforced concrete (FRC) with a tensile strength of 10% of the concrete compressive strength is used for construction of the optimized walls. Because the strength of the FRC was assumed to be a function of the concrete compressive strength, both stiffness and strength of the optimized walls were related to the concrete compressive strength. Design of FRC is more involved than this, but for simplicity it is assumed herein that FRC mixtures are available that, through some manipulation of fiber type, fiber content, and concrete compressive strength, exhibit tensile strengths close to 10% of the specified concrete compressive strengths used in this analysis.

For each volume ratio, iterative analysis runs were conducted to identify the concrete compressive strength required to maintain a lateral strength of 6 kips and a stiffness up to 3 kips of lateral force similar to that of the control specimen constructed from concrete with a 6,000 psi compressive strength and reinforced as described in Chapter 3. The required concrete compressive strengths are listed in Table 5.10 and shown in Figure 5.15. For an approximately 30% reduction in wall volume, the concrete compressive strength required to maintain a lateral strength of 6 kips was approximately 13,000 psi. The strength in these cases was limited by failure of the slender web components in tension. Walls with larger volume reductions would require even higher concrete

strengths (e.g. ultra-high performance concrete), reinforcement would be necessary, or reduced wall strength would need to be accepted. Stiffness up to 3 kips of lateral force can theoretically be maintained even for a volume ratio of 65% with concrete compressive strengths of 10,000 psi.

Table 5.10: Concrete compressive strength required to maintain same strength and stiffness as the control specimen

Volume Ratio	Required Concrete Compressive Strength (psi)	
	Similar Strength	Similar Stiffness
100	6000	6000
92	6000	7000
84	7000	8000
74	11000	9000
65	15000	10000
51	25000	15000

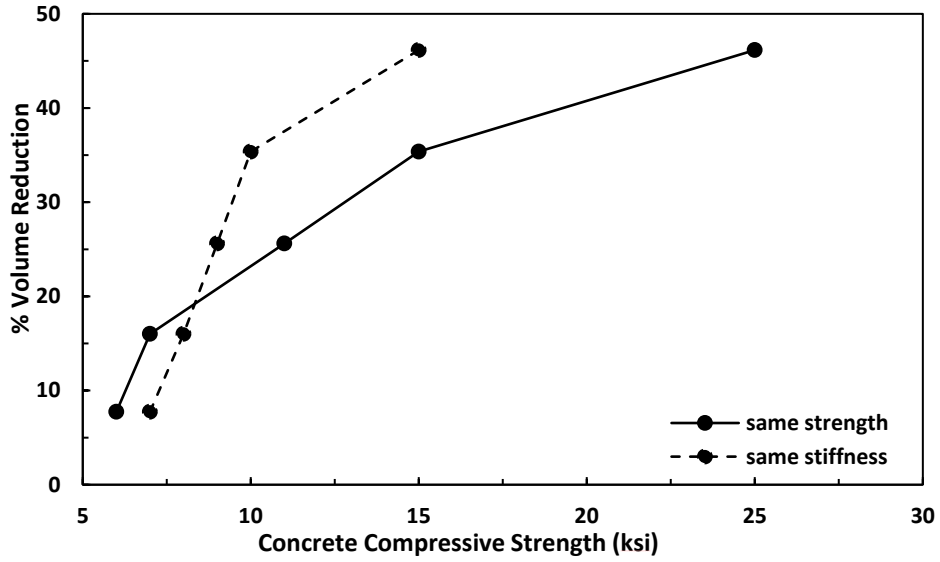

Figure 5.15: Percentage volume reduction versus required concrete compressive strength to maintain the same strength and stiffness as that of the control specimen

Figure 5.16 shows plots of force versus top displacement for walls with different volume ratios with concrete compressive strengths selected to result in lateral strengths of 6 kips. It can be observed that the optimized sections with volume ratios of 0.92 and 0.84 had larger deflections at peak load than the control specimen. This is because the modulus of elasticity is similar in the three models but the former two had reduced material volume. The walls with volume ratios of 0.74, 0.65, and 0.51 all had concrete compressive strengths that were between 2 and 4 times that of the control specimen. Hence the curves showed higher stiffness than the control specimen.

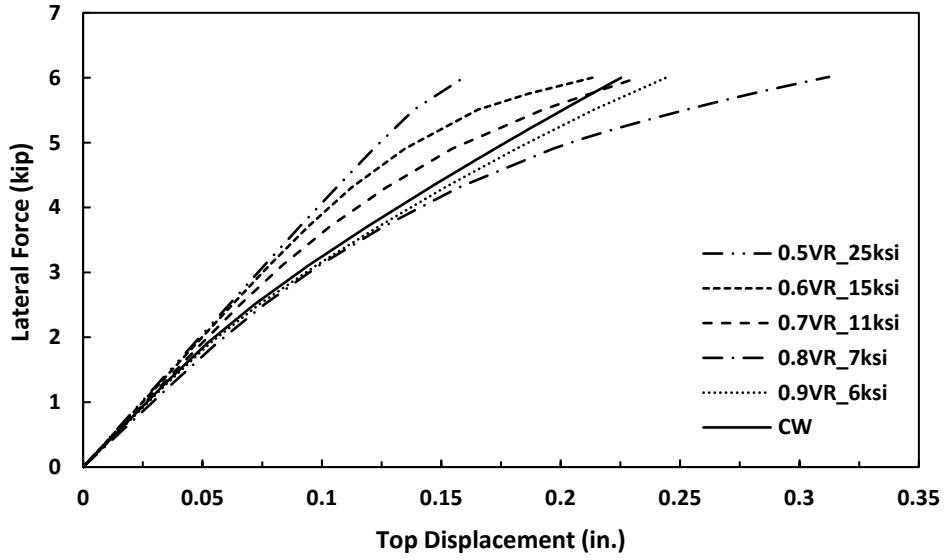

Figure 5.16: Lateral force versus top displacement in models with volume ratios between 0.5 and 0.9 designed to maintain a lateral strength of 6 kips

Figure 5.17 shows force versus deflection results from models with different volume ratios and concrete compressive strengths selected to produce stiffnesses up to 3 kips of force similar to that of the control specimen (listed in Table 5.10). It is clear that modest increases in concrete compressive strength were, theoretically, sufficient to sustain the initial stiffness of the specimens. Figure 5.17, however, shows that several of these walls failed to exhibit a strength of 6 kips because of failure of ties within the web.

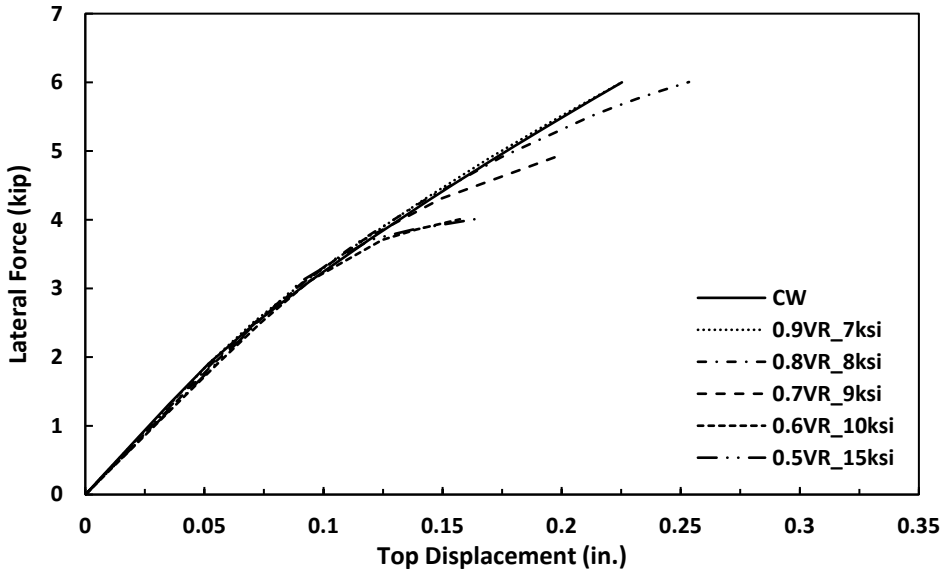

Figure 5.17: Lateral force versus top displacement in models with volume ratios between 0.5 and 0.9 designed to maintain the same stiffness as control wall up to 3 kips of lateral force

5.5 Discussion

The results from this study are intended to be a starting point for detailed analysis of topology optimized RC structures.

A major limitation for topology optimization of RC structures is not being able to include reinforcing bars in the model used for optimization and the requirement to use linear material properties. These features of the algorithm were accommodated by using a rule of mixtures to define the stiffness and density of an effective composite material in the models used for analysis. However, this approach does not provide for a fully optimized composite system. It is reasonable to expect that an algorithm which somehow considers the presence of discrete reinforcement would produce a different optimized geometry.

The behavior of the optimized walls can be estimated using a model with discrete reinforcement within the boundary elements and the non-linear concrete damaged plasticity material model with

some correction made to account for base rotation (as discussed in Section 5.1, but omitted in Section 5.4, which was focused on theoretical comparisons and not actual behavior). These analyses show that the lack of reinforcement in the ties leads to large strains and failure that limits the strength of the walls. This is shown in Figure 5.18, which shows contour plots of the principal strains in the optimized walls designed to exhibit lateral strengths of 6 kips. Even for the 0.9 volume ratio wall, the ties near the top of the section experience large strains and ultimately limit the lateral strength of the model. It is therefore crucial that validated nonlinear 2nd order models by used in design to estimate deformation demands on the components of topology optimized structures, and that appropriate reinforcement detailing be provided to accommodate the anticipated deformation demands, which can be substantially amplified relative to roof-level drift due to model geometry.

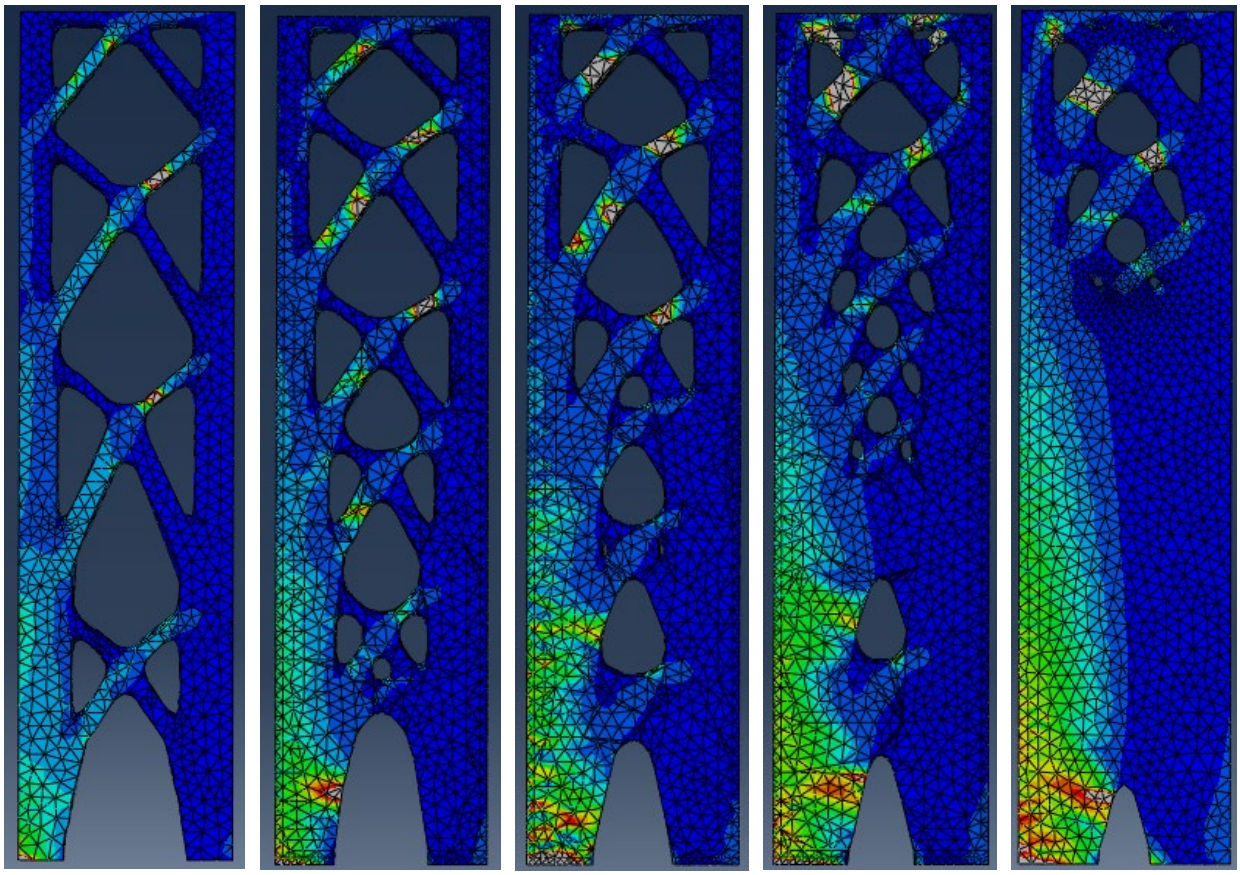

Figure 5.18: Principal strains at 6-kip lateral force in optimized sections designed to have strengths of at least 6 kips with volume ratios of (a) 0.51, (b) 0.65, (c) 0.74, (d) 0.84, and (e) 0.92 (element type C3D10, 0.5 in. mesh size)

CHAPTER 6 - CONCLUSIONS AND FUTURE WORK

6.1 Conclusions

Topology optimization has yet to make a significant impact in the civil engineering industry despite being well established in the automotive and aerospace industries. The reasons behind this include the (1) difficulty of constructing the complex, irregular, and nonlinear designs that result from topology optimization; (2) difficulty of applying topology optimization algorithms, which typically assume homogenous materials, to reinforced concrete (RC) structures; and (3) paucity of tests of topology optimized RC structures, and therefore limited understanding of behavior of optimized structures.

This study was intended to be a starting point toward future development of topology optimized RC structures. The study scope included use of additive manufacturing (3D printing) to construct a complex truss-shaped RC structure, testing of the RC specimen to failure under monotonic pushover loading, and exploration of the use of commercially-available topology-optimization software for design and then modeling of optimized RC slender walls under lateral force.

The following observations and conclusions were made based on the reported work:

1) At small scales, it is feasible to use additively manufactured (3D printed) formwork for construction of RC structures. This new type of formwork could conceivably be used for precast and cast-in-place RC structures. The 3D printing of formwork appears more promising than direct printing of concrete because it allows for placement of reinforcement and use of additive manufacturing in a more controlled off-site environment.
2) Reductions of stiffness were not proportional to reductions in volume. The “optimized” wall specimen had a volume that was 43% less than the volume of the control specimen (and a volume of reinforcement that was 7% more than in the control specimen) but it

exhibited a stiffness that was only 20 to 30% less than the stiffness of the control specimen. Finite element models with a volume ratio of 0.9 had cracked lateral stiffnesses that were only about 3% less than the rectangular wall, whereas finite element models with a volume ratio of 0.5 had cracked lateral stiffnesses that were 33% less than the stiffness of the rectangular wall. This is likely because most of the volume was removed near mid-depth, and therefore had little effect on the moment of inertia of the walls. The cracked lateral stiffness was the slope of line joining 1.2 and 3 kip on the force-displacement curve.

3) Finite element analyses show that modest increases in concrete compressive strength can help compensate for reductions in stiffness. The stiffness up to half of the lateral force required to yield the wall longitudinal reinforcement can theoretically be maintained in relation to the rectangular wall even for a volume ratio of 65% by increasing the concrete compressive strength from 6000 to 10000 psi.
4) Failure of the optimized wall specimen was associated with buckling and crushing of struts within the web. Digital image correlation data also showed large strains concentrating where an inclined tie met the vertical strut. It is therefore crucial that appropriate reinforcement detailing be provided to accommodate anticipated (local) deformation demands, which can be amplified relative to roof-level (global) drift due to geometry. It may also be necessary to conduct a nonlinear 2nd order analysis during design to estimate deformation demands on components of topology optimized structures.
5) The finite element analyses show that the unreinforced ties within the web were the weakest portions of the optimized models and limited their strength. Even for the 0.9 volume ratio wall, ties near the top of the wall exhibited large tensile strains and ultimately

limited the lateral strength of the model. Ties require sufficient strength and deformation capacity, which may require use of reinforcing bars or fiber reinforced concrete materials.

6) It was observed that the number of optimization cycles required to reach convergence was independent of mesh size but strongly affected by element type and target volume ratio. More cycles were required to reach convergence for elements with fewer nodes and smaller target volume ratios (i.e., larger reductions in volume).
7) If an evolutionary structural optimization (ESO) style algorithm is used for topology optimization and a stability index like that proposed by Huang and Xie (2007), Huang and Xie (2010), and Mahmoud et al. (2018) is not integrated into the algorithm, it will be necessary for users to conduct multiple optimizations using different numbers of cycles to identify cases where anomalous increases in total strain energy occur.
8) Models with finer meshes resulted in optimized geometries with smaller members and more voids, and somewhat greater stiffness (smaller total strain energy) than models with coarser meshes. Use of meshes that were 1/2 to 1/16 of the wall thickness did not appear to converge (each change in mesh size led to a reduction in stiffness), although the changes in stiffness were small. A change from a 1 in. mesh to a 0.125 in. mesh resulted in only a 5% reduction in stiffness but required a computation time that was 17 times longer.
9) Models with different element types resulted in different optimized geometries but similar stiffness (similar total strain energy) if a sufficient number of optimization cycles was used.
10) Care should be taken when importing optimized geometries into FE software like Abaqus. The importing process, governed by ISO and "percent reduction" parameters, is a purely geometric process (not an optimization process) that can result in overly slender components and volume ratios less that that targeted during the optimization process. Use

of the ISO value to change the volume ratio to a value substantially different from the target volume ratio used for optimization could lead to inefficient, unstable, or weak geometries.

6.2 Future Work

Further experimental studies are necessary to develop guidance for design and manufacture of cost-competitive large-scale 3D printed formwork and to establish rules for design and detailing of optimized RC members. For example, the minimum formwork thickness and corner radius necessary for 3D printed formwork will depend on the materials used for fabrication, force demands, need for reuse (durability), and additive manufacturing procedures employed. If 3D printed formwork is to be reused in practice, a connection type for joining formwork components that is different from the one used in this study would be required (perhaps bolting).

Future work could be aimed at producing optimized geometries for reinforced concrete structures subjected to loads beyond those required to cause concrete cracking or yielding of the reinforcement. A challenge for topology optimization of RC structures is not being able to include the use of discrete reinforcing bars in the model and having to use linear material properties. These features of the algorithm were accommodated by using a user defined composite material to define the rigidity and density of an equivalent material in the models used for analysis. However, this approach does not provide for a fully optimized composite system after cracking and yielding because reinforcement placement and the redistribution of stresses associated with cracking are not considered during the optimization process. It is reasonable to expect that an algorithm which somehow considers the presence of discrete reinforcement and concrete cracking would produce a different optimized geometry.

Before topology optimization can be used widely in practice, it will be necessary to establish minimum design requirements to ensure optimized structures exhibit adequate strength, stability, and serviceability. There may be a need to reevaluate permitted construction tolerances because, as structures become increasingly optimized, they are likely to become more sensitive to differences between design and as-built properties. There will also be a need to consider how principles of reliability should be applied to optimized structures. Strength reduction factors in use today were not developed to account for the novel construction and analysis methods necessary for optimized structures.

REFERENCES

1. ACI 318 (2014). Building Code Requirements for Structural Concrete (ACI 318-14): Commentary on Building Code Requirements for Structural Concrete (ACI 318R-14): an ACI Report. *American Concrete Institute, Farmington Hills, Michigan.*
2. ASTM A36 / A36M (2019). Standard Specification for Carbon Structural Steel. *ASTM International, West Conshohocken, PA.* <www.astm.org>.
3. ASTM A853 (2019). Standard Specification for Steel Wire, Carbon, for General Use. *ASTM International, West Conshohocken, PA.* <www.astm.org>.
4. ASTM C39 / C39M (2018). Standard Test Method for Compressive Strength of Cylindrical Concrete Specimens. *ASTM International, West Conshohocken, PA.* <www.astm.org>.
5. ASTM C150 / C150M-19a (2019). Standard Specification for Portland Cement. *ASTM International, West Conshohocken, PA.* <www.astm.org>.
6. ASTM C494 / C494M (2017). Standard Specification for Chemical Admixtures for Concrete. *ASTM International, West Conshohocken, PA.* <www.astm.org>.
7. ASTM C566 (2019). Standard Test Method for Total Evaporable Moisture Content of Aggregate by Drying. *ASTM International, West Conshohocken, PA.* <www.astm.org>.
8. ASTM C618 (2019). Standard Specification for Coal Fly Ash and Raw or Calcined Natural Pozzolan for Use in Concrete. *ASTM International, West Conshohocken, PA.* <www.astm.org>.
9. ASTM C1017 / C1017M-13e1 (2013). Standard Specification for Chemical Admixtures for Use in Producing Flowing Concrete. *ASTM International, West Conshohocken, PA.* <www.astm.org>.
10. ASTM C1240 (2015). Standard Specification for Silica Fume Used in Cementitious Mixtures. *ASTM International, West Conshohocken, PA.* <www.astm.org>.
11. Chang, G. A., & Mander, J. B. (1994). Seismic energy-based fatigue damage analysis of bridge columns: part 1-evaluation of seismic capacity (Technical Report No. NCEER-94-0006) *University of Buffalo, New York.*
12. Donofrio, M. (2016). Topology Optimization and Advanced Manufacturing as a Means for the Design of Sustainable Building Components. *Procedia Engineering*, *145*, 638-645.
13. Feldman, L. R., Poudyal, U., & Cairns, J. (2018). Proposed Development Length Equation for Plain Bars. *ACI Structural Journal*, *115*(6), 1615-1623.
14. Hack, N., Wangler, T., Mata-Falcón, J., Dörfler, K., Kumar, N., Walzer, A. N., & Kaufmann, W. (2017). Mesh Mould: An On-Site, Robotically Fabricated, Functional Formwork. In *Second Concrete Innovation Conference (2nd CIC),* 19, 1-10.
15. Hambach, M., & Volkmer, D. (2017). Properties of 3D-Printed Fiber-Reinforced Portland Cement Paste. *Cement and Concrete Composites*, *79*, 62-70.
16. Hawkins, W. J., Herrmann, M., Ibell, T. J., Kromoser, B., Michaelski, A., Orr, J. J., & Veenendaal, D. (2016). Flexible Formwork Technologies – A State of the Art Review. *Structural Concrete*, *17*(6), 911-935.
17. Hillerborg, A., Modéer, M., & Petersson, P. E. (1976). Analysis of crack formation and crack growth in concrete by means of fracture mechanics and finite elements. *Cement and concrete research*, *6*(6), 773-781.
18. Huang, X., & Xie, Y. M. (2007). Convergent and Mesh-Independent Solutions for the Bi-Directional Evolutionary Structural Optimization Method. *Finite Elements in Analysis and Design*, *43*(14), 1039-1049.

19. Huang, X., & Xie, Y. M. (2010). A Further Review of ESO Type Methods for Topology Optimization. *Structural and Multidisciplinary Optimization*, *41*(5), 671-683.
20. Huq, M. S. (2018). High-Strength Steel Bars in Earthquake-Resistant T-Shaped Concrete Walls. *Doctoral dissertation, University of Kansas, Available on KU Library database <* https://kuscholarworks.ku.edu/handle/1808/27611*>*.
21. Januszkiewicz, K., & Banachowicz, M. (2017). Nonlinear Shaping Architecture Designed with using Evolutionary Structural Optimization Tools. In *IOP Conference Series: Materials Science and Engineering, IOP Publishing*, 245(8), 1-9.
22. Jewett, J. J. L. (2018). Design, Fabrication, and Testing of Plain Concrete Beams using Topology Optimization. *Master's thesis, Massachusetts Institute of Technology, Available on MIT Libraries database <* https://dspace.mit.edu/handle/1721.1/120634*>*.
23. Jewett, J. L., & Carstensen, J. V. (2019). Topology-Optimized Design, Construction and Experimental Evaluation of Concrete Beams. *Automation in Construction*, *102*, 59-67.
24. Jipa, A., Bernhard, M., Meibodi, M., & Dillenburger, B. (2016). 3D-Printed Stay-in-Place Formwork for Topologically Optimized Concrete Slabs. In *Proceedings of the 2016 Tx - A Emerging Design Technology Conference, Texas Society of Architects,* 97-107.
25. Johnsen, S. (2013). Structural topology optimization: basic theory, methods and applications. *Master's thesis, Institutt for produktutvikling og materialer, Available on NTNU Open database <* https://ntnuopen.ntnu.no/ntnu-xmlui/handle/11250/241794*>*.
26. Lee, J., & Fenves, G. L. (1998). Plastic-damage model for cyclic loading of concrete structures. *Journal of engineering mechanics*, *124*(8), 892-900.
27. Lim, S., Buswell, R. A., Le, T. T., Austin, S. A., Gibb, A. G., & Thorpe, T. (2012). Developments in Construction-Scale Additive Manufacturing Processes. *Automation in construction*, *21*, 262-268.
28. Lubliner, J., Oliver, J., Oller, S., & Oñate, E. (1989). A plastic-damage model for concrete. *International Journal of solids and structures*, *25*(3), 299-326.
29. Mahmoud, G. M., El Mostapha, P. B., & Toufik, P. C. (2018). Topological optimization of structures based on the BESO-Method. In *2018 4th International Conference on Optimization and Applications (ICOA), IEEE*, 1-7.
30. Moehle, J. P., & Sozen, M. A. (1978). Earthquake Simulation Tests of a Ten-Story Reinforced Concrete Frame with a Discontinued First-Level Beam. (Report No. UILU-ENG-78-2014) *University of Illinois at Urbana-Champaign.*
31. Ohmori, H. (2011). Computational Morphogenesis: Its Current State and Possibility for the Future. *International Journal of Space Structures*, *26*(3), 269-276.
32. Orakcal, K., Wallace, J. W., & Conte, J. P. (2004). Flexural modeling of reinforced concrete walls-model attributes. *Structural Journal*, *101*(5), 688-698.
33. Peters, B. (2014). Additive Formwork: 3D Printed Flexible Formwork. *Paper presented at the ACADIA 14: Design Agency, Los Angeles,* 517-522.
34. Raun, C., & Kirkegaard, P. H. (2014). Adaptive Mould-A Cost-Effective Mould System Linking Design and Manufacturing of Double-Curved Panels. In *Proceedings of IASS Annual Symposia*, *International Association for Shell and Spatial Structures (IASS)*, 11, 1-7.
35. Smith, M. (2009). ABAQUS/Standard User's Manual, *Version 6.9*. *Providence, RI: Dassault Systèmes Simulia Corp.*
36. Søndergaard, A., Feringa, J., Stan, F., & Maier, D. (2018). Realization of Topology Optimized Concrete Structures Using Robotic Abrasive Wire-Cutting of Expanded

Polystyrene Formwork. In *Robotic Fabrication in Architecture, Art and Design*, Springer, *Cham.*, 473-488.
37. Tao, Z., Wang, Z. B., & Yu, Q. (2013). Finite element modeling of concrete-filled steel stub columns under axial compression. *Journal of Constructional Steel Research*, *89*, 121-131.
38. Vazquez, A. N., Bhooshan, S., Sondergaard, A., Inamura, C., Zabel, J., & El–sayed, M. (2014). Design, analysis and fabrication of expressive, efficient shell structures: a prototype exploring synergy between architecture, engineering and manufacture. In *Proceedings of IASS Annual Symposia*, *International Association for Shell and Spatial Structures (IASS)*, 11, 1-12.
39. Vulcano, A., Bertero, V. V., & Colotti, V. (1988). Analytical modeling of RC structural walls. In *9th World Conference on Earthquake Engineering*, 6, 41-6.
40. Wahalathantri, B. L., Thambiratnam, D. P., Chan, T. H. T., & Fawzia, S. (2011). A material model for flexural crack simulation in reinforced concrete elements using ABAQUS. In *Proceedings of the first international conference on engineering, designing and developing the built environment for sustainable wellbeing*, *Queensland University of Technology*, 260-264.
41. Wille, K., & Boisvert-Cotulio, C. (2013). Development of non-proprietary ultra-high performance concrete for use in the highway bridge sector. *Report No. PB2013-110587, National Technical Information Service, Springfield, VA*.
42. Xie, Y. M., & Steven, G. P. (1993). A simple evolutionary procedure for structural optimization. *Computers & structures*, *49*(5), 885-896.

APPENDIX A

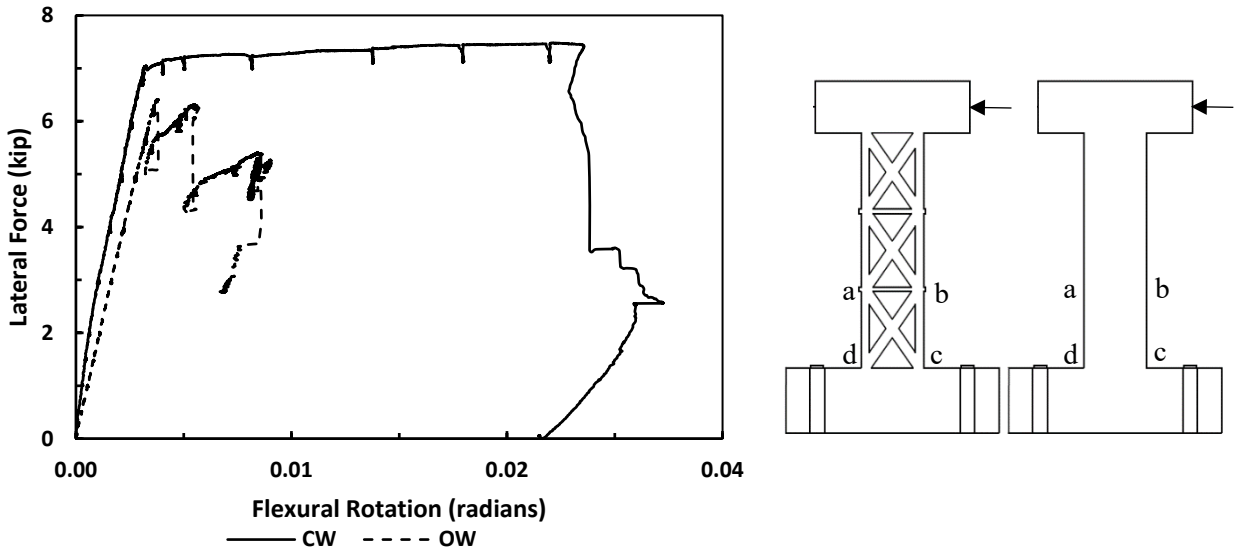

Figure A.1: Flexural rotation in control and optimized walls (level 1)

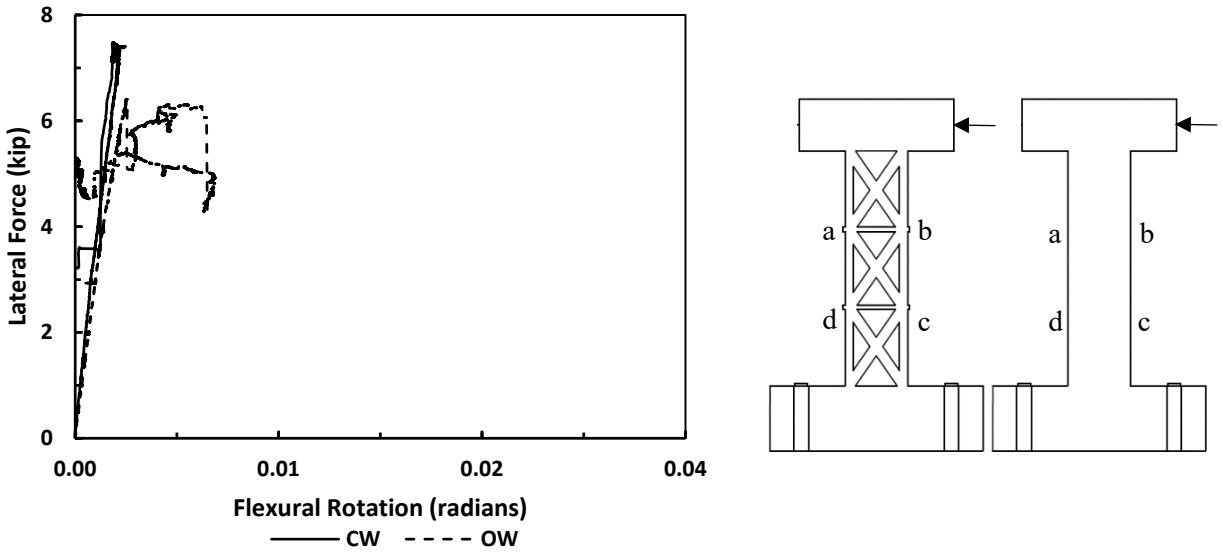

Figure A.2: Flexural rotation in control and optimized walls (level 2)

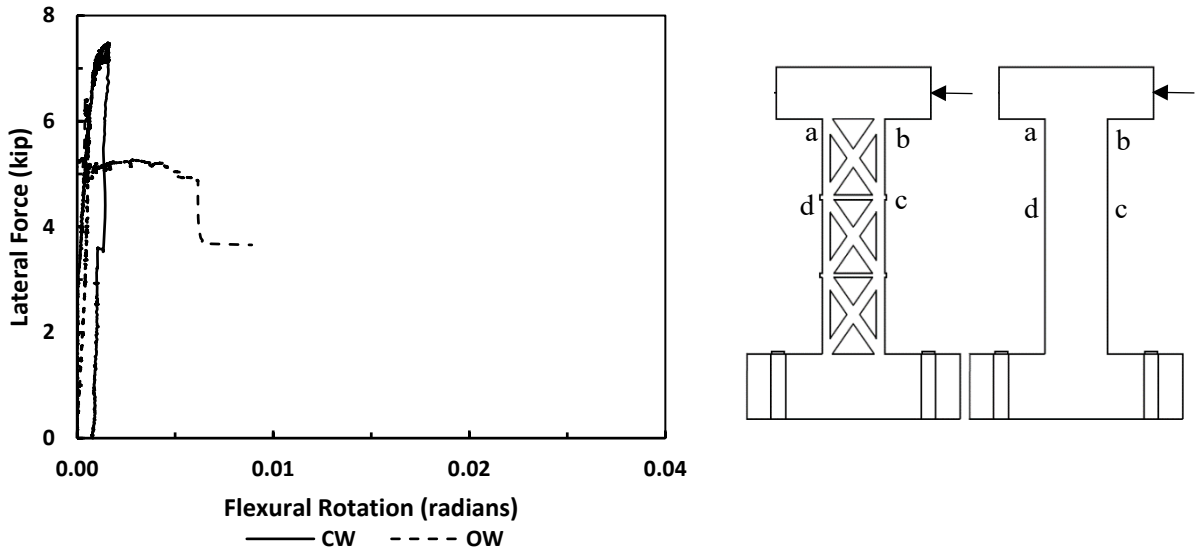

Figure A.3: Flexural rotation in control and optimized walls (level 3)

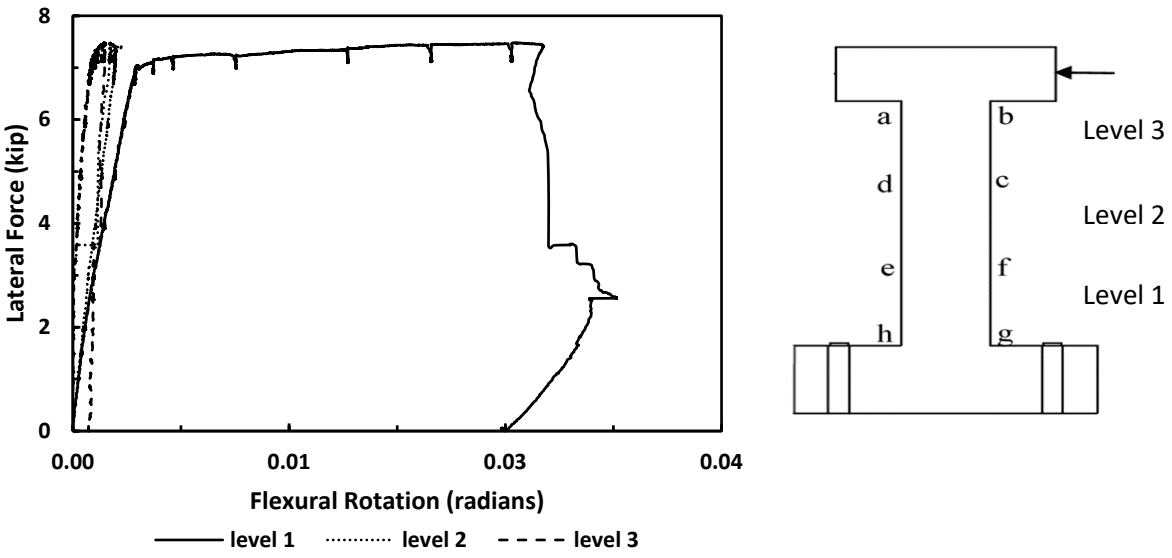

Figure A.4: Flexural rotation in control wall

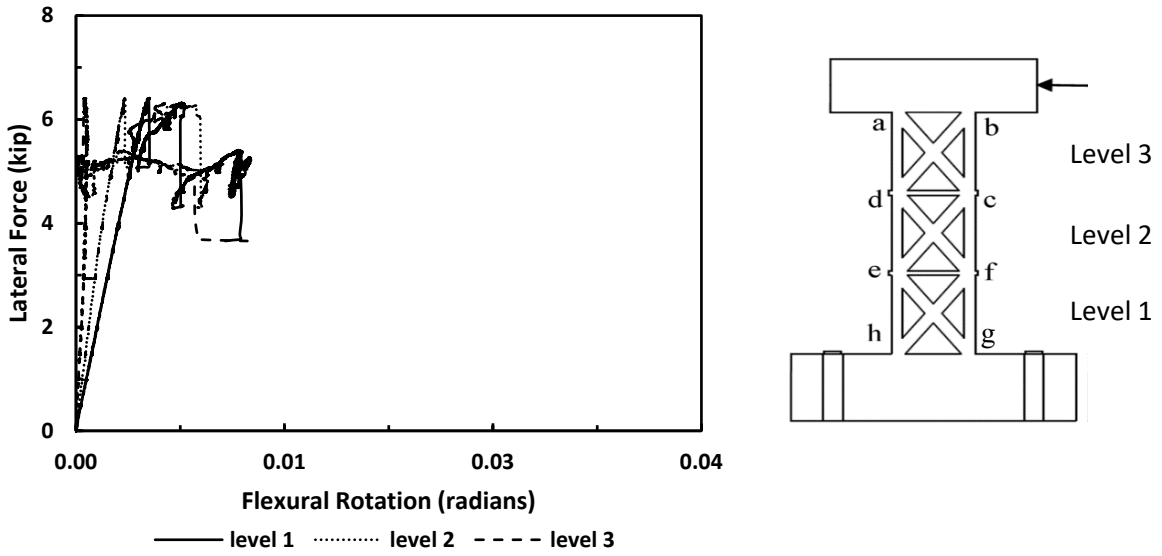

Figure A.5: Flexural rotation in optimized wall

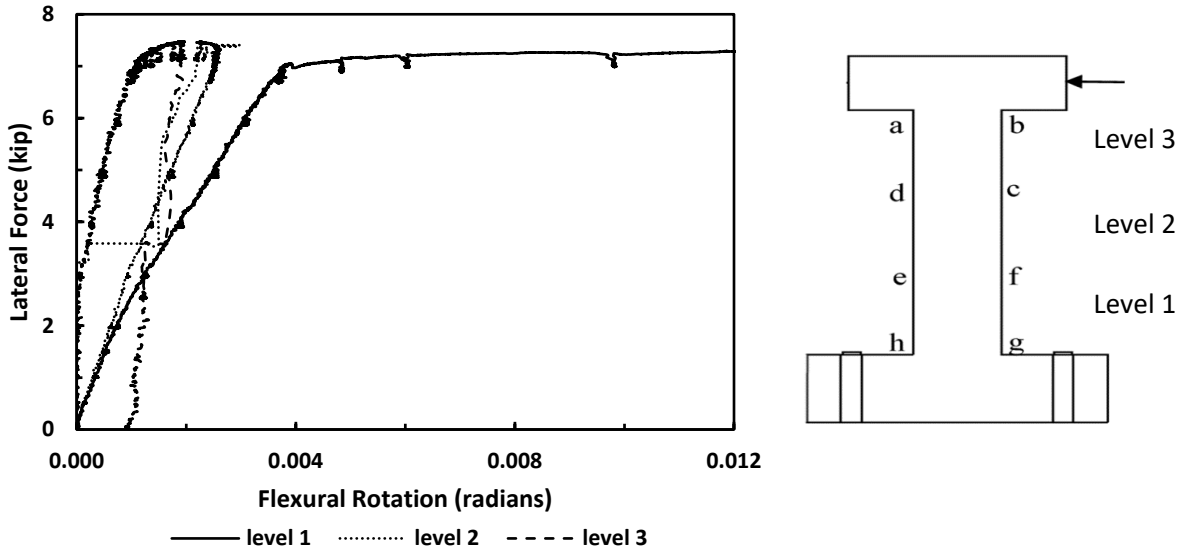

Figure A.6: Close-up of Fig. A.4 for flexural rotation up to 0.012 rad

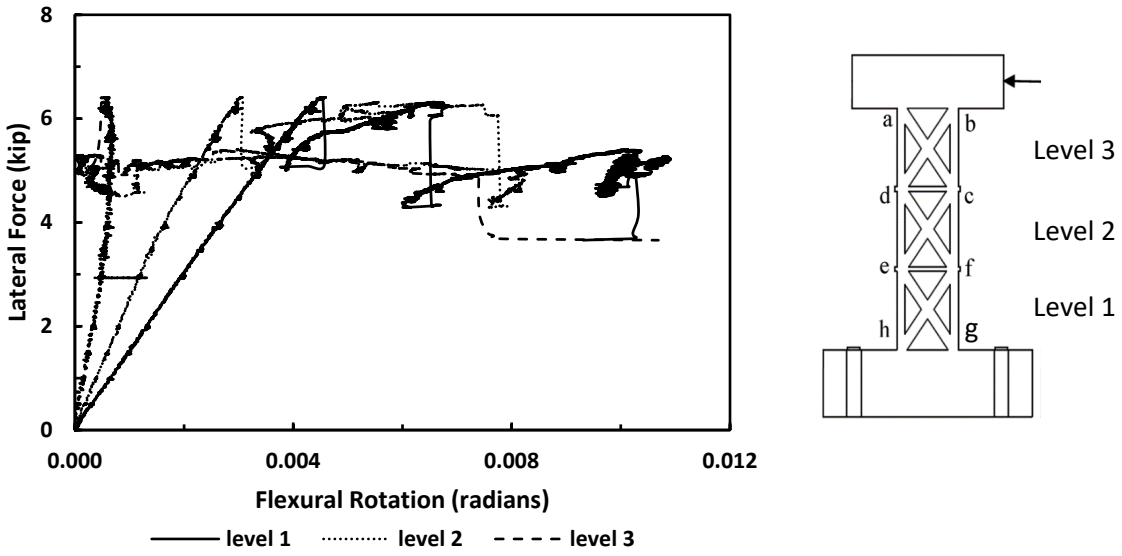

Figure A.7: Close-up of Fig. A.5 for flexural rotation up to 0.012 rad

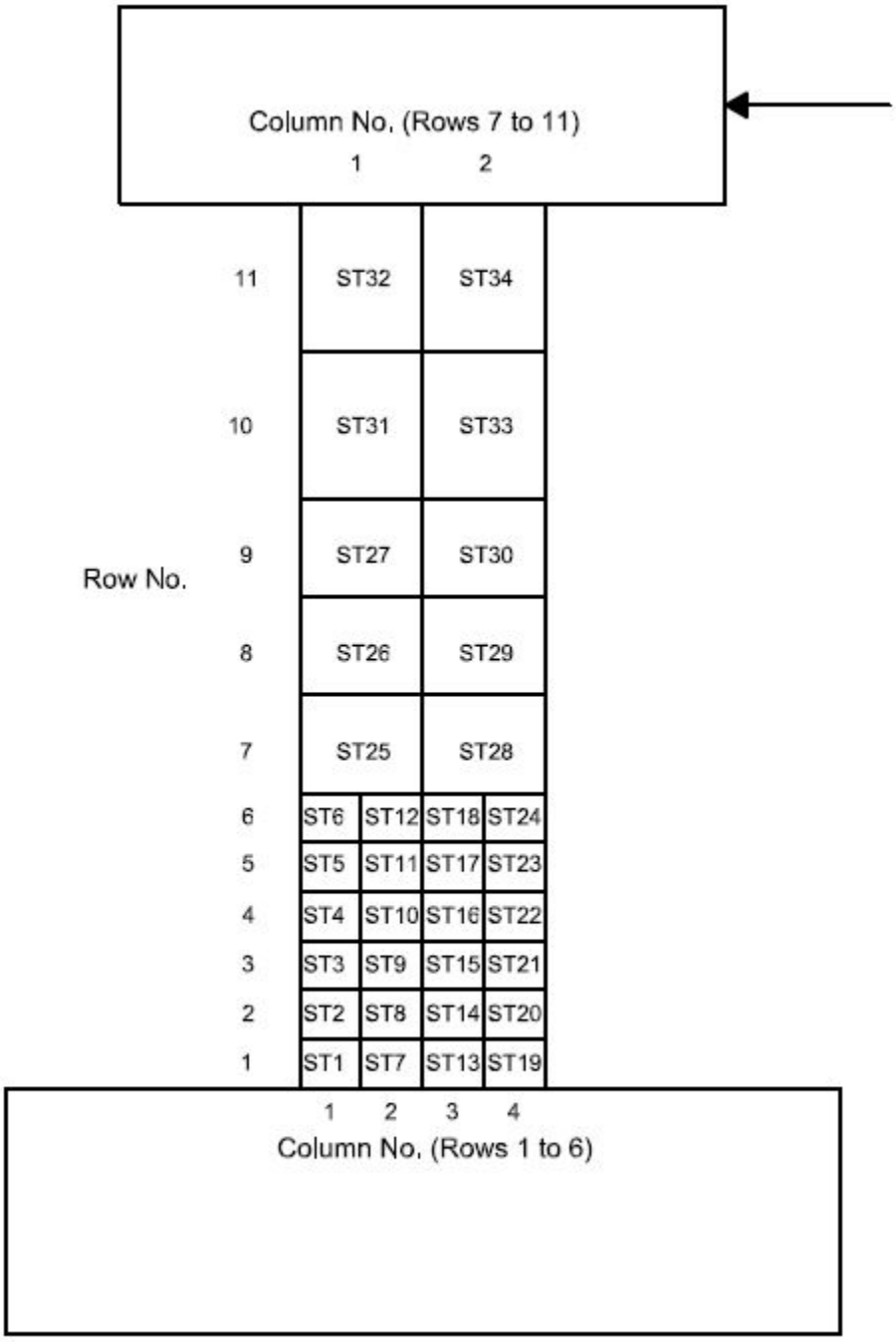

Figure A.8: Station locations

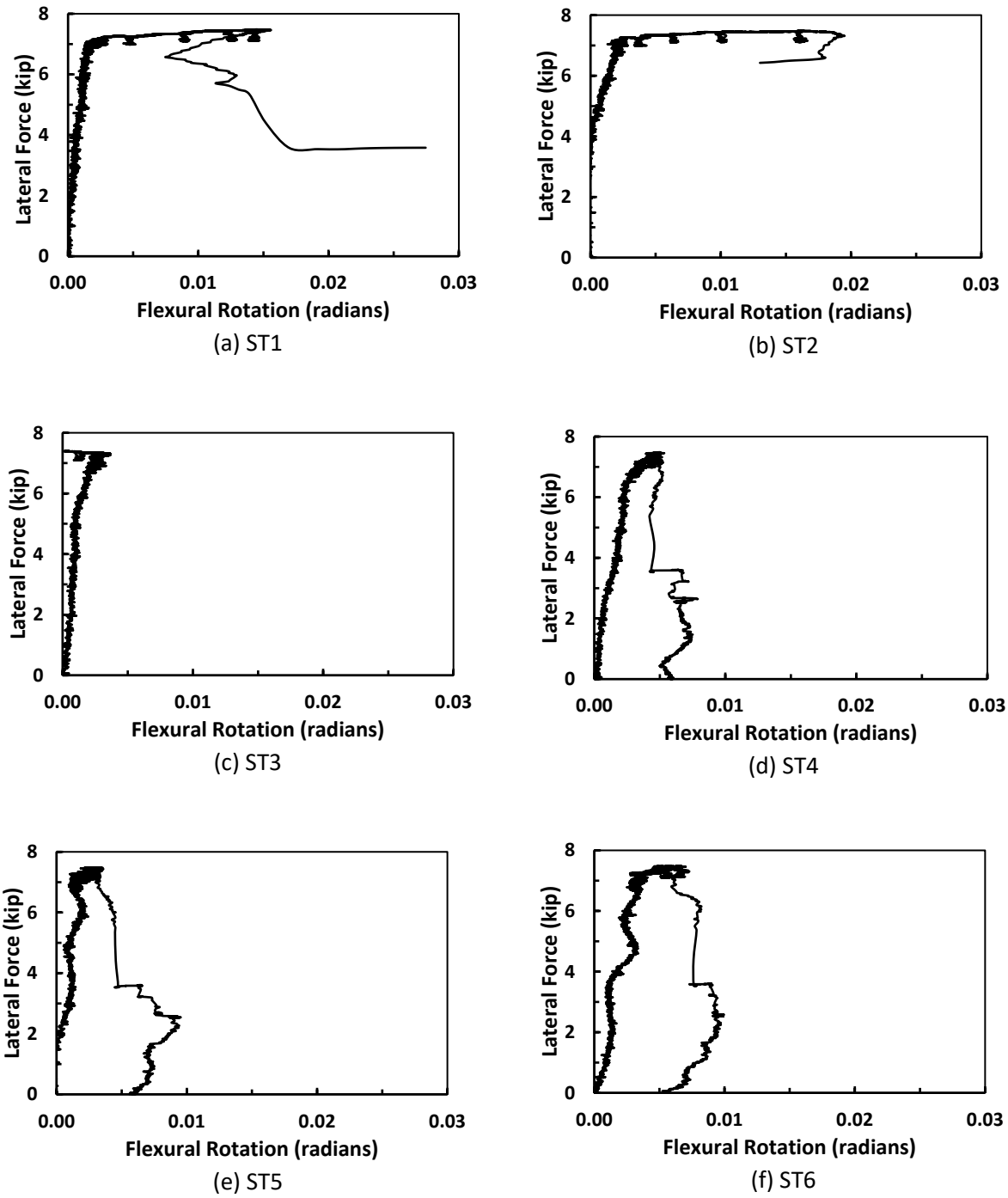

Figure A.9 Flexural rotations in level 1 of control wall (1st column, compression face)

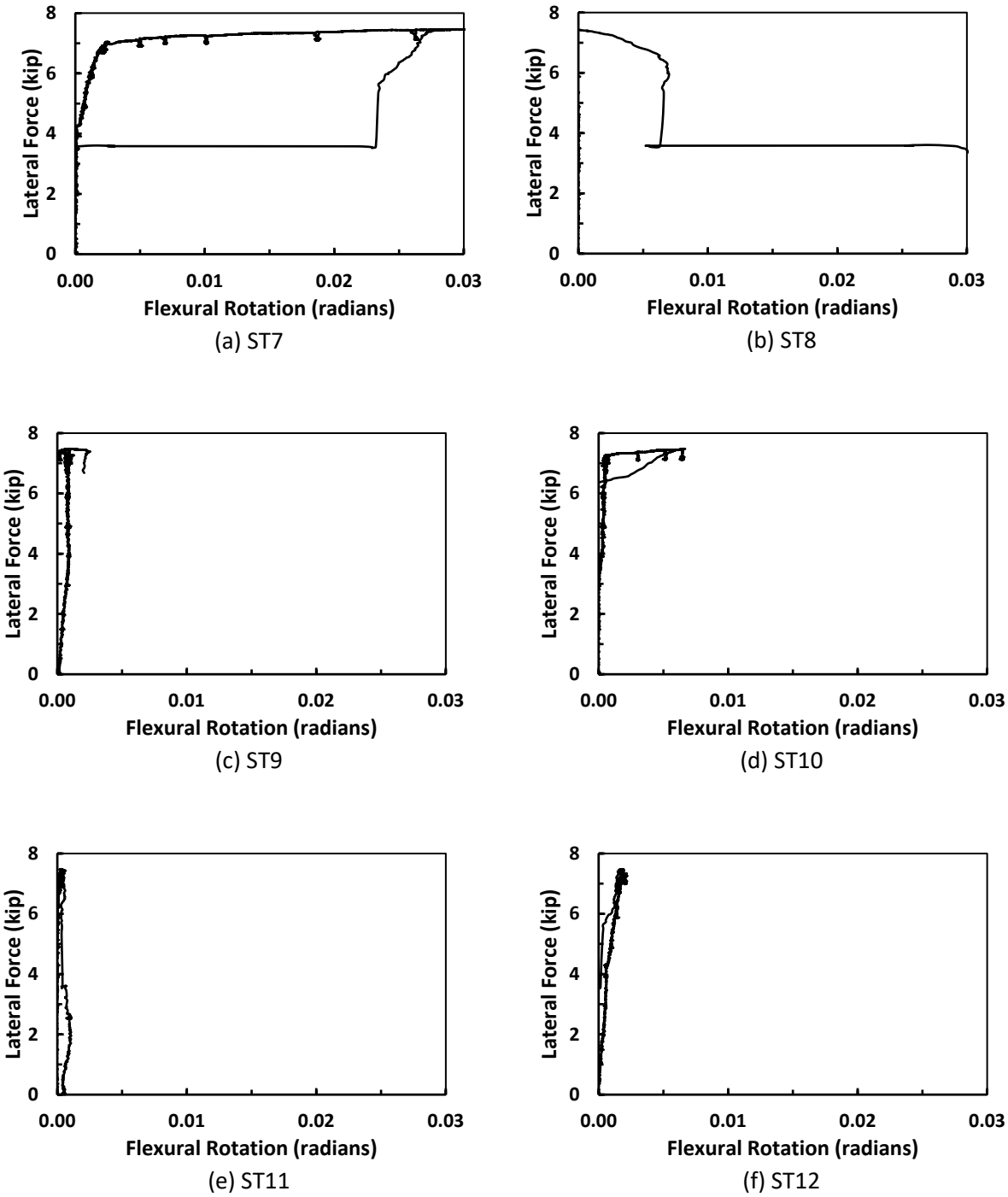

Figure A.10: Flexural rotations in level 1 of control wall (2nd column)

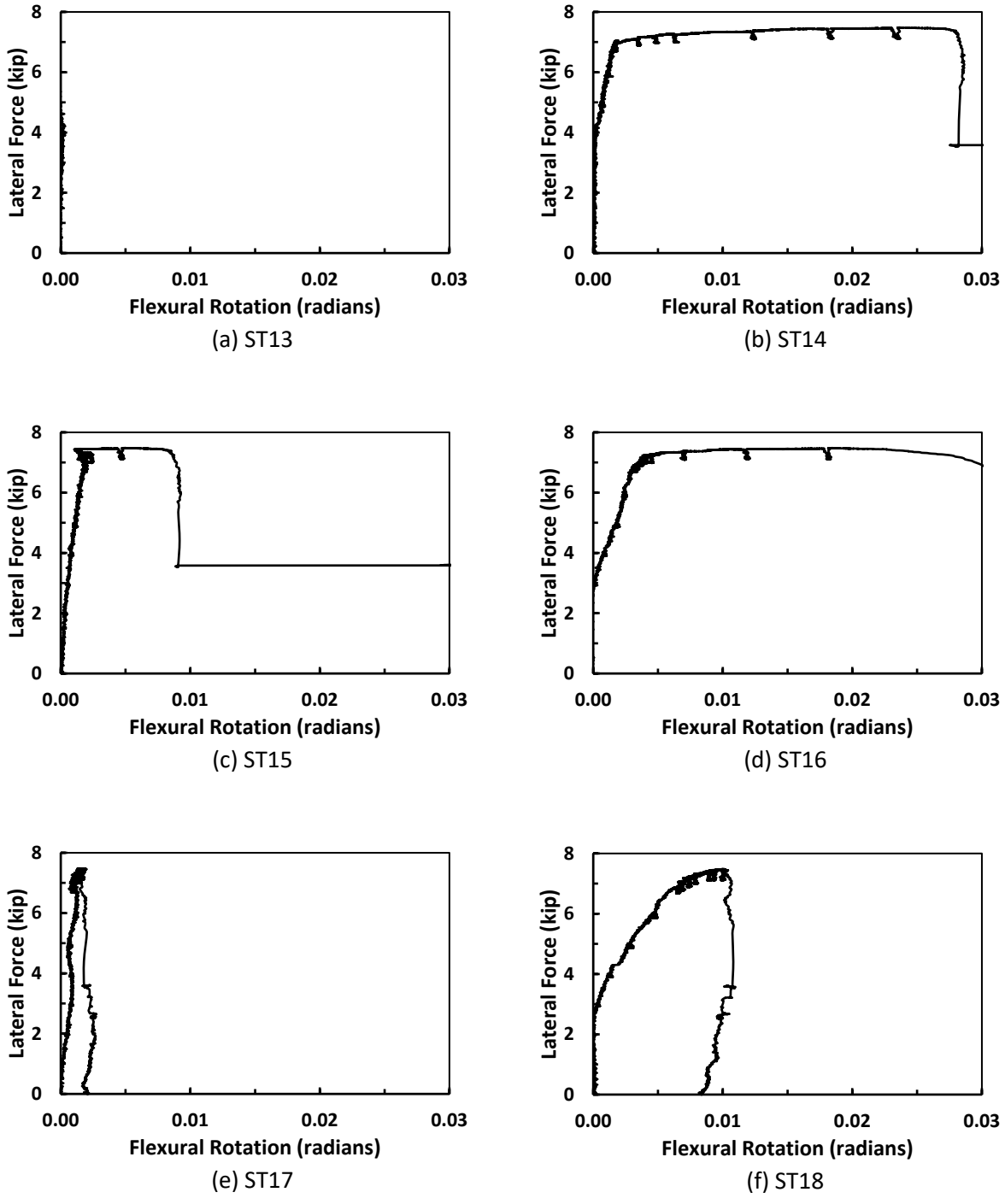

(a) ST13 (b) ST14

(c) ST15 (d) ST16

(e) ST17 (f) ST18

Figure A.11: Flexural rotations in level 1 of control wall (3rd column)

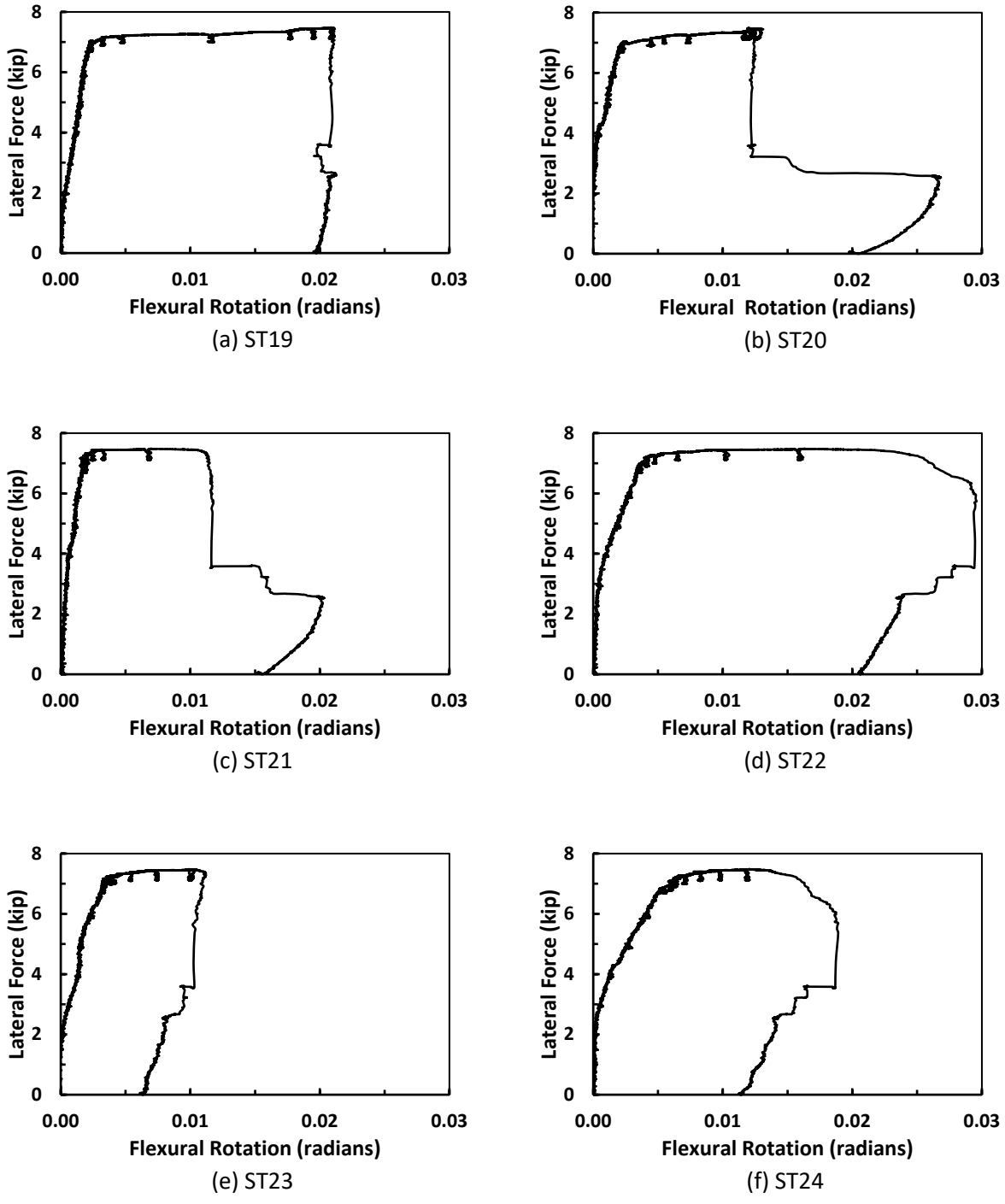

(a) ST19 (b) ST20

(c) ST21 (d) ST22

(e) ST23 (f) ST24

Figure A.12: Flexural rotations in level 1 of control wall (4th column, tension face)

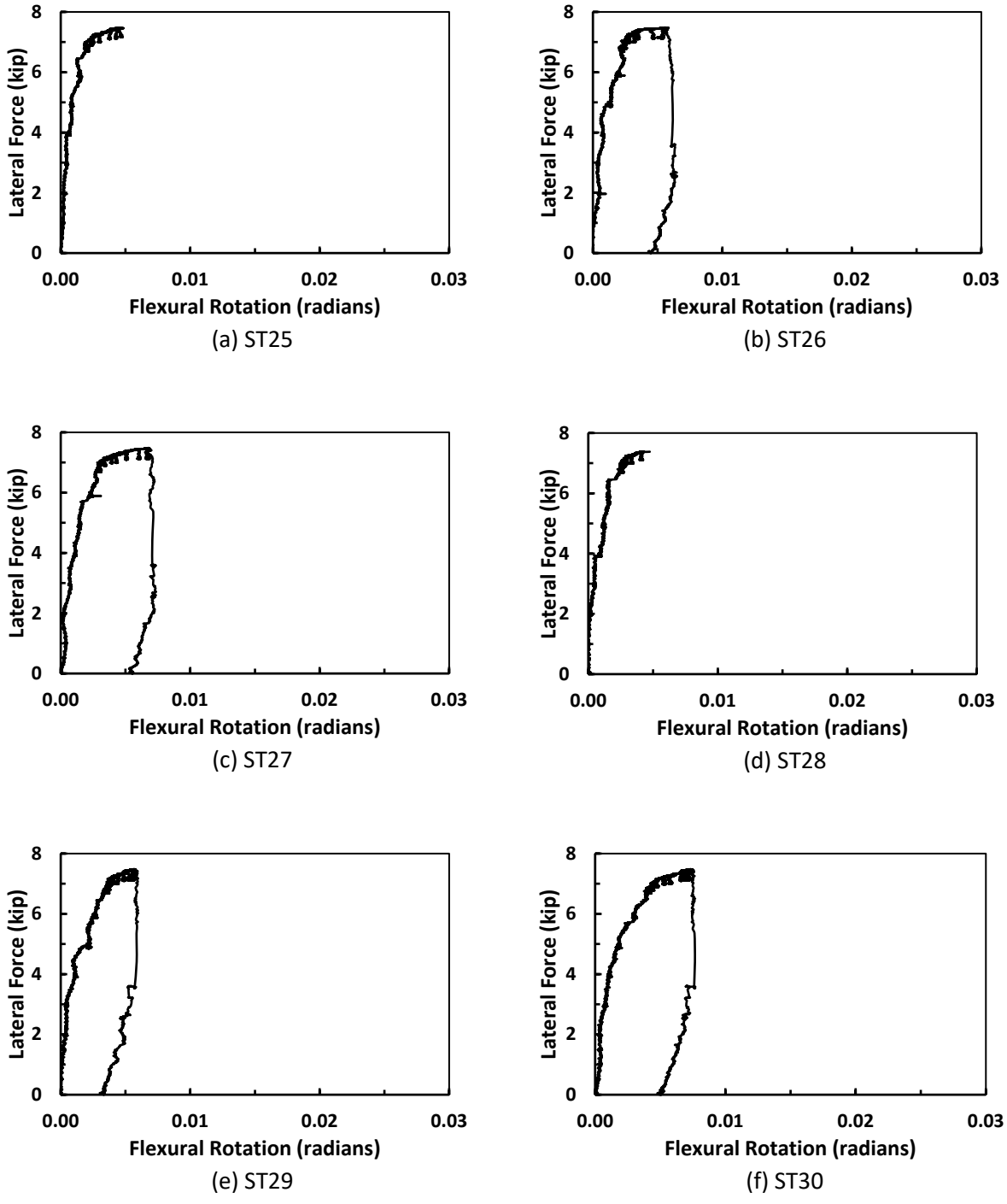

Figure A.13: Flexural rotations in level 2 of control wall

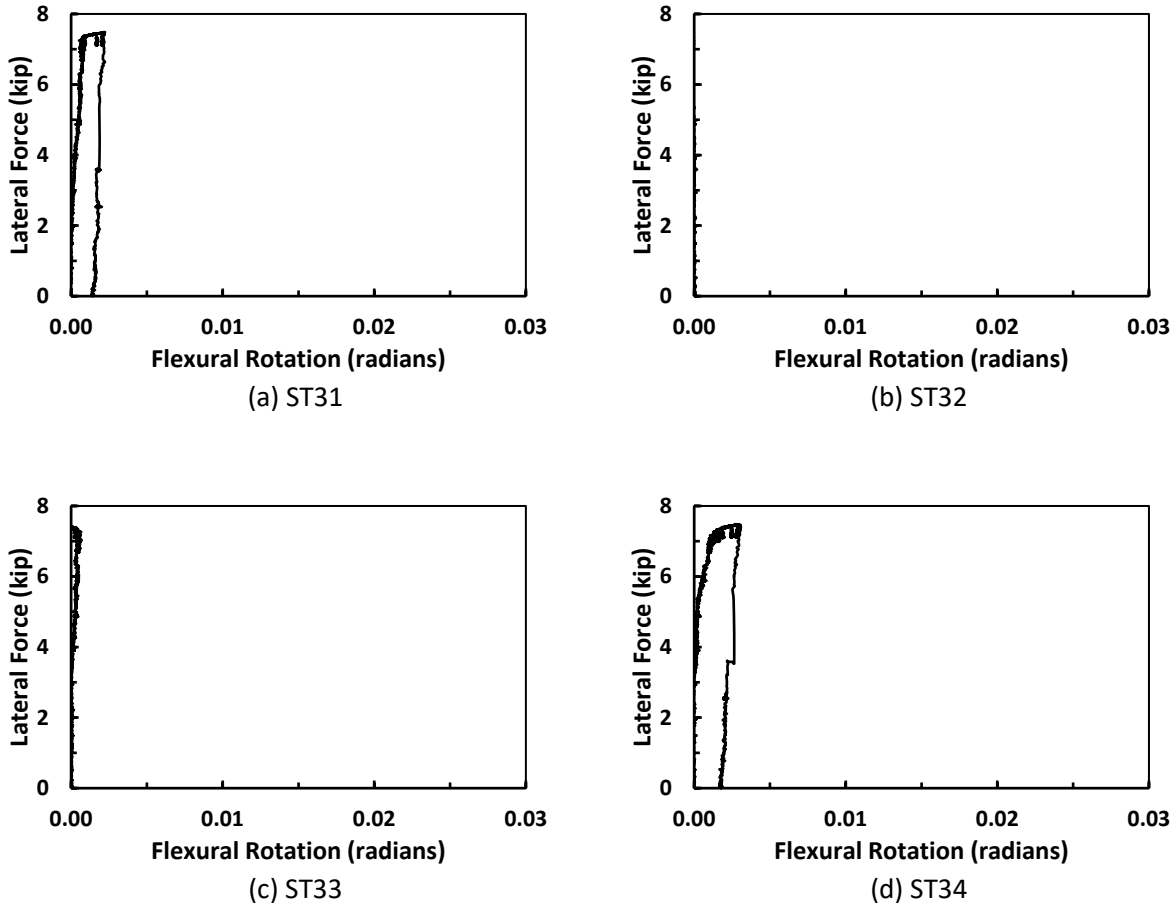

Figure A.14: Flexural rotations in level 3 of control wall

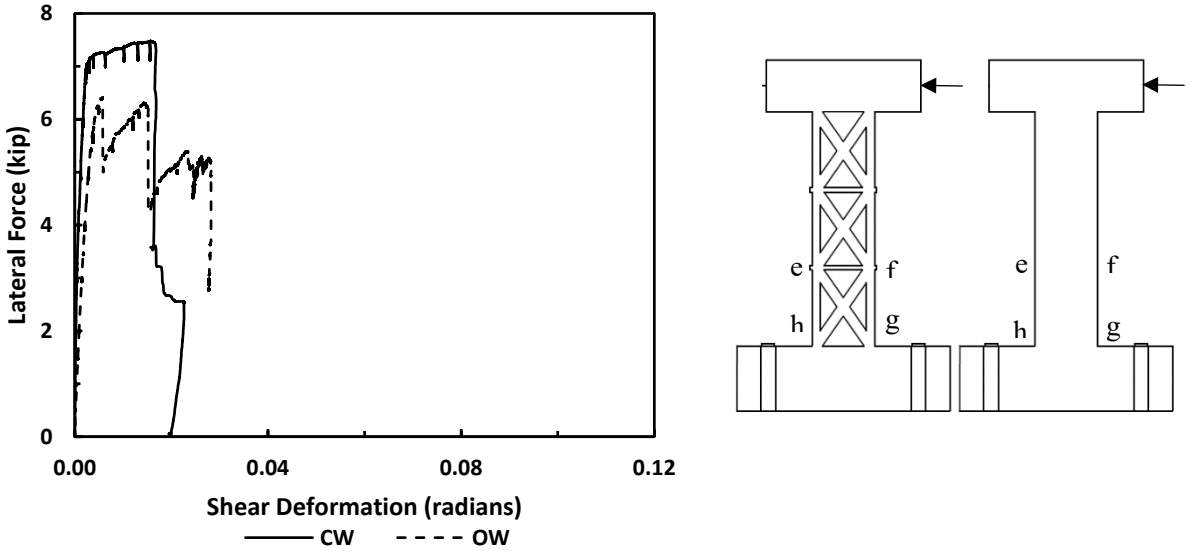

Figure A.15: Shear deformation in control and optimized walls (level 1)

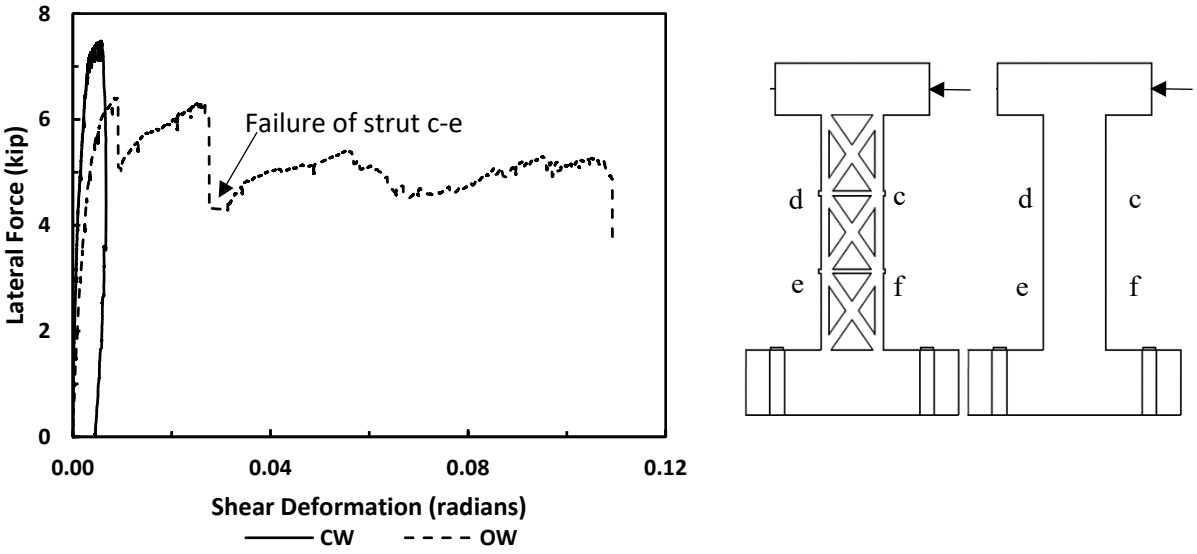

Figure A.16: Shear deformation in control and optimized walls (level 2)

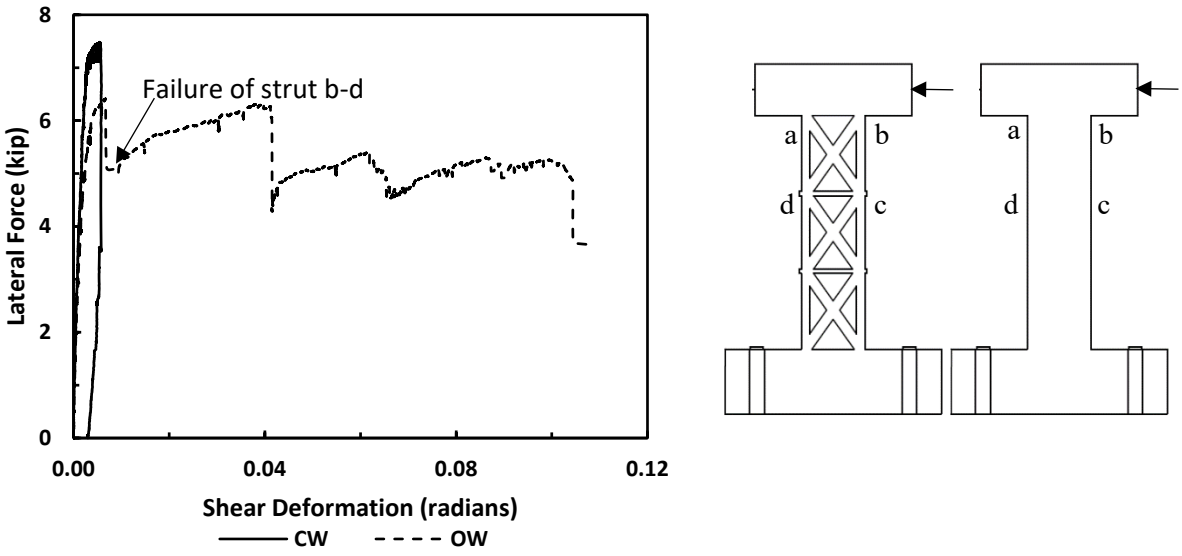

Figure A.17: Shear deformation in control and optimized walls (level 3)

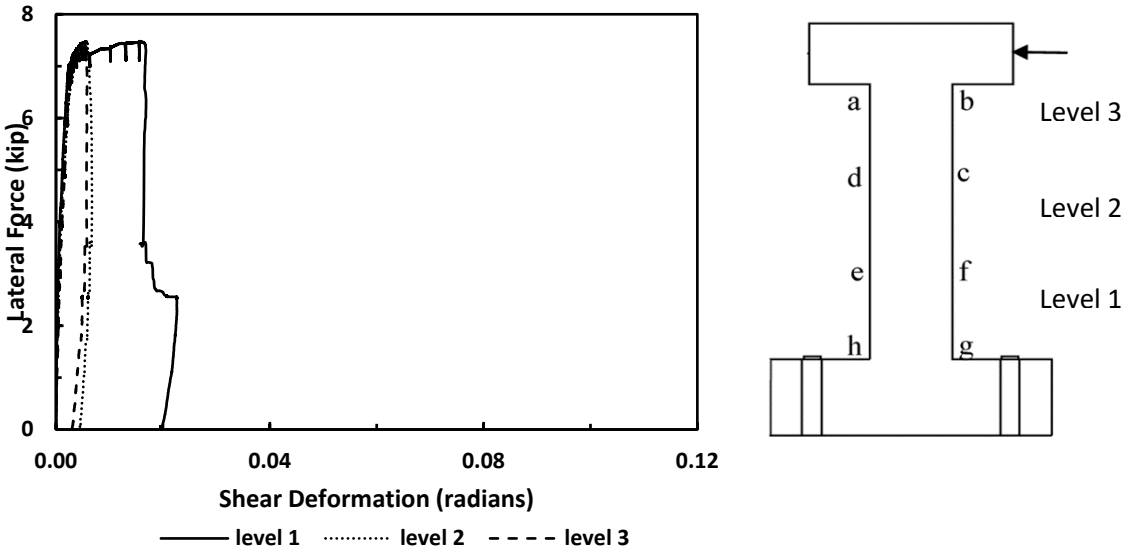

Figure A.18: Shear deformation in control wall

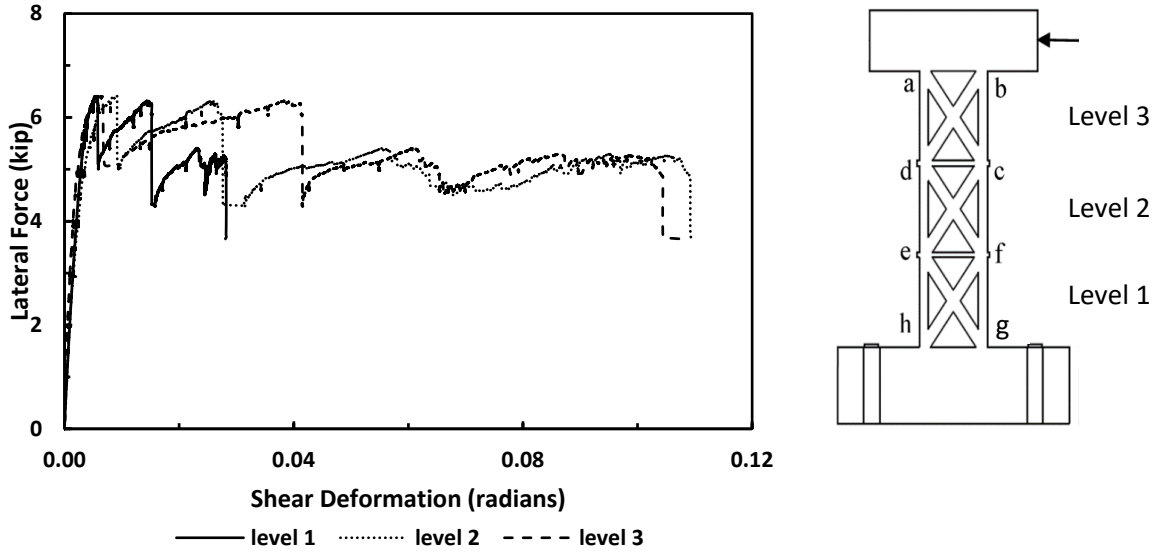

Figure A.19: Shear deformation in optimized wall

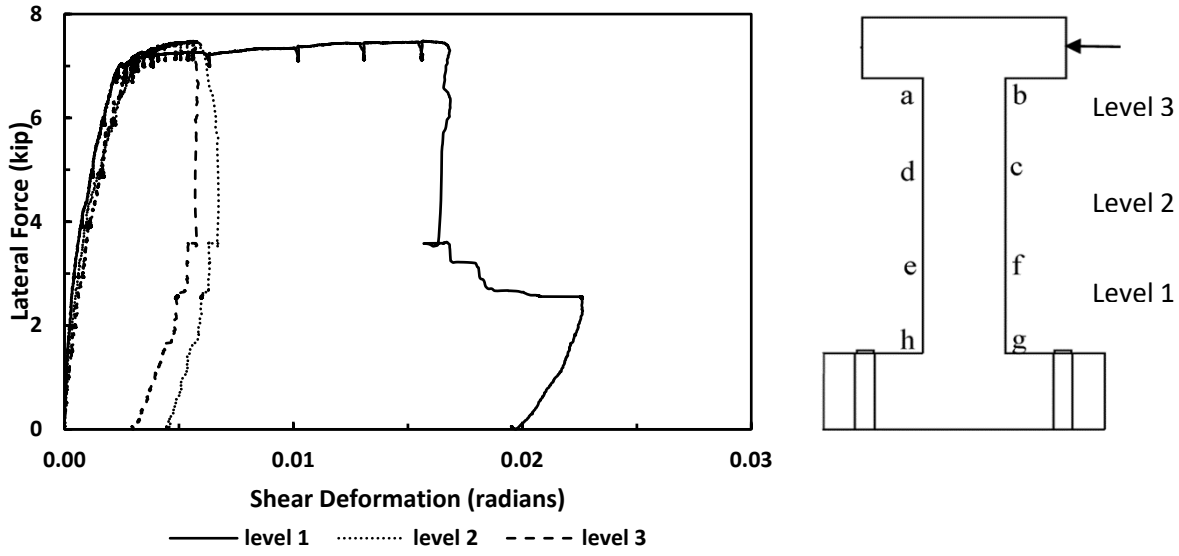

Figure A.20: Close-up of Fig. A.18 for shear deformation up to 0.03 rad

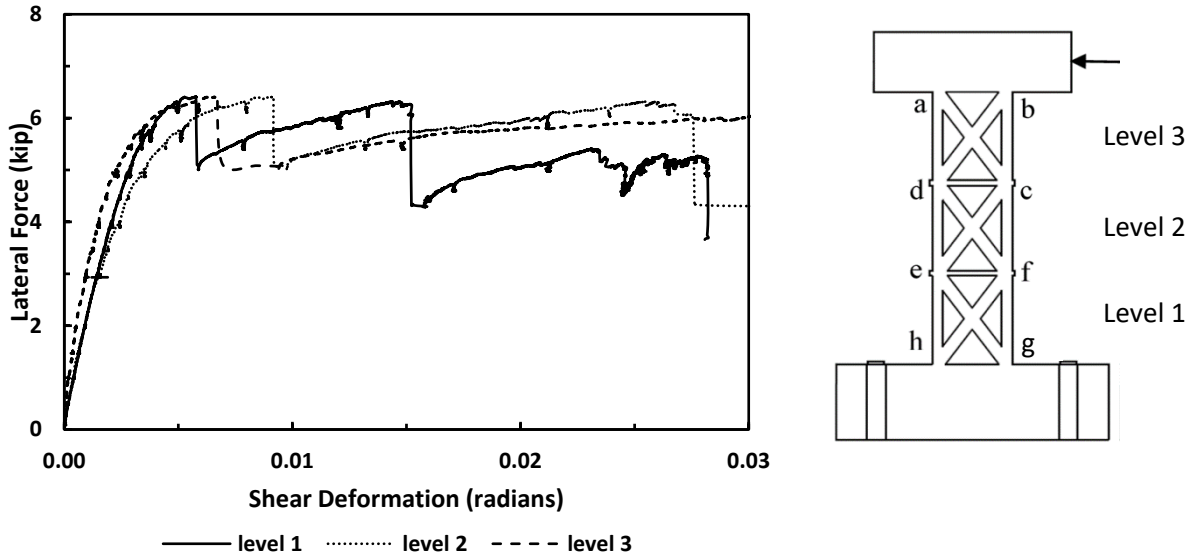

Figure A.21: Close-up of Fig. A.19 for shear deformation up to 0.03 rad

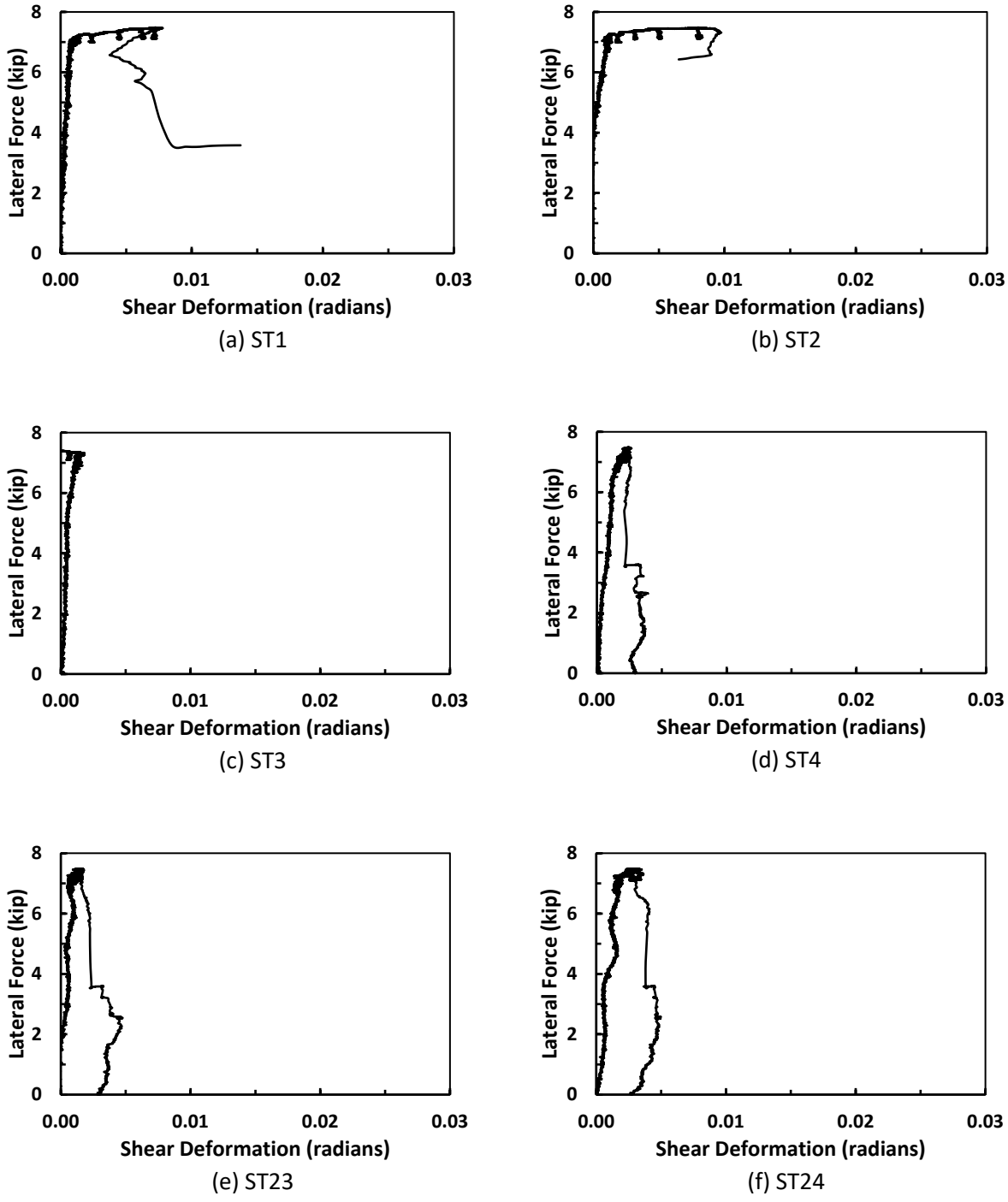

Figure A.22: Shear deformations in level 1 of control wall (1st column, compression face)

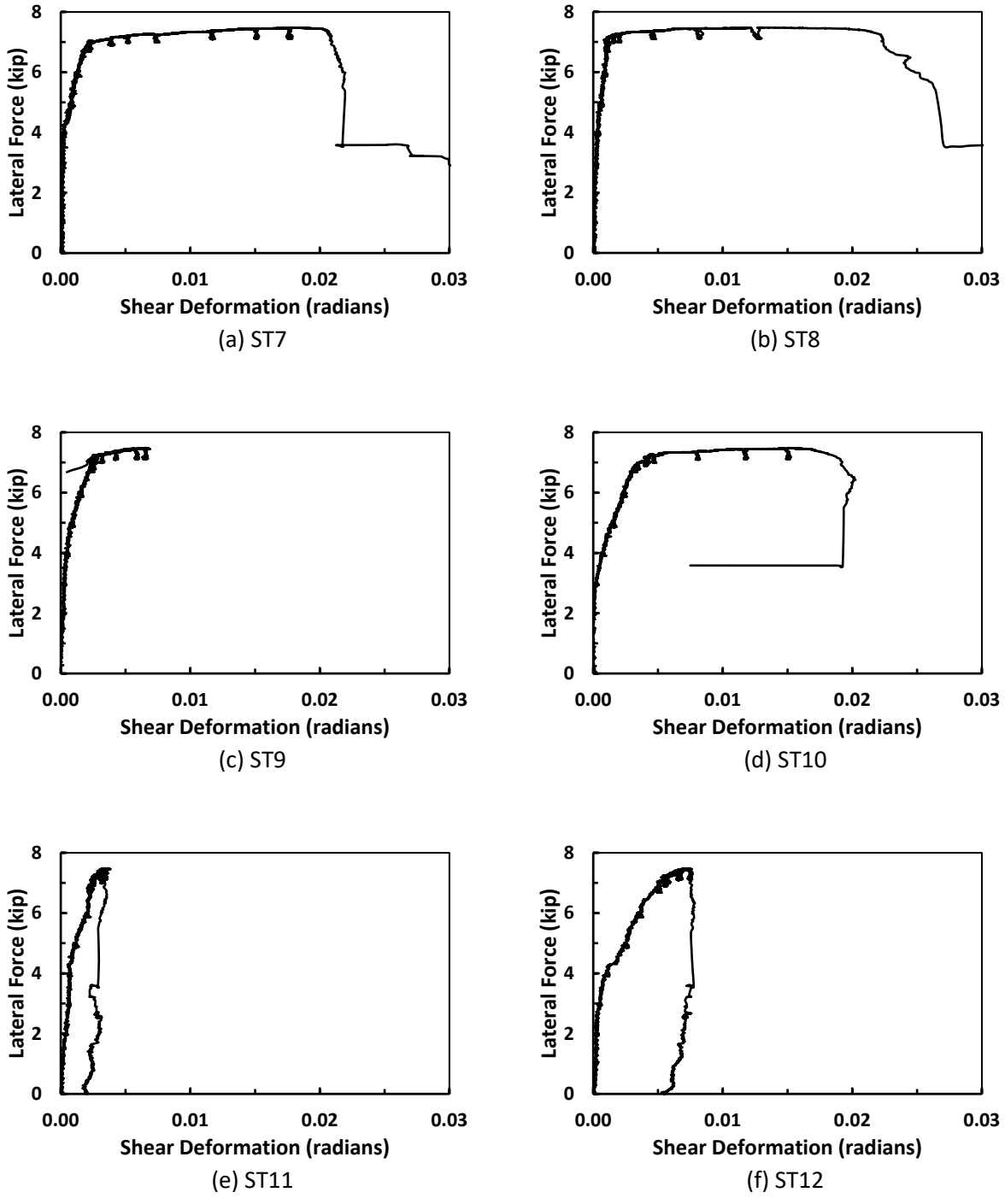

Figure A.23: Shear deformations in level 1 of control wall (2nd column)

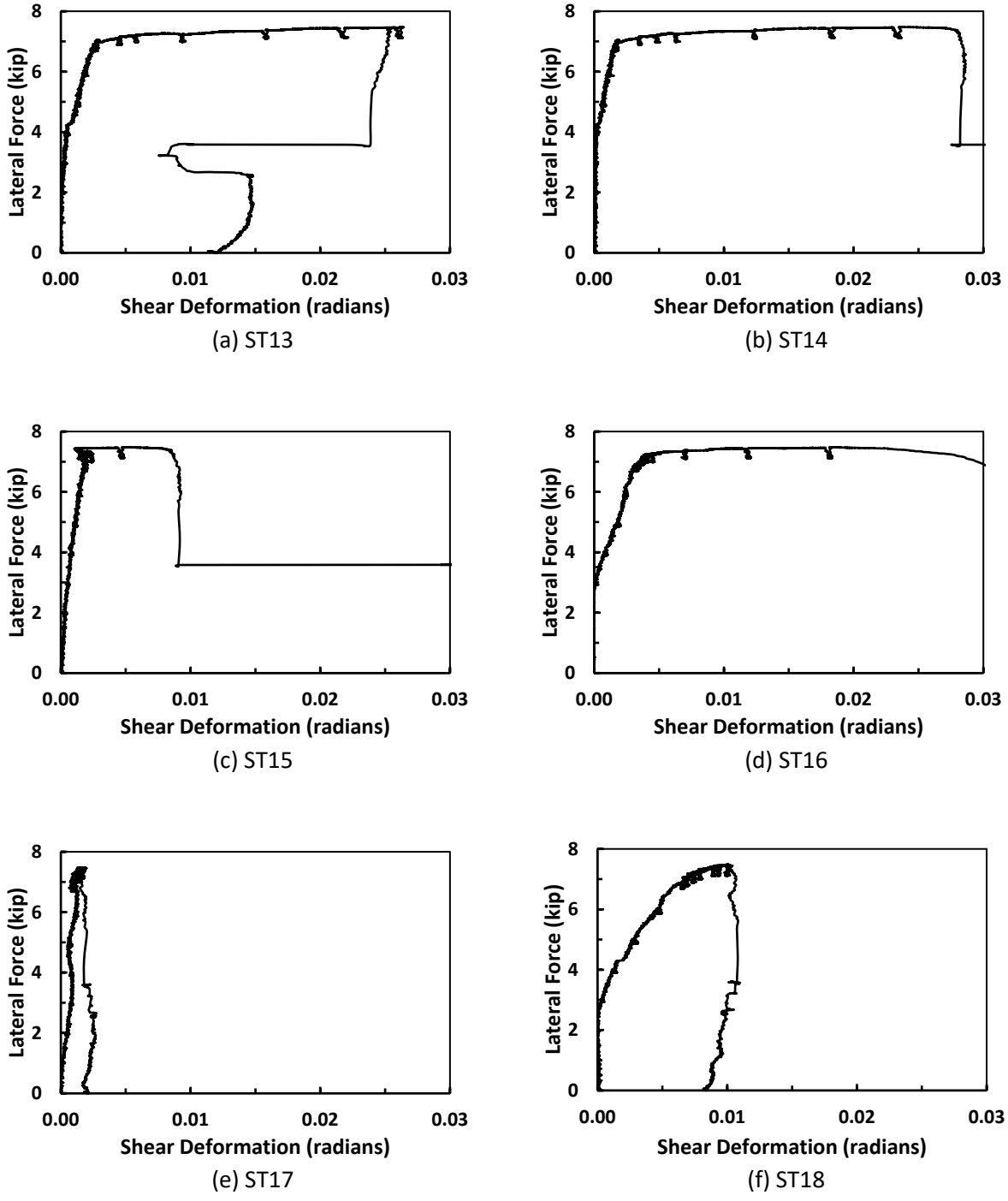

Figure A.24: Shear deformations in level 1 of control wall (3rd column)

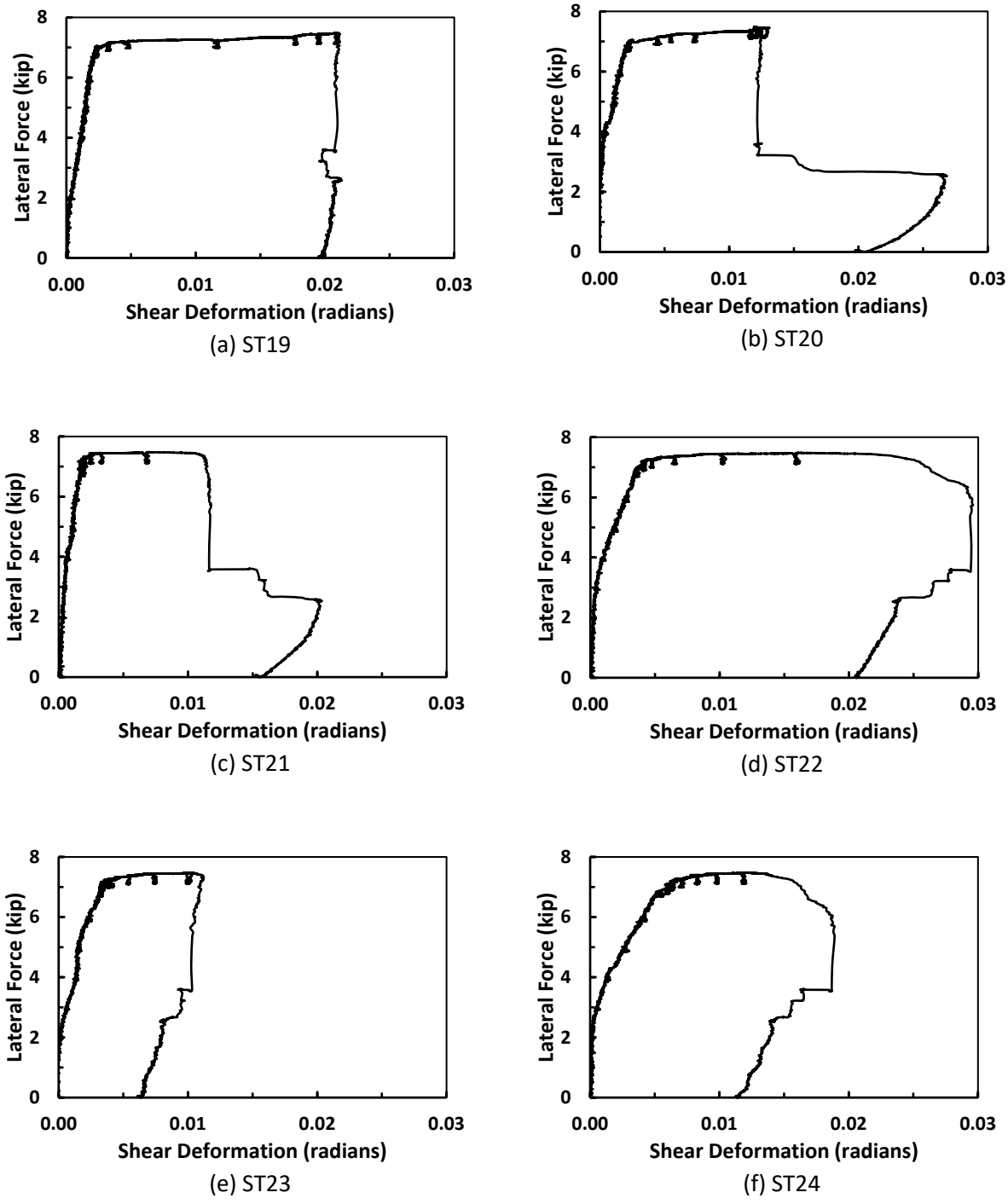

Figure A.25: Shear deformations in level 1 of control wall (4th column, tension face)

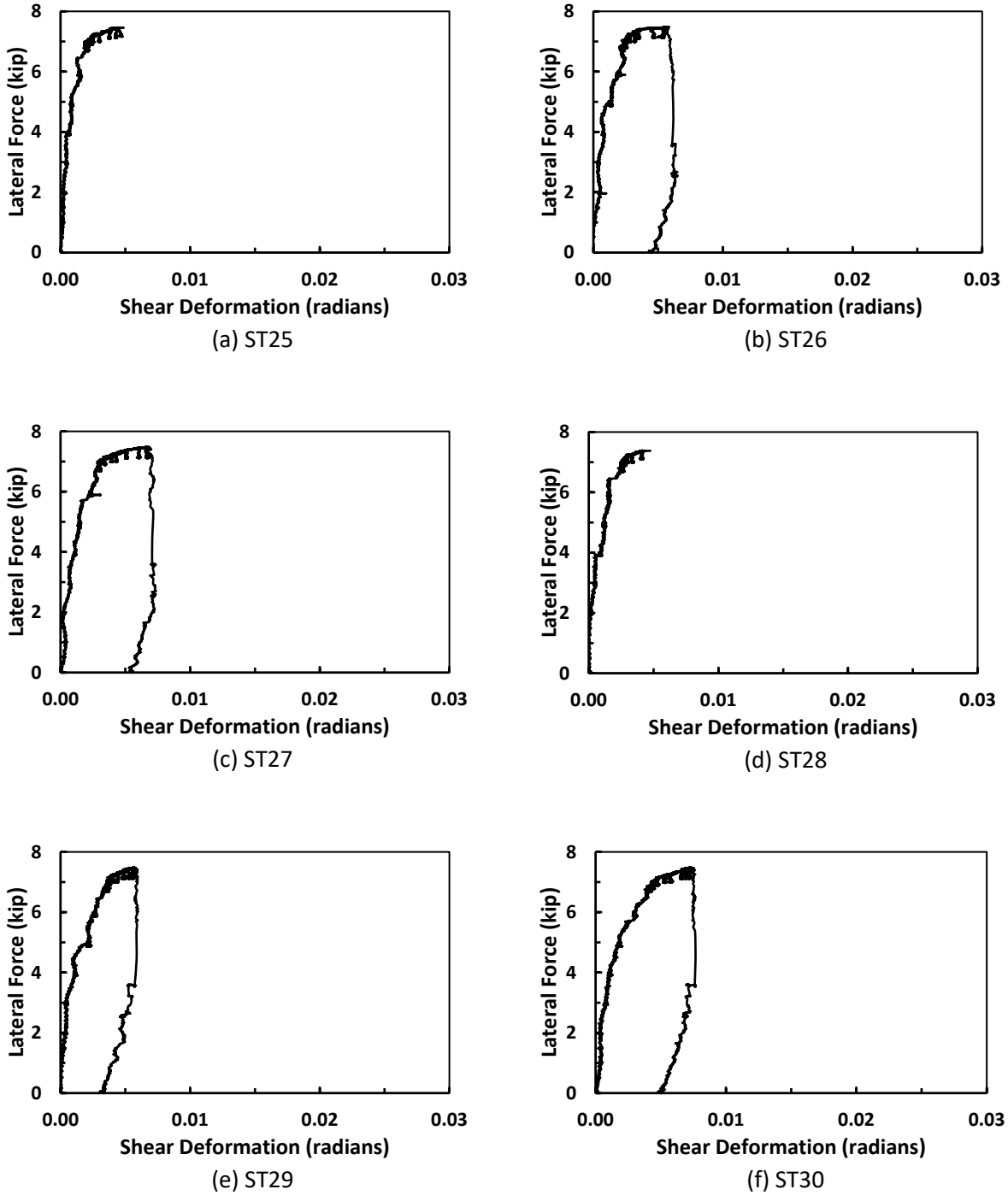

Figure A.26: Shear deformations in level 2 of control wall

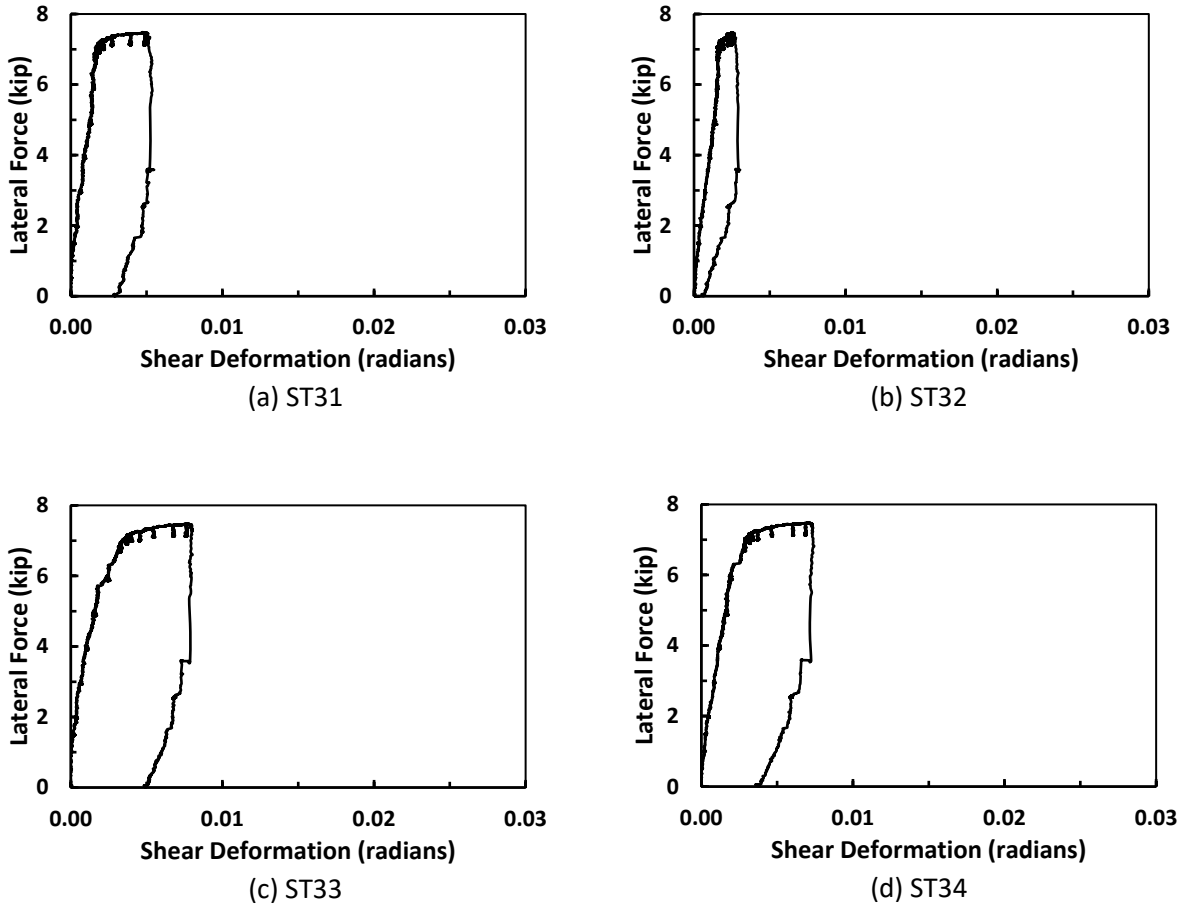

Figure A.27: Shear deformations in level 3 of control wall

In the following figures, the effects of considering smaller stations of optotrak markers versus larger are demonstrated. The local curves were obtained by first calculating shear deformation at every station within the region of interest (shown in figures to right). The next step involved taking an average of the shear deformations in the stations at same elevation (horizontally adjacent). This average value was multiplied by the height of the station. These values at every station level were added to obtain the total deformation, which was divided by the total height of the region under consideration. The values in x-axis represent drift resulting from shear deformations.

The global curves are the shear deformation calculated using four corner markers of the region.

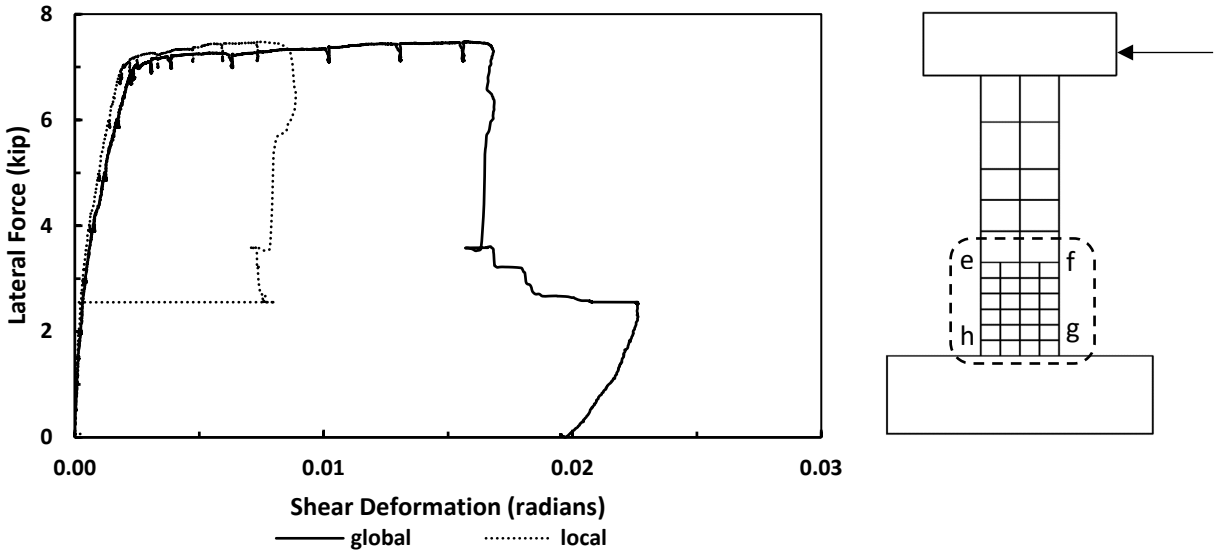

Figure A.28: Shear deformations in level 1 of control wall

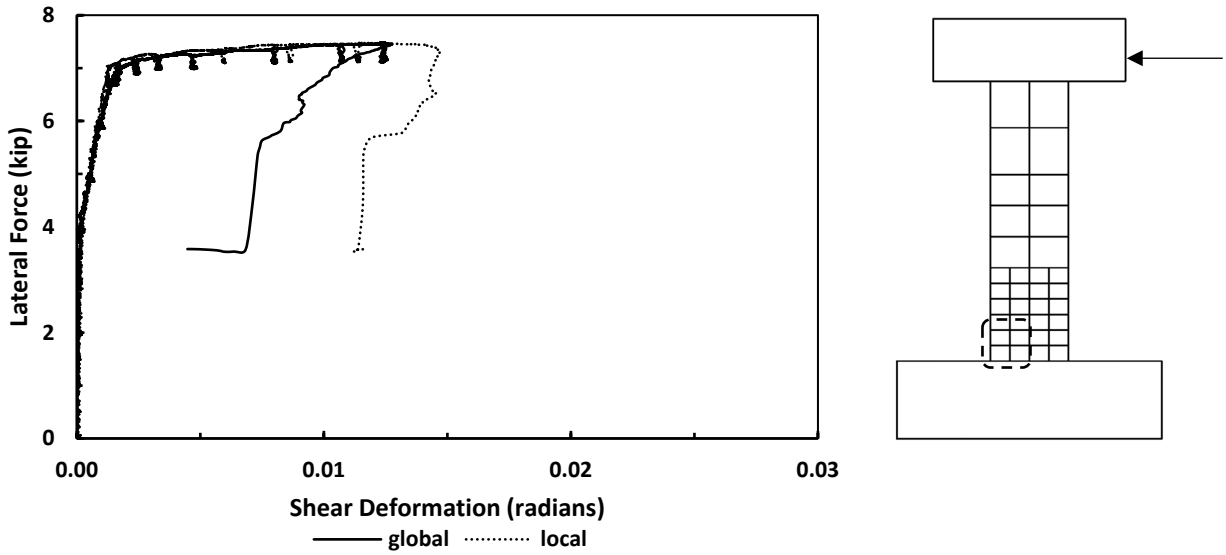

Figure A.29: Shear deformations in stations 1, 2, 7, 8 of control wall

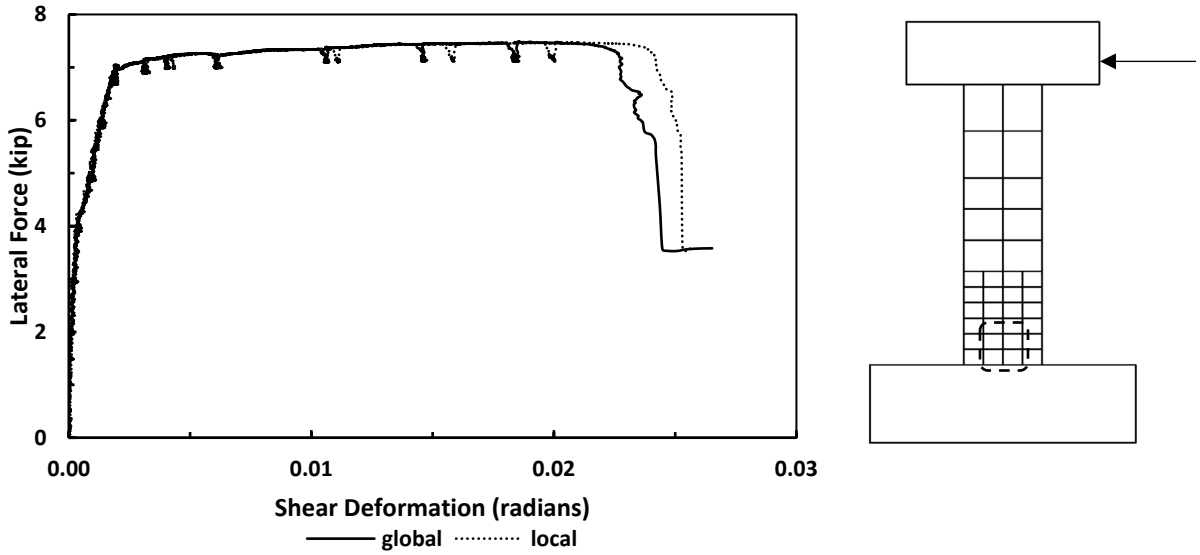

Figure A.30: Shear deformations in stations 7, 8, 13, 14 of control wall

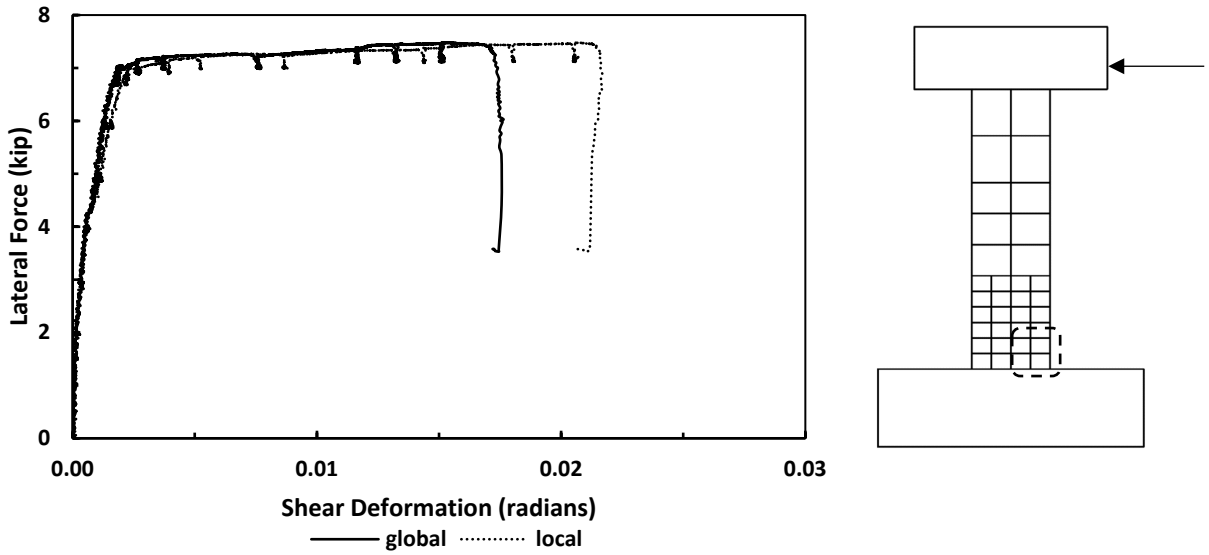

Figure A.31: Shear deformations in stations 13, 14, 19, 20 of control wall

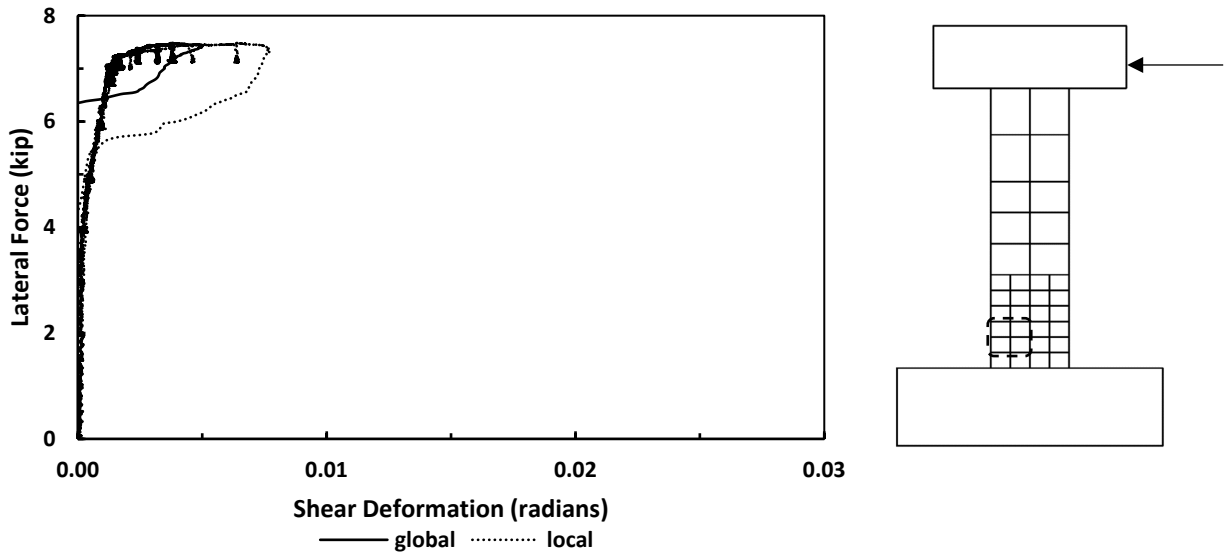

Figure A.32: Shear deformations in stations 2, 3, 8, 9 of control wall

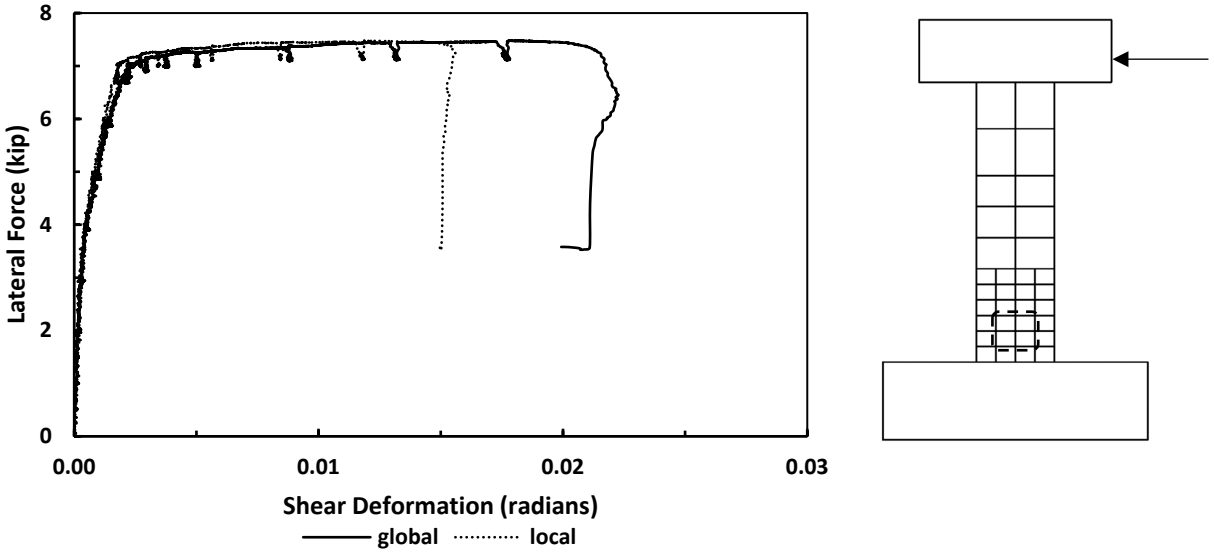

Figure A.33: Shear deformations in stations 8, 9, 14, 15 of control wall

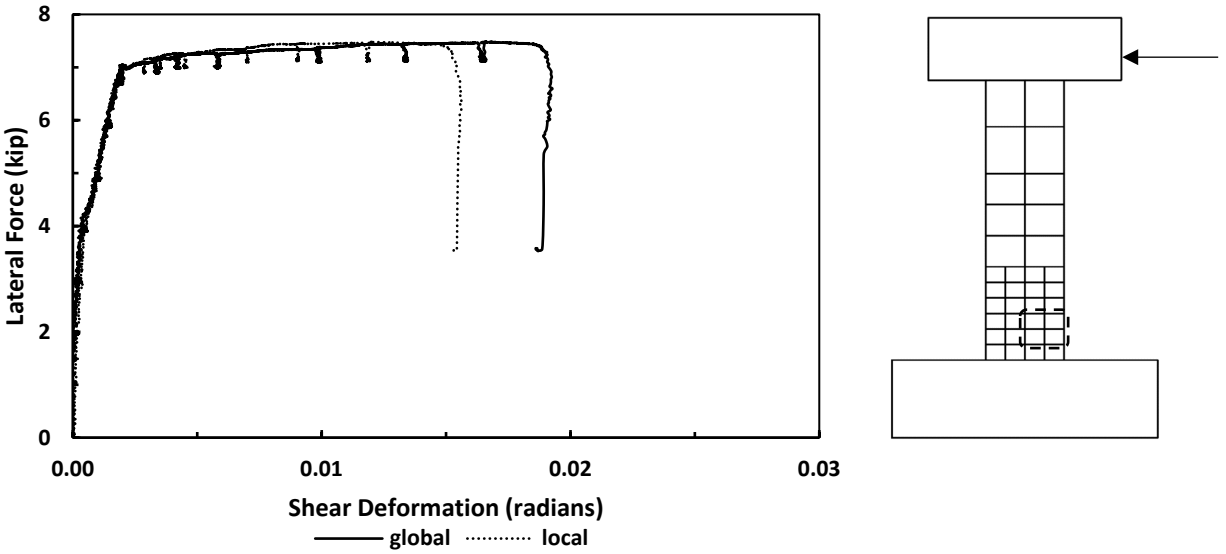

Figure A.34: Shear deformation in stations 14, 15, 20, 21 of control wall

In the following figures, the data labeled “local” represent the total shear deformation (in radians) within a level based on local station measurements. This is equal to the total wall drift resulting from shear deformations within a level. The “local” shear deformations were calculated by first calculating shear deformation at every station within level 1 (shown in the schematic to the right of the figures). The shear deformations calculated for horizontally adjacent stations at a single elevation were averaged and then multiplied by the average height of the stations. These were then summed for all rows of stations within level 1 and then divided by the total height of level 1.

The data labeled “coarse” represent the total shear deformations (in radians) within a level based on a coarser grid of markers (simulated by redefining a station as a group of four stations). This was calculated using similar procedure as described above.

The data labeled “global” represent the total shear deformations (in radians) within a level based only on the four corners of the level. For level 1, markers e-f-g-h were used to calculate the “global” shear deformation.

Differences between the three results show the important effect of grid size on calculated shear deformations. The “local” and “coarse” grids produced calculated shear deformations that were much less than calculated using the “global” approach.

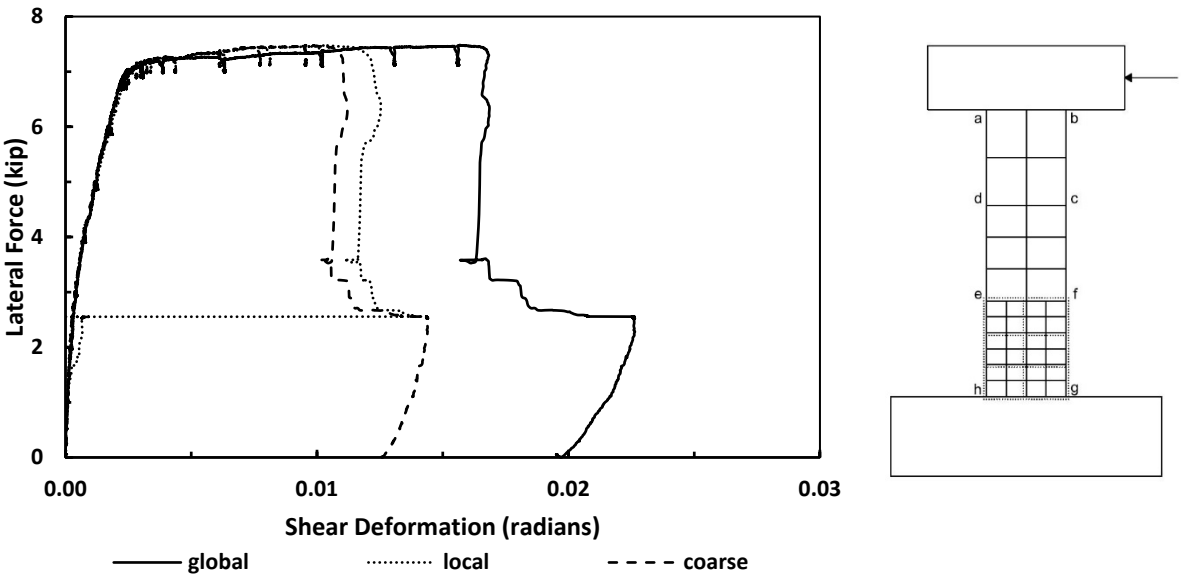

Figure A.35: Shear deformation in level 1 of control wall

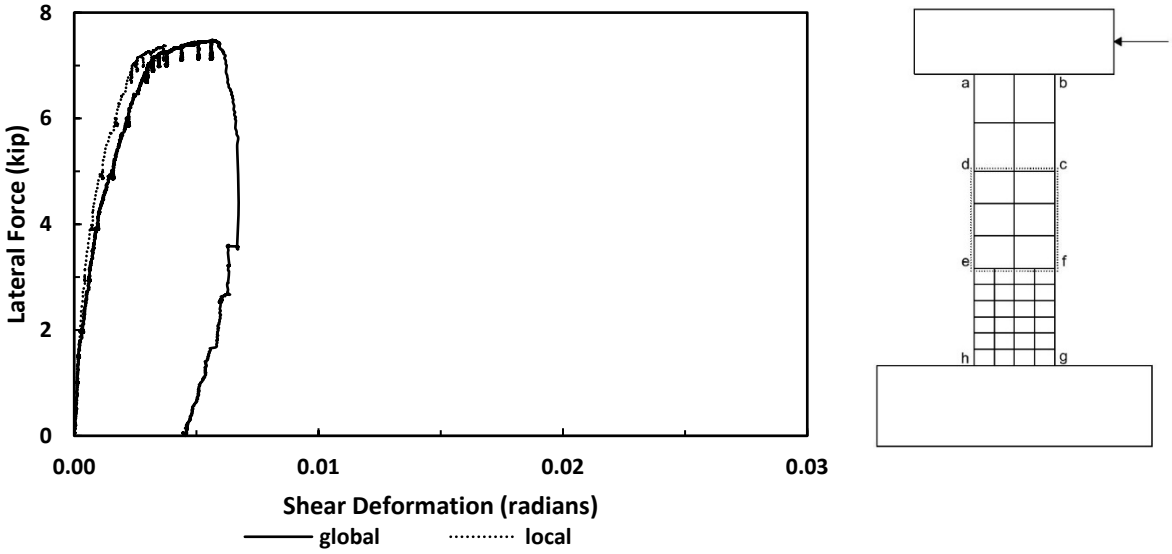

Figure A.36: Shear deformation in level 2 of control wall

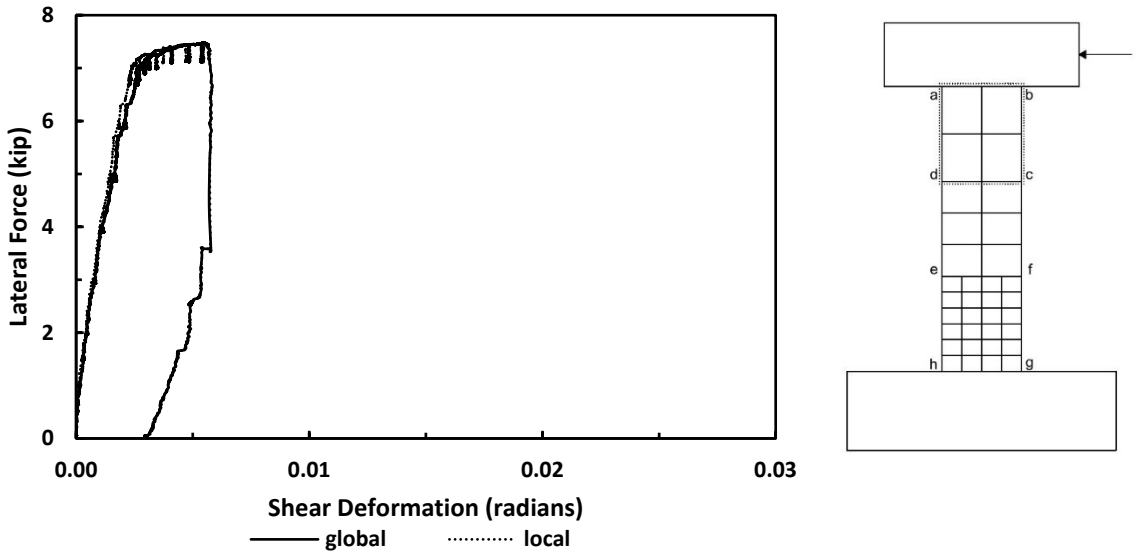

Figure A.37: Shear deformation in level 3 of control wall

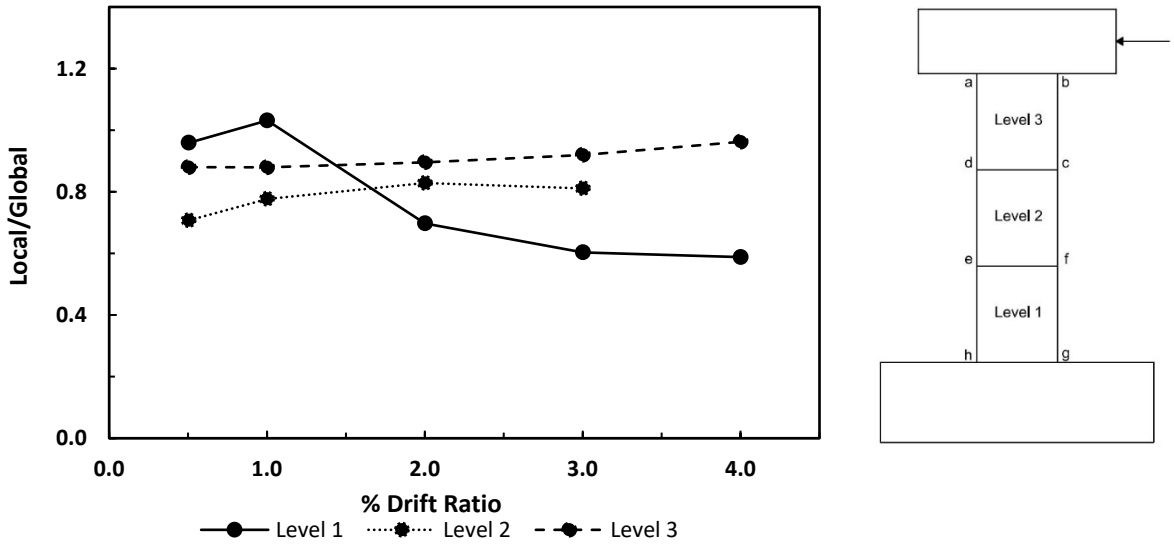

Figure A.38: Ratio of local to global shear deformations vs. drift ratio

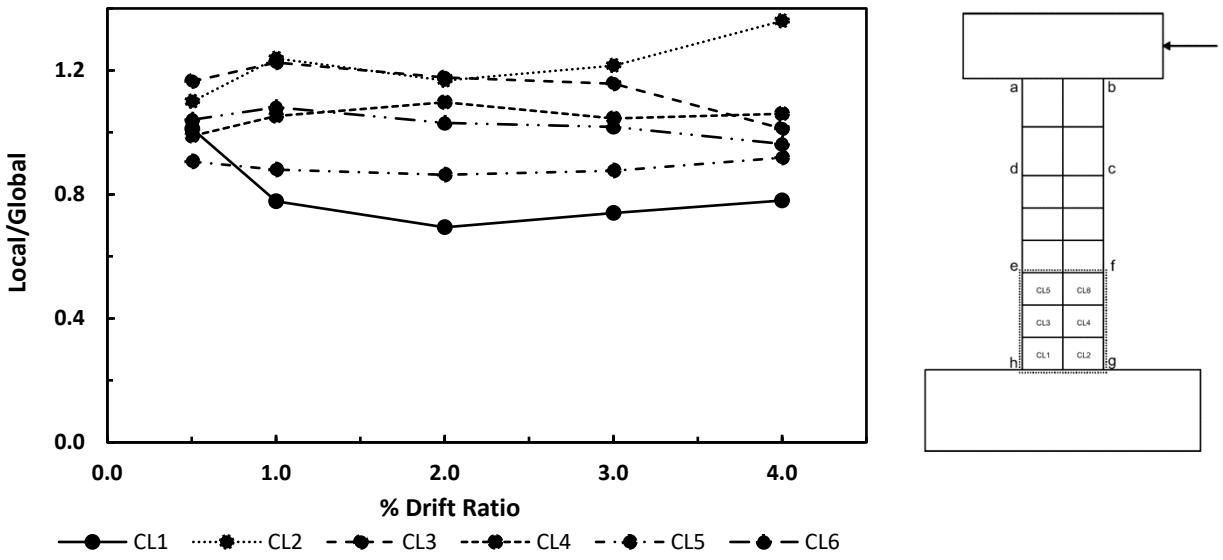

Figure A.39: Ratio of local to global shear deformations vs. drift ratio in level 1

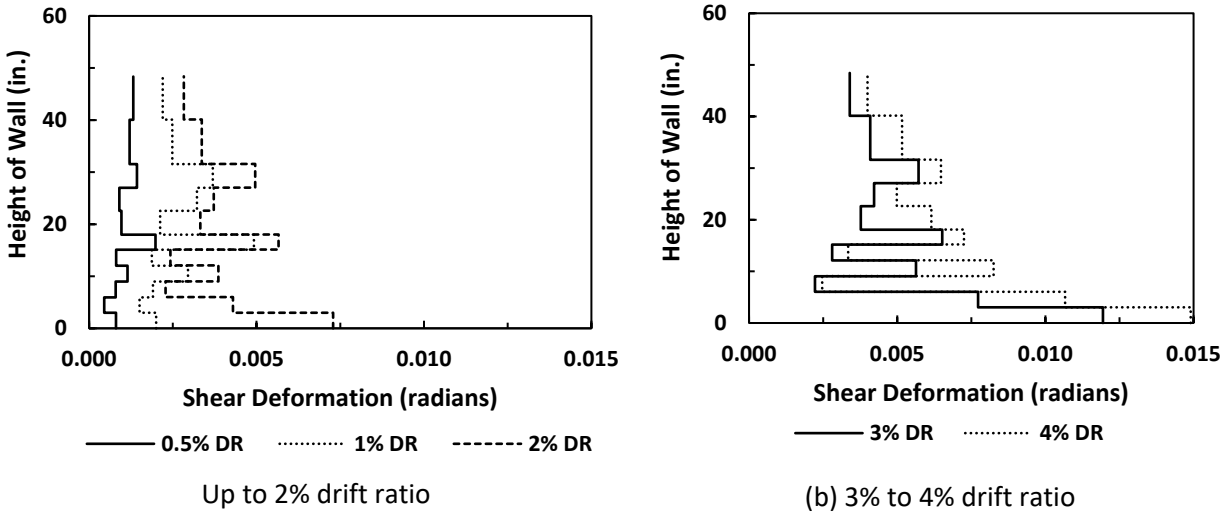

Figure A.40: Shear deformations along the height of control wall

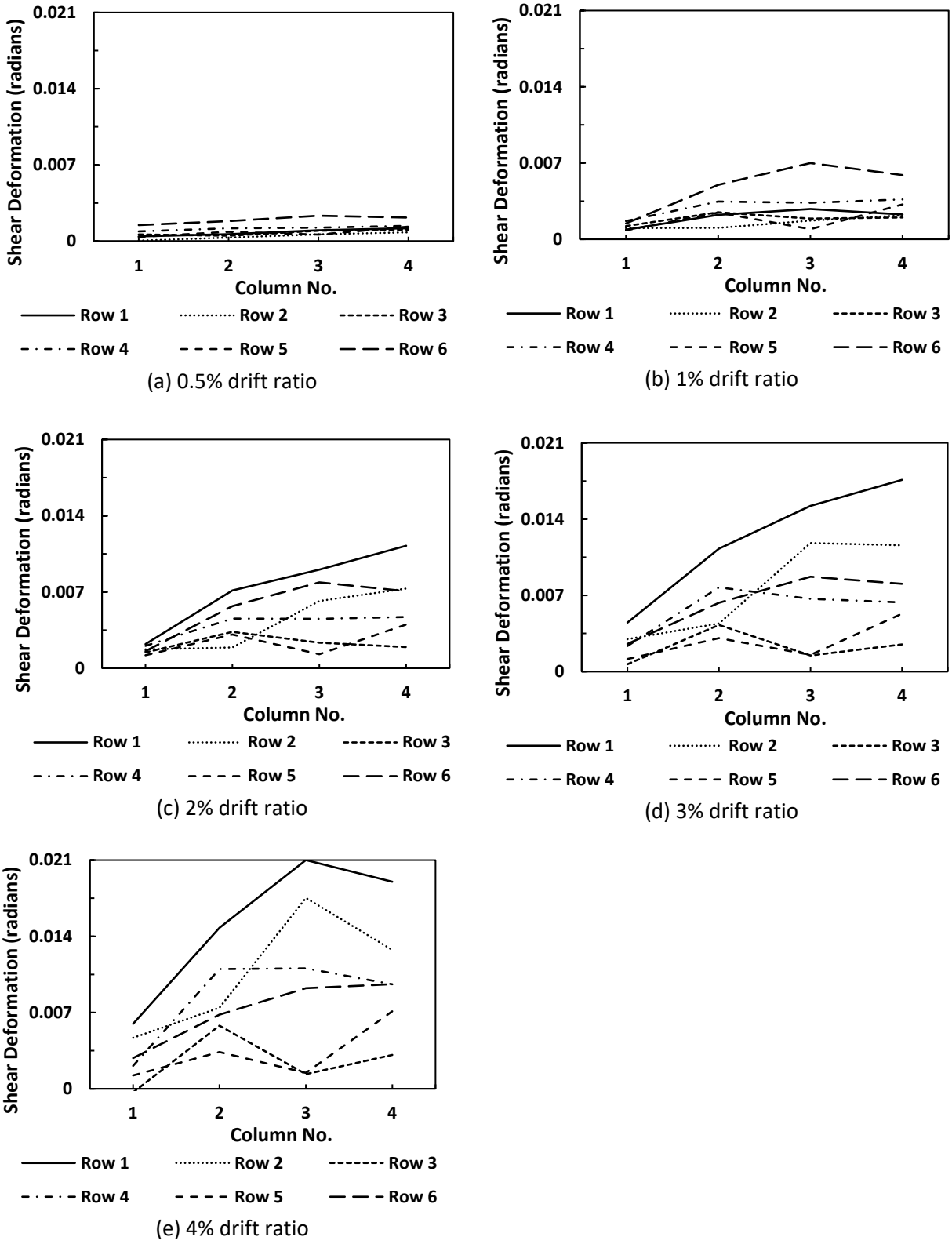

Figure A.41: Shear deformations in level 1 of control wall

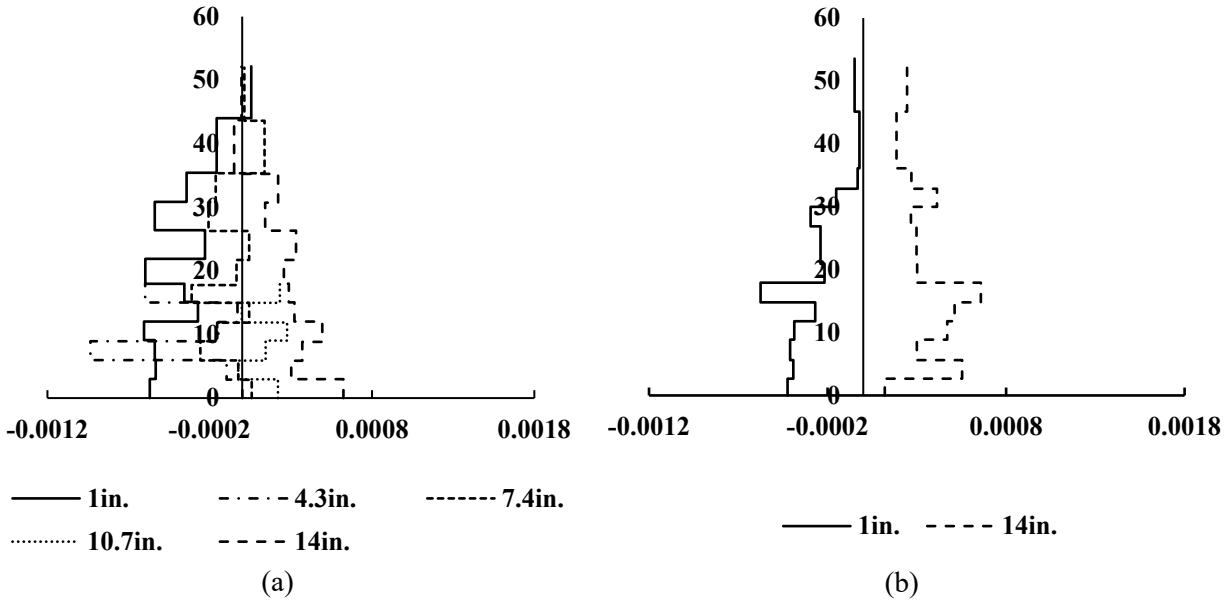

Figure A.42: Axial strains along height of the wall at 0.25% drift ratio in (a) control and (b) optimized walls

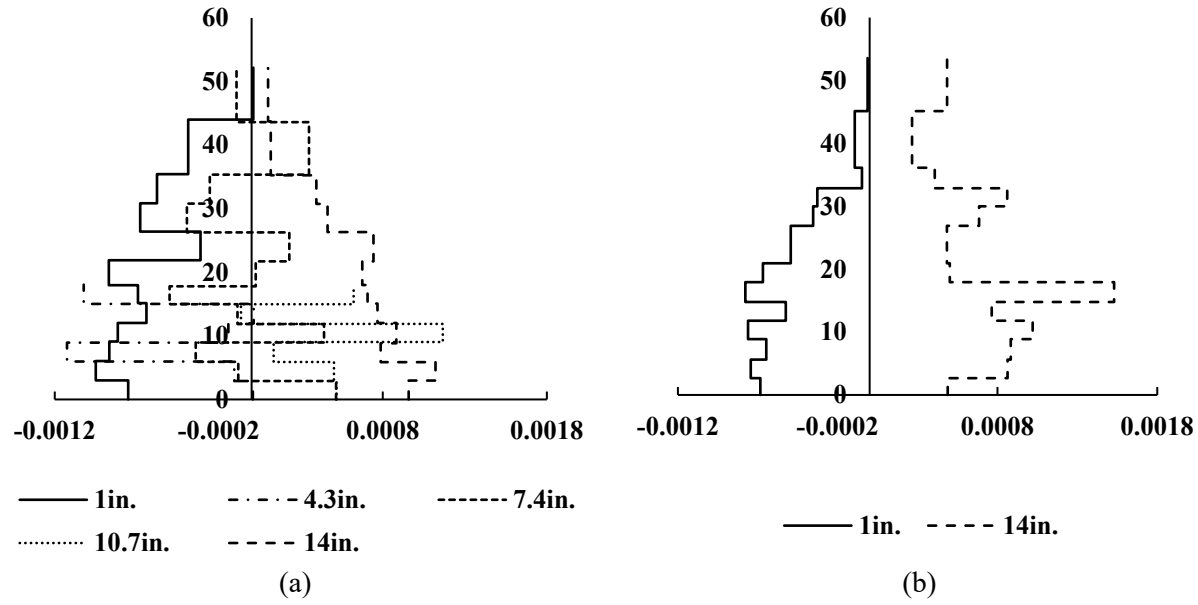

Figure A.43: Axial strains along height of the wall at 0.5% drift ratio in (a) control and (b) optimized walls

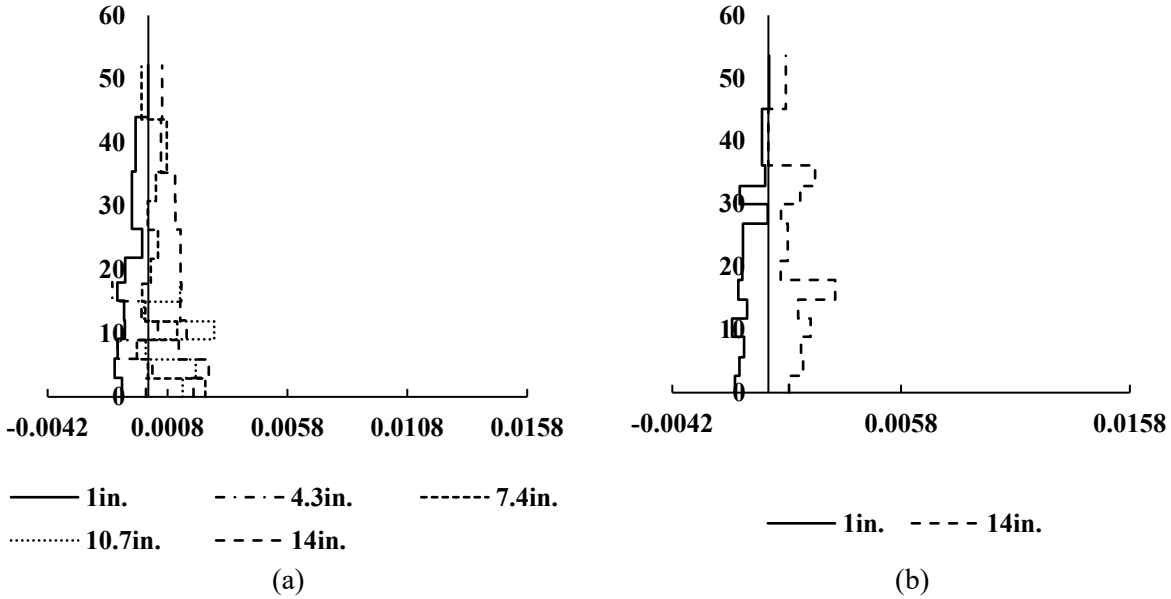

Figure A.44: Axial strains along height of the wall at 1% drift ratio in (a) control and (b) optimized walls

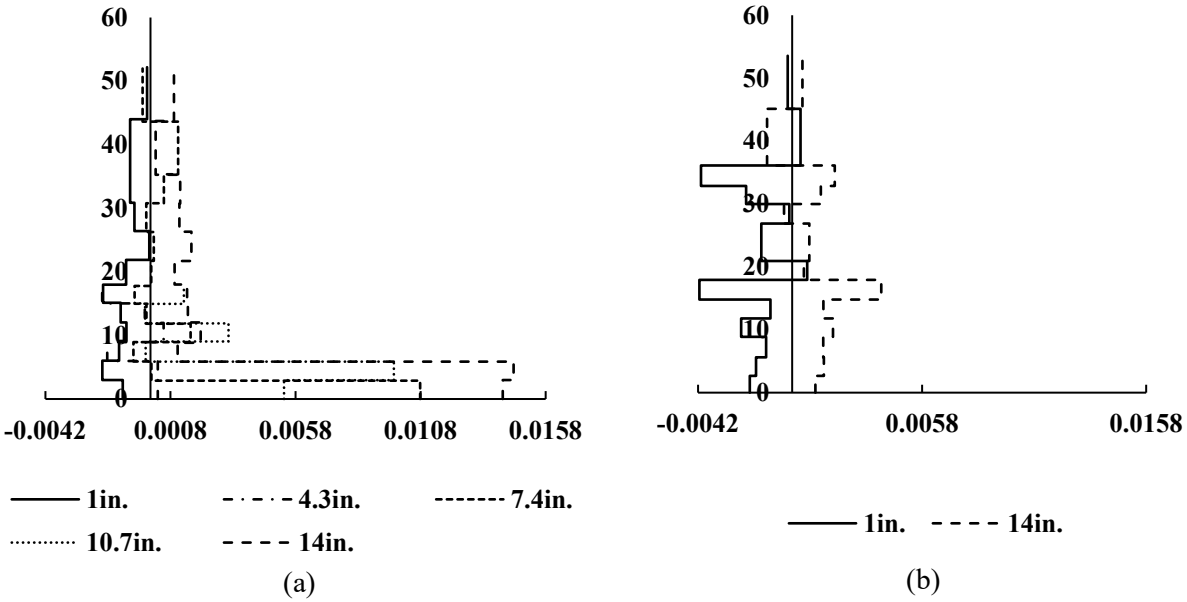

Figure A.45: Axial strains along height of the wall at 2% drift ratio in (a) control and (b) optimized walls

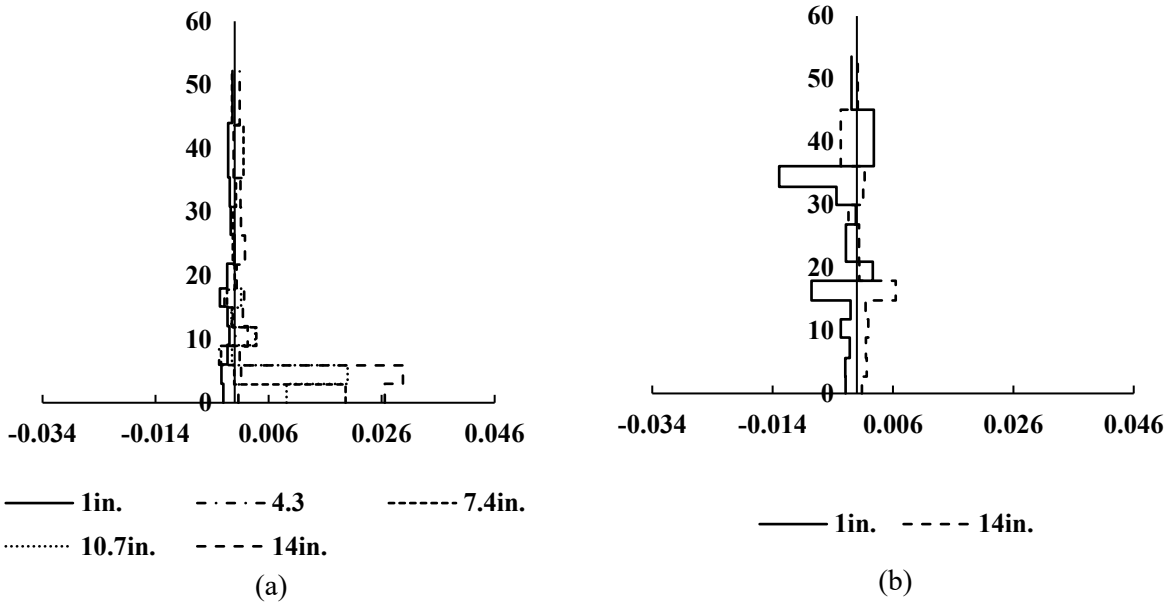

Figure A.46: Axial strains along height of the wall at 3% drift ratio in (a) control and (b) optimized walls

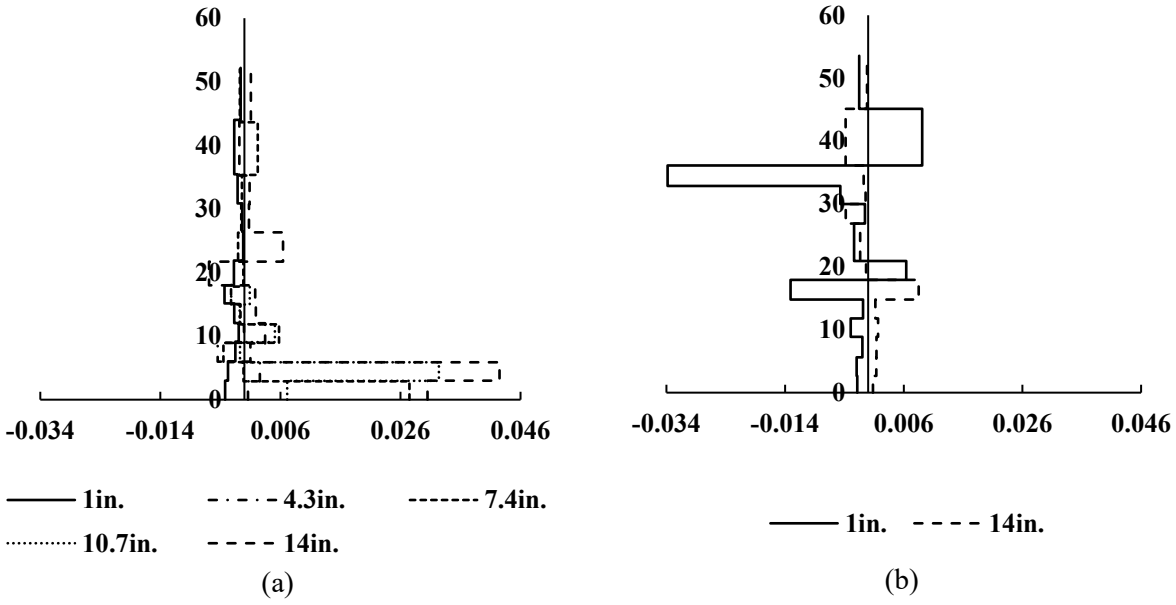

Figure A.47: Axial strains along height of the wall at 4% drift ratio in (a) control and (b) optimized walls

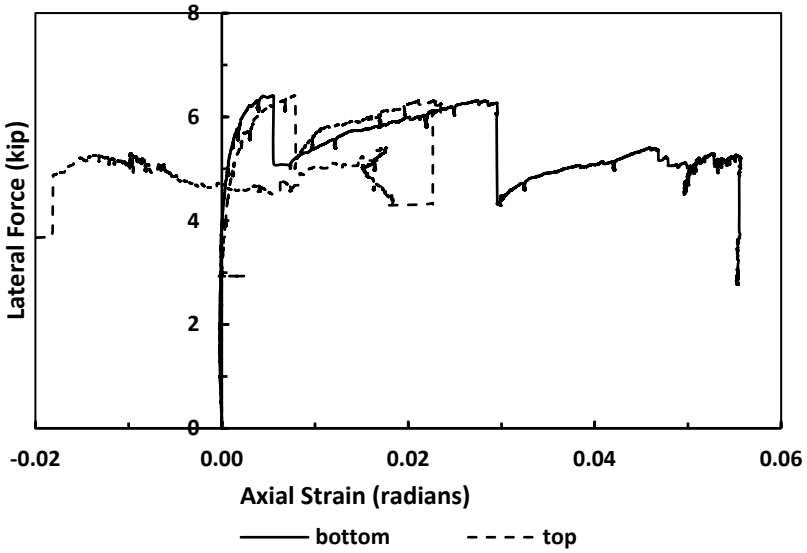

Figure A.48: Axial deformation in slabs of optimized wall

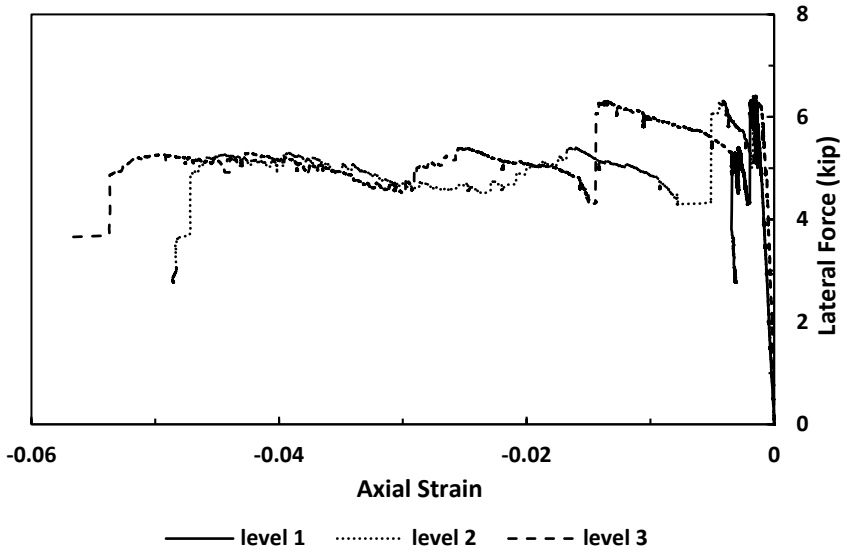

Figure A.49: Axial (compression) strains in inclined struts of optimized wall

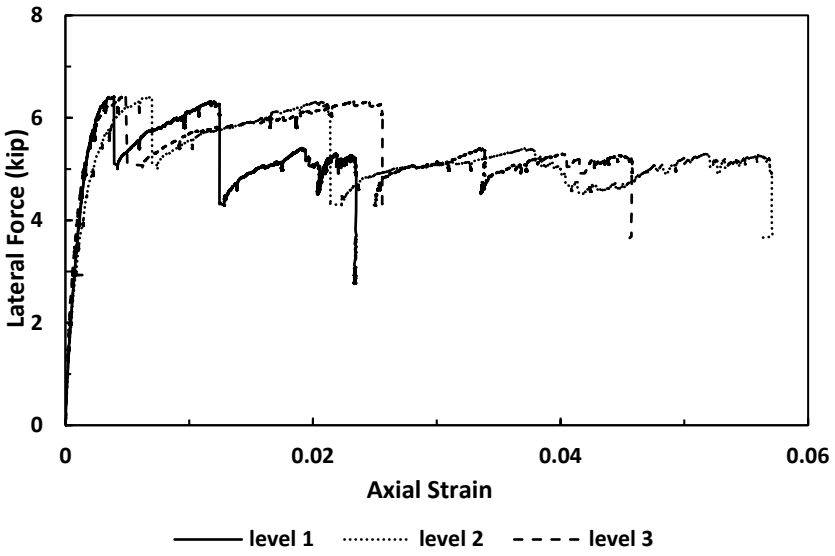

Figure A.50: Axial (tension) strains in inclined ties of optimized wall

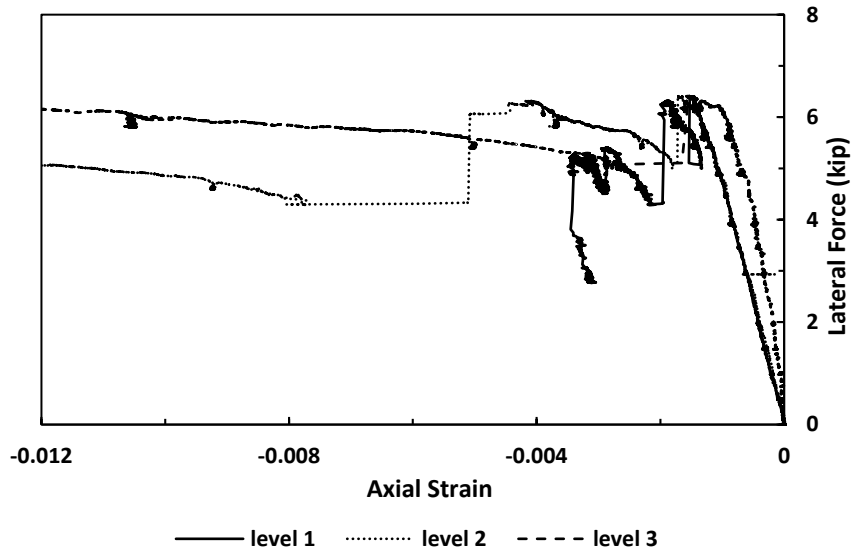

Figure A.51: Close-up of Fig. A.53 for axial (compression) strains up to -0.012

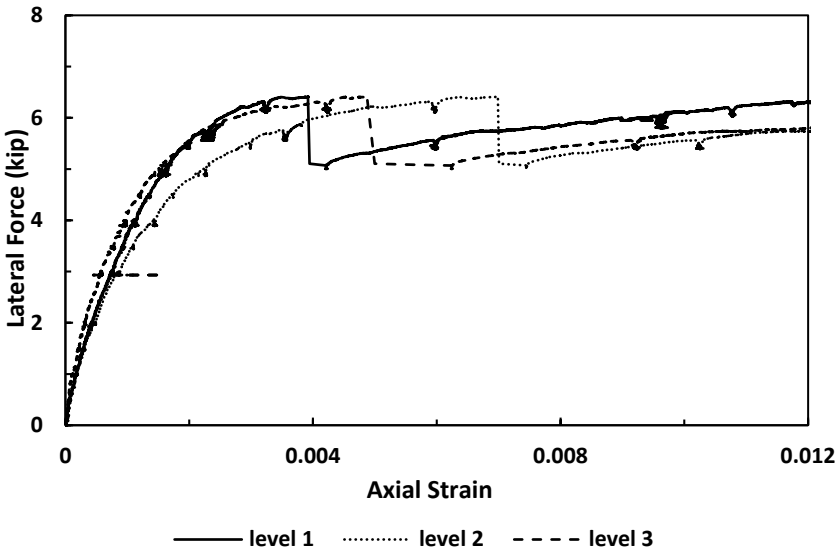

Figure A.52: Close-up of Fig. A.54 for axial (tension) strains up to 0.012

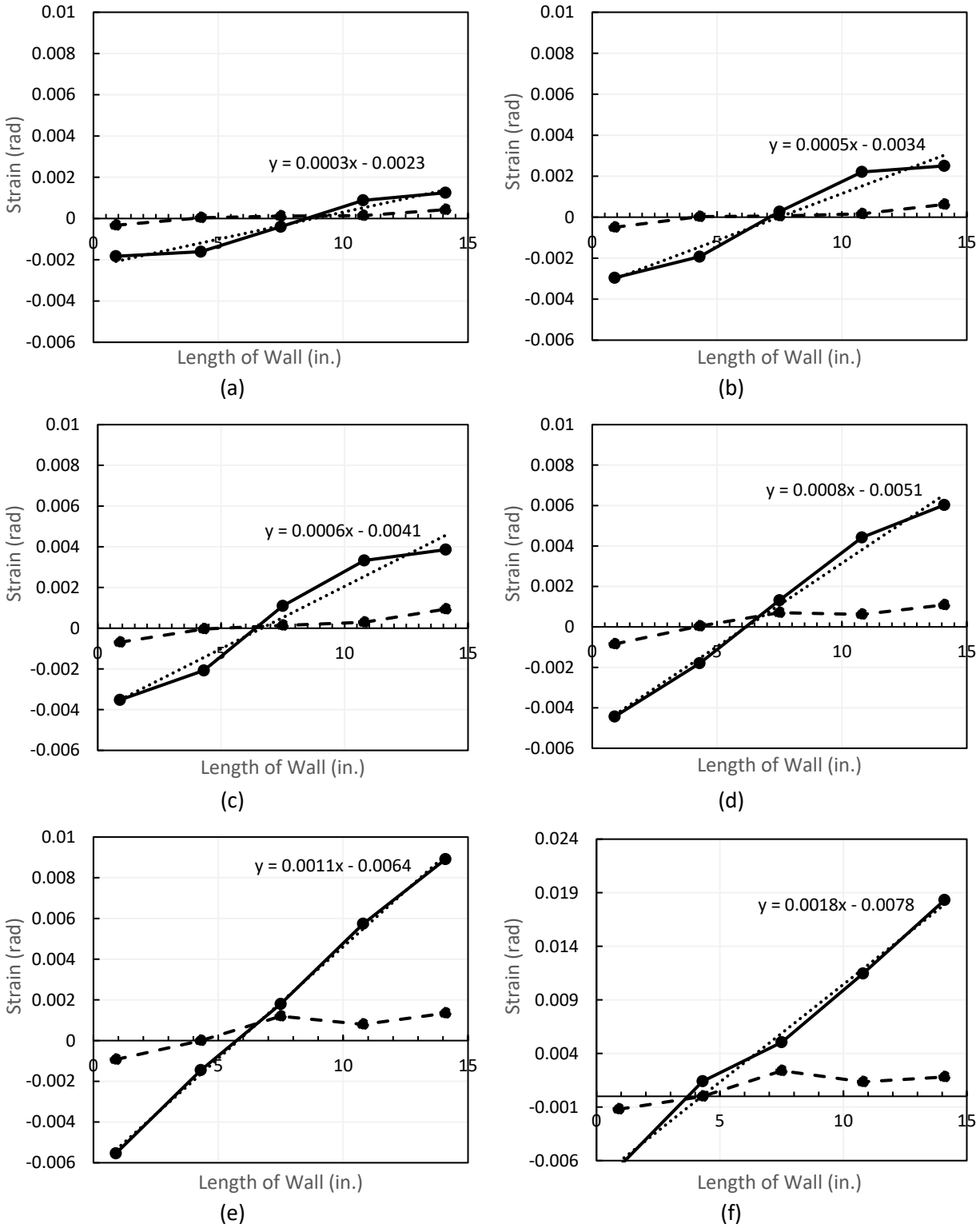

Figure A.53: Strains along the base of the control wall at (a) 0.16%, (b) 0.27%, (c) 0.41%, (d) 0.57%, (e) 0.74%, and (f) 1.0%. The solid lines represent change in distance divided by 1 in., while the dashed lines represent change in distance divided by 4 in.

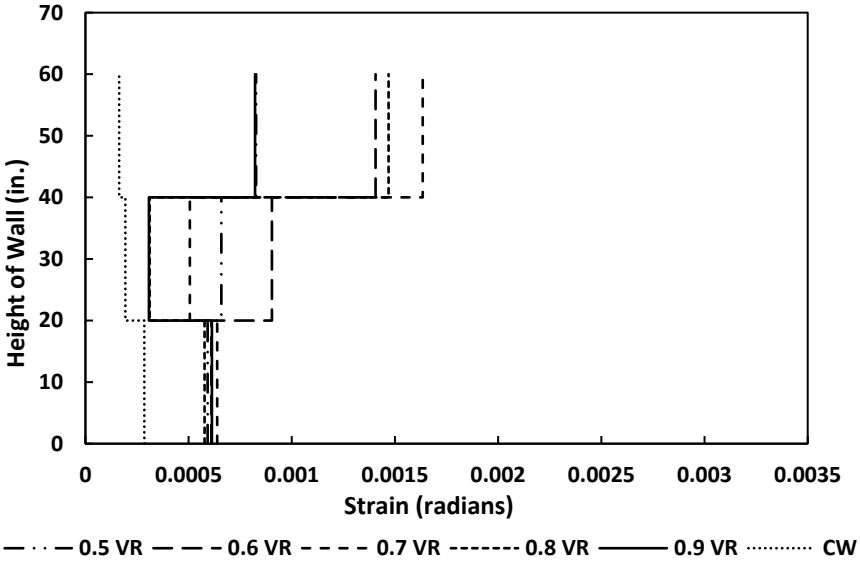

Figure A.54: Shear deformation along the height of the FE model for different volume ratios at 6 kips lateral force for the similar strength case

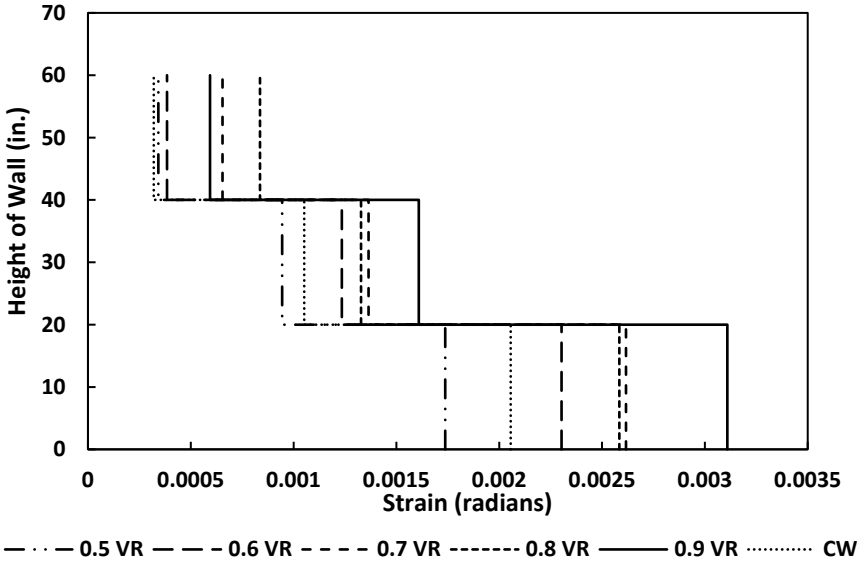

Figure A.55: Flexural rotation along the height of the FE model for different volume ratios at 6 kips lateral force for the similar strength case

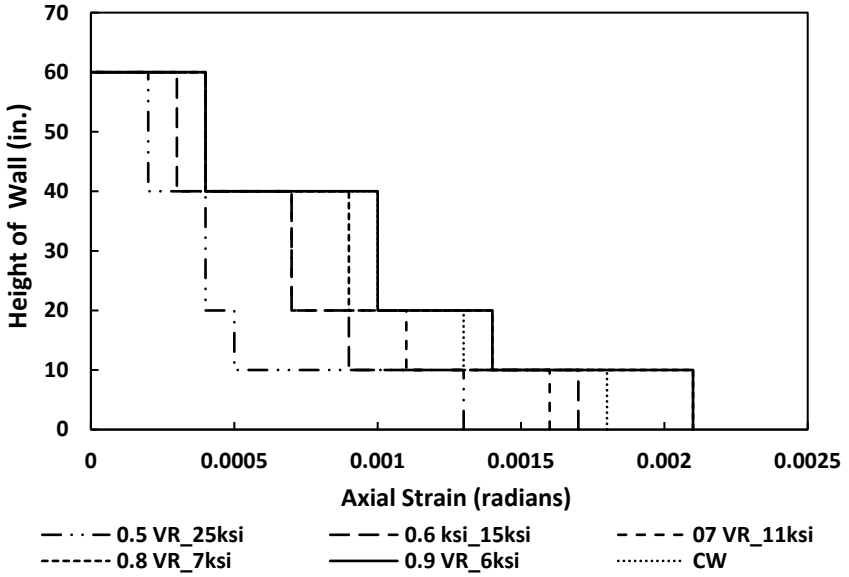

Figure A.56: Maximum principal (tensile) strain in longitudinal reinforcing bars along the height of the FE model for different volume ratios at 6 kips lateral force for the similar strength case

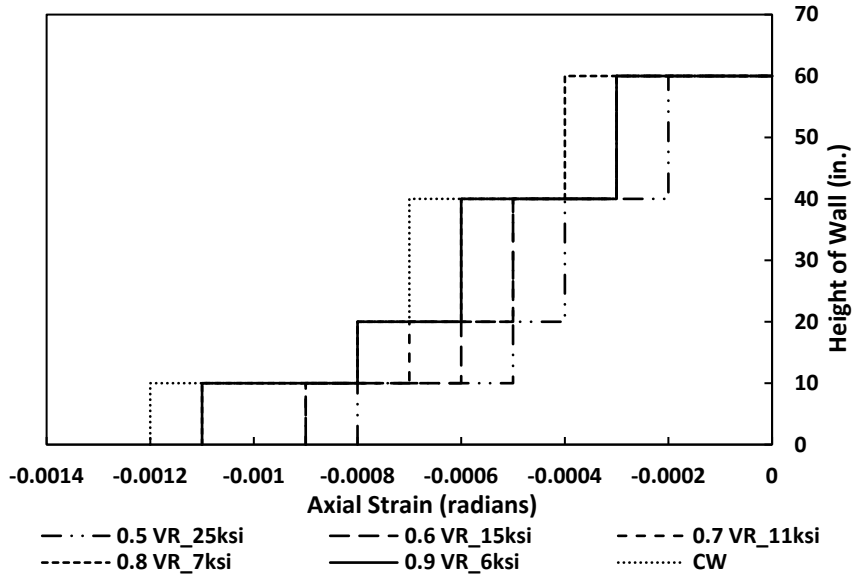

Figure A.57: Minimum principal (compression) strain in longitudinal reinforcing bars along the height of the FE model for different volume ratios at 6 kips lateral force for the similar strength case

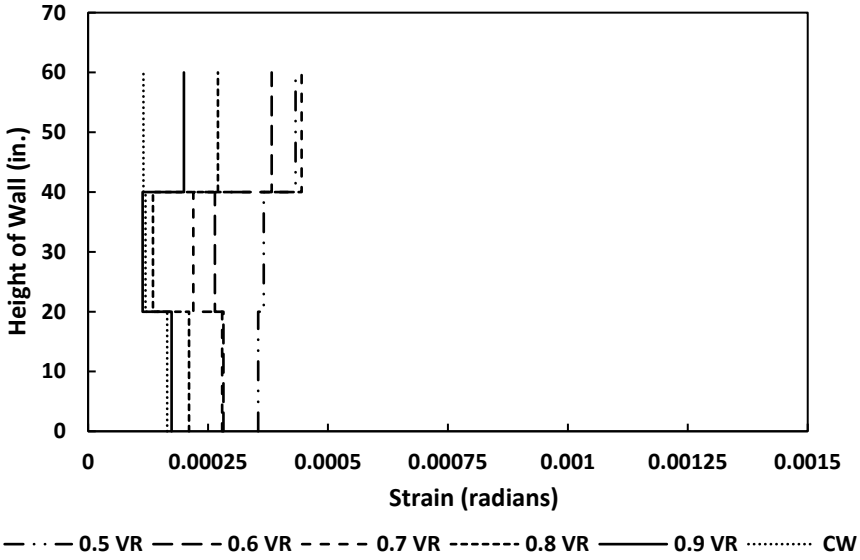

Figure A.58: Shear deformation along the height of the FE model for different volume ratios at 3 kips lateral force for the similar stiffness case

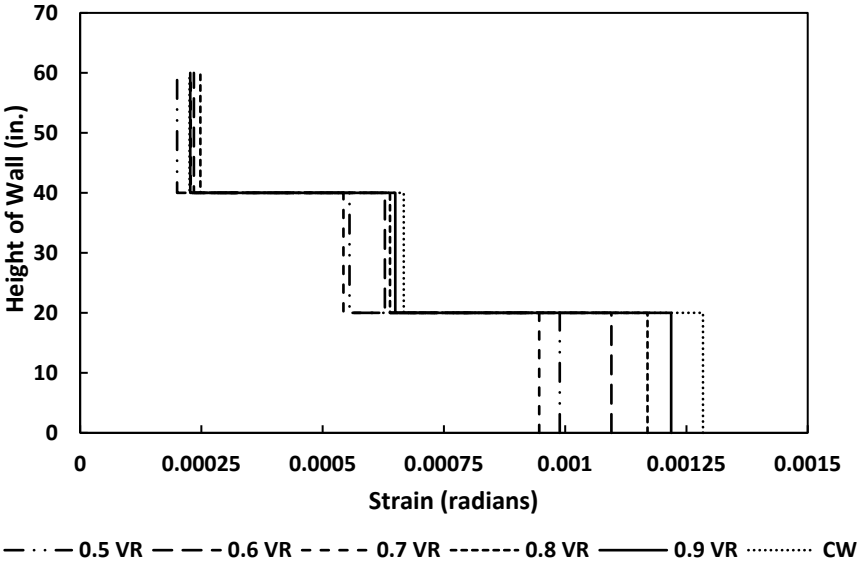

Figure A.59: Shear deformation along the height of the FE model for different volume ratios at 6 kips lateral force for the similar strength case

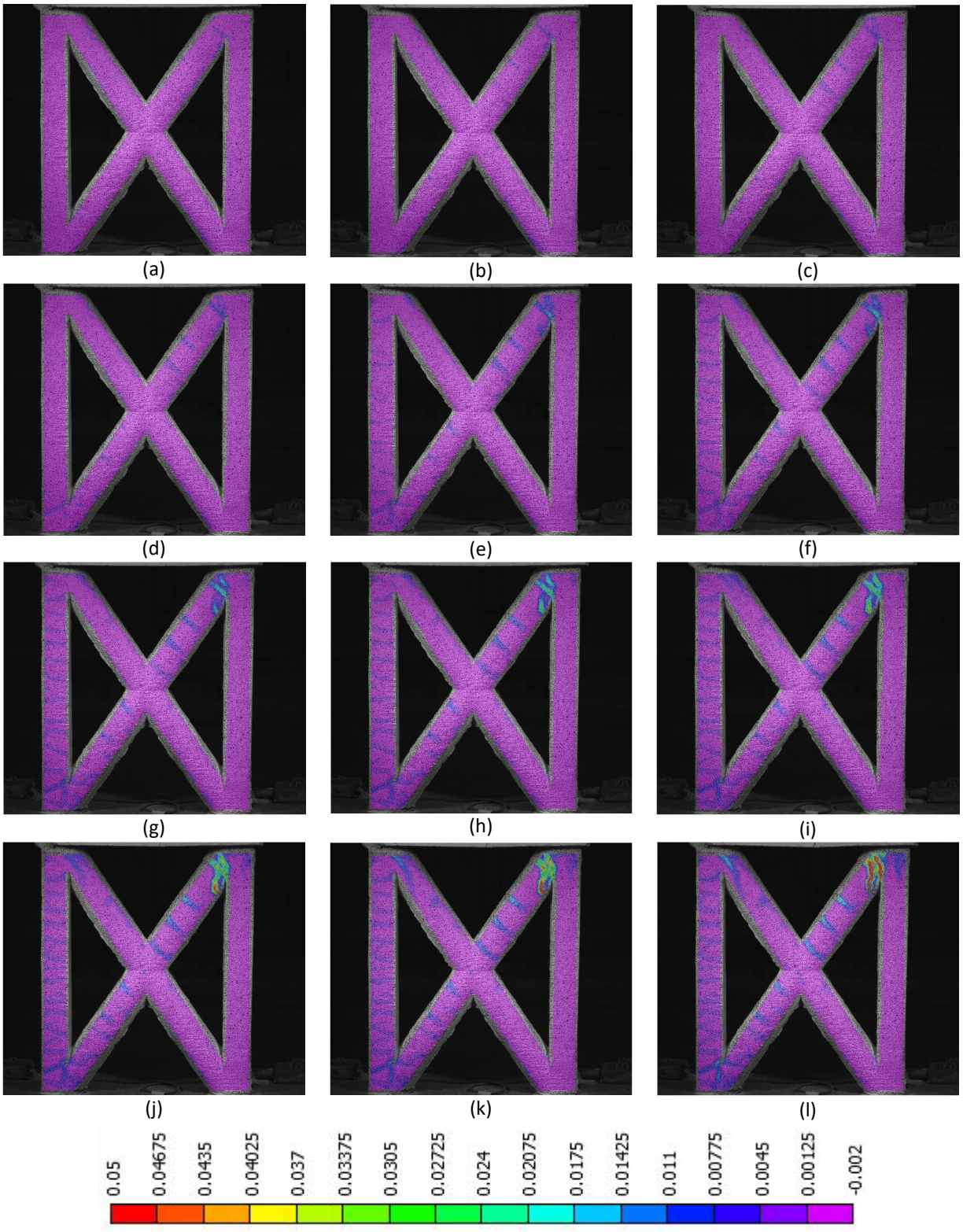

Figure A.60: Damage progression (results from DIC) in optimized wall specimen (up to drift ratio 1.5%)

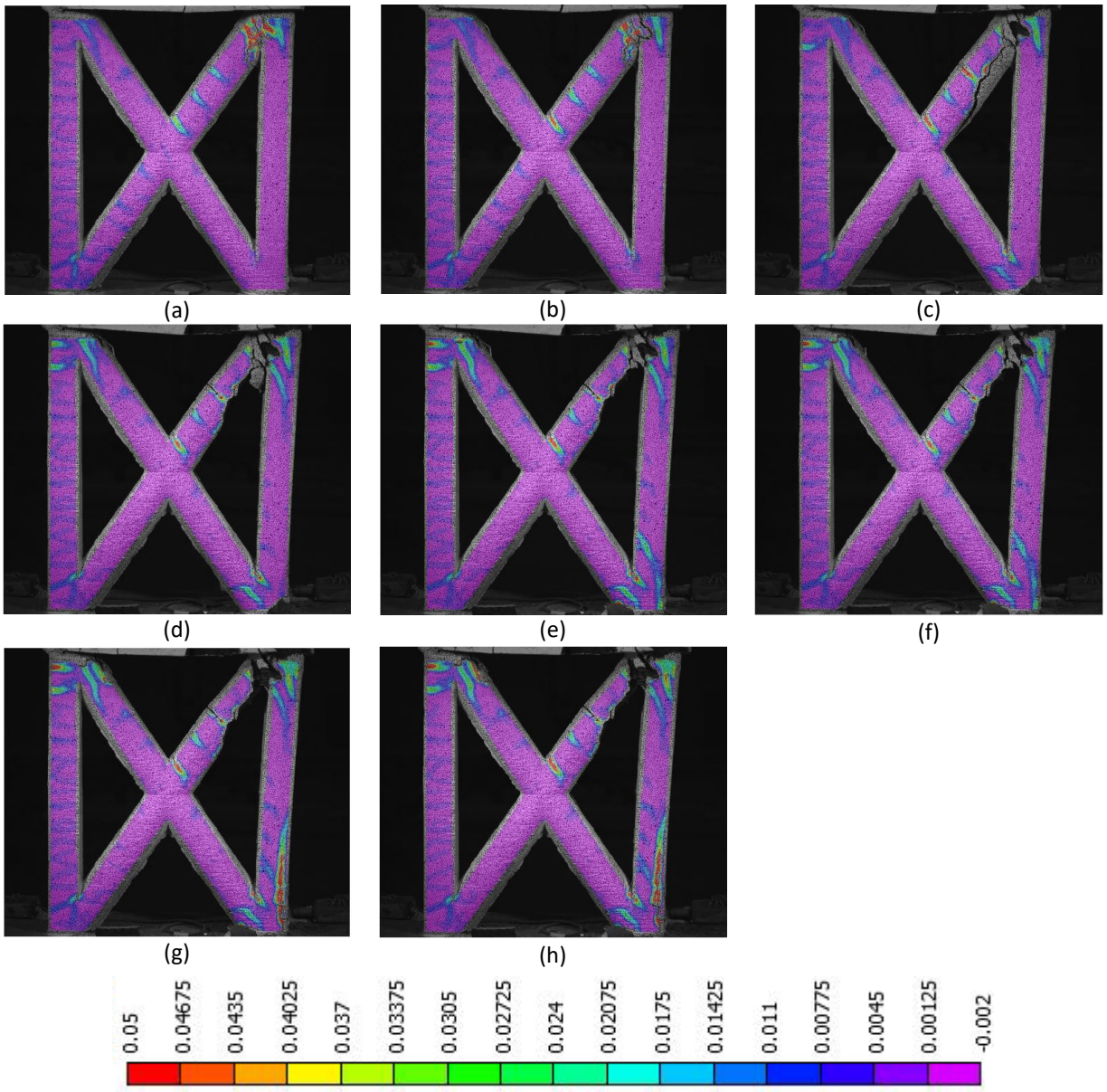

Figure A.61: Damage progression (results from DIC) in optimized wall specimen (1.5% drift ratio to failure)

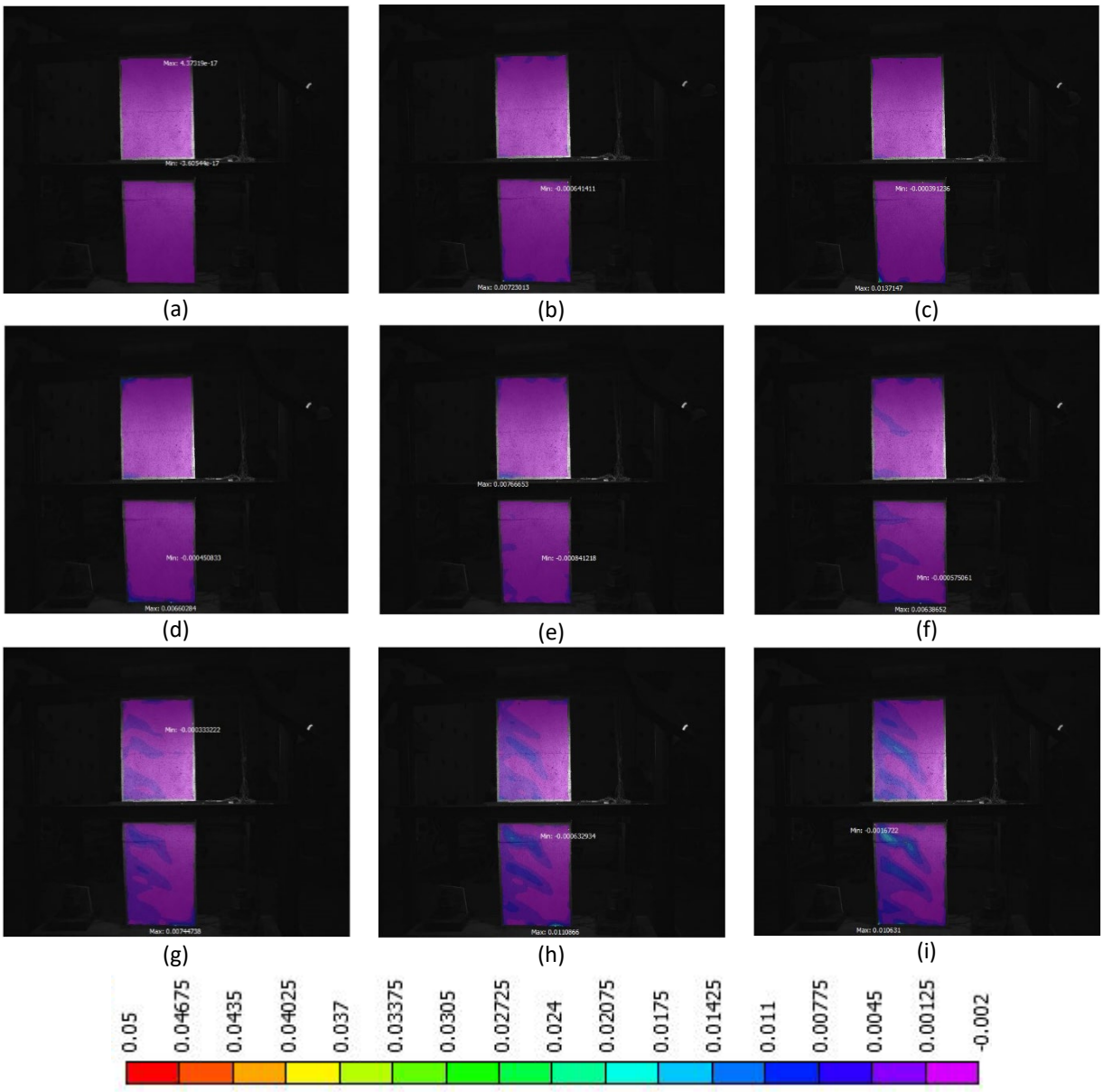

Figure A.62: Damage progression (results from DIC) in control wall specimen (up to drift ratio 1%)

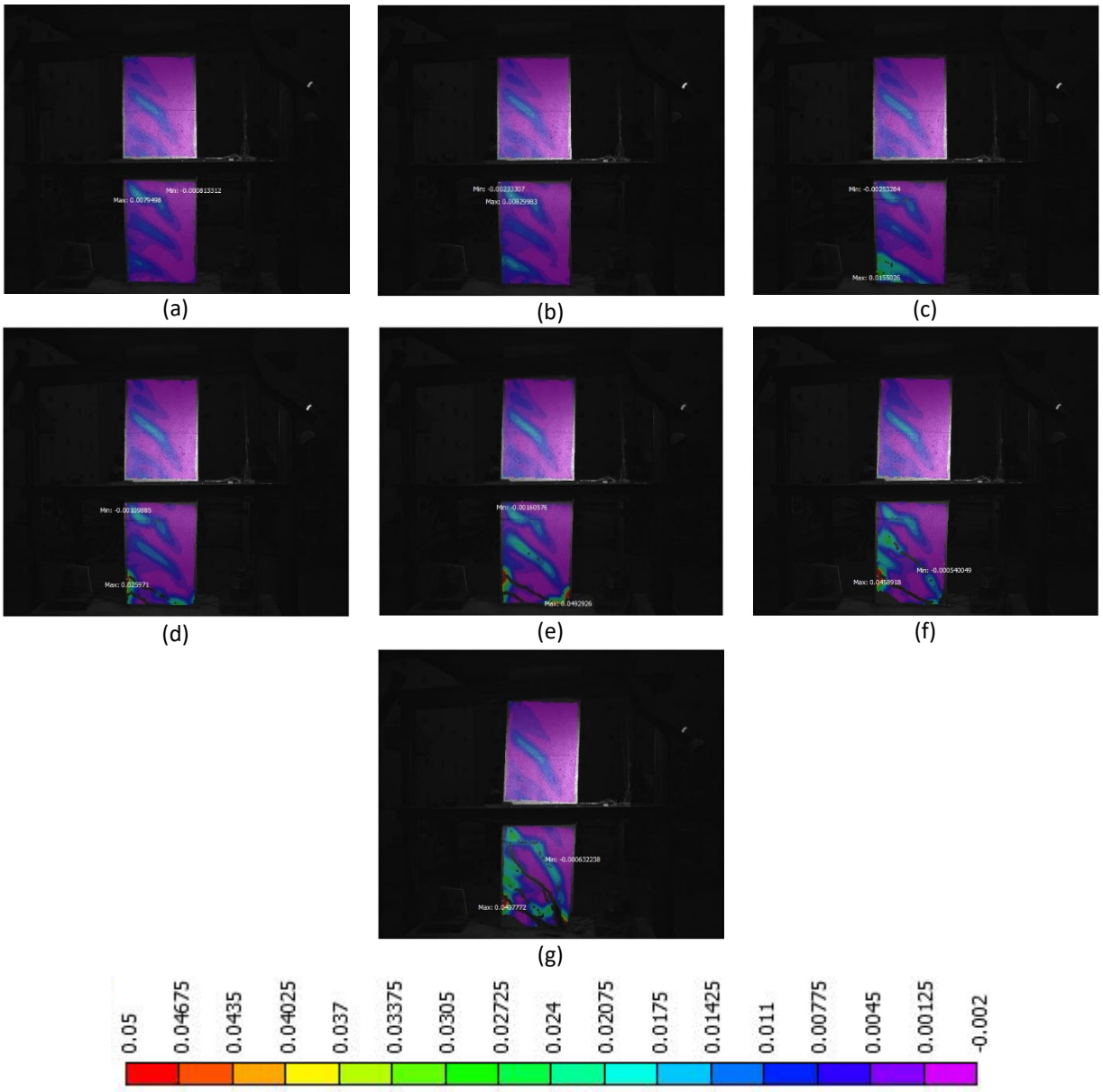

Figure A.63: Damage progression (results from DIC) in control wall specimen (1% drift ratio to failure)